Magnetic Hyperthermia for Spinal Metastases
Using PMMA Loaded with Nanoparticles

Mariem Harabech

Promotoren: prof. dr. ir. L. Dupré, prof. dr. ir. G. Crevecoeur, ereprof. dr. D. Van Roost
Proefschrift ingediend tot het behalen van de graad van
Doctor in de ingenieurswetenschappen: biomedische ingenieurstechnieken

UNIVERSITEIT
GENT

Vakgroep Elektrische Energie, Metalen, Mechanische Constructies en Systemen
Voorzitter: prof. dr. ir. L. Dupré
Faculteit Ingenieurswetenschappen en Architectuur
Academiejaar 2018 - 2019

ISBN 978-94-6355-219-6
NUR 954, 924
Wettelijk depot: D/2019/10.500/27

UNIVERSITEIT
GENT

Ghent University
Faculty of Engineering and Architecture (FEA)
Department of Electrical Energy, Metals,
Mechanical Constructions & Systems
(EEMMeCS)
Electrical Energy Laboratory (EELAB)

Magnetic hyperthermia for spinal metastases using PMMA loaded with nanoparticles

---

Mariem Harabech

Promoters
Prof. dr. ir. Luc Dupre (UGent - EEMMeCS)
Prof. dr. Dirk Van Roost (Ghent University Hospital)
Prof. dr. ir. Guillaume Crevecoeur (UGent - EEMMeCS)

Chairman
Prof. dr. ir. Filip De Turck (UGent - INTEC)

Exam Commission
Prof. dr. ir. Luc Dupre (UGent - EEMMeCS)
Prof. dr. Dirk Van Roost (Ghent University Hospital)
Prof. dr. ir. Guillaume Crevecoeur (UGent - EEMMeCS)
Prof. dr. ir. Wout Joseph (UGent - INTEC)
Prof. dr. ir. Charlotte Debbaut (UGent - ELIS)
Dr. ir. Nele De Geeter (UGent - EEMMeCS)
Prof. dr. ir. Florence Gazeau (UP7 - MSC Lab)
Prof. dr. ir. Gérard Sou (UPMC - L2E)

Acknowledgement

Firstly, I would like to express my sincere gratitude to my supervisors Prof. Luc Dupré and Prof. Guillaume Crevecoeur for the continuous support of my PhD researchs and immense knowledge. Their guidance helped me in all the time of research and the writing of this thesis. I could not have imagined having a better supervison for my PhD study.

Besides my supervisors, I would like to thank Prof. Dirk Van Roost and all my thesis committee for their insightful comments and questions which incented me to widen my research from various perspectives. This PhD work is supported by the UGent Research Fund (BOF project no. 01IO5014).

My sincere thanks goes also to my collegues in EEMMeCS who provided me a nice working atmosphere to enjoy my PhD. Dank u wel voor jullie hulp. Bedankt Marilyn voor onze lunchgesprekken en alles !

I thank my friends and familly. My parents, sisters and cousins for supporting me spiritually during the writing of my thesis. Merci à tous pour votre confiance. A mes soeurs pour votre compréhension. Papa et maman je vous remercie pour votre amour inconditionnel qui me donne la force à chaque épreuve de ma vie.

Last but not the least, I would like to thank my husband for supporting me throughout this PhD and my life in general.

Gent, 2019
Mariem Harabech

Table of Contents

List of Figures

List of Tables

Abbreviations

2D	One-Dimensional
3D	Three-Dimensional
AC	Alternating Current
AMF	Alternating Magnetic Field
BNF	Bionized NanoFerrite
CEM	Cumulative Equivalent Minutes
DC	Direct Current
DNA	DeoxyriboNucleic Acid
FOV	Field Of View
GE	Gradient Echo
HIFU	High-Intensity Focused Ultrasound
HSP	Heat Shock Protein
IgG	Immunoglobulin G
IQR	InterQuartile Range
ILP	Intrinsic Loss Power
LLG	Landau Lifshitz Theory
LRT	Linear Response Theory
MNH	Magnetic Nanoparticle Hyperthermia
MNP	Magnetic Nanoparticle
MRI	Magnetic Resonance Imaging
MRX	MagnetoRelaXometry
mRNA	Messenger RiboNucleic Acid
PEG	PolyEtyleneGlycol
PET	Positron Emission Tomography
PMMA	PolyMethyl MethAcrylate
RF	Radio Frequency
ROI	Region Of Interest
RNA	RiboNucleic Acid
SAR	Specific Absorption Rate
SLP	Specific Loss Power
SNR	Signal-to-Noise Ratio
TER	Thermal Enhancement Ratio
TID	Thermal Isoeffective Dose
UV	UltraViolet

Most used symbols

Scalars, vectors and matrices

a	scalar
a, **A**	vector, matrice
$\underline{A}$	phasor of scalar function
$\underline{\mathbf{A}}$	phasor of vector function

Latin letters

$\mathbf{r}$	spatial coordinate [m]
t	time [s]
T	temperature [°C]
$\mathbf{H}$	magnetic field [A/m]
$\mathbf{E}$	electric field [V/m]
$\mathbf{D}$	electric displacement field [C/m^2]
$\mathbf{B}$	magnetic induction [T]
$\mathbf{M}$	magnetization [A/m]
$\mathbf{J}_f$	free current density [A/m^2]
$\mathbf{I}$	electrical current vector [A]
C	capacitance [F]
L	inductance [H]
d_c	core diameter [m]
d_h	hydrodynamic diameter [m]
f	frequency of excitation [1/s]
H	magnetic field [A/m]
H_0	magnetic field intensity [A/m]
N_t	total number of turs
N_R	number of turn layers in R-direction,
N_l	number of turn layers in z-direction
$\mathbf{n}$	unit vector orthogonal to the surface S
P	power or loss in magnetic nanoparticles [W/m^3]
Q	heat source [W]
U	potential energy [J]
V	electric transmembrane potential [V]
V_M	volume of the nanoparticle [m^3]
V_H	hydrodynamic volume of the nanoparticle [m^3]
Z	impedance [Ω]

Mathematical symbols

$\cdot$	dot product
$\times$	cross product
∇	gradient

Greek letters

α	survival fraction
Δ	penetration depth [m]
γ	gyromagnetic ratio of hydrogen [rad/sT]
δt	time step [s]
δT	temperature increase [°C]
ε	electric permittivity [F/m]
ε_0	electric permittivity of vaccuum [F/m]
μ	magnetic permeability [H/m]
μ_0	magnetic permeability of vacuum [H/m]
μ_r	magnetic relative permeability [H/m]
σ	electric conductivity [S/m]
λ	space constant of the neural membrane [m]
ρ_{MNP}	mass density of MNP [kg/m^3]
ρ_{PMMA}	mass density of MNP [kg/m^3]
Ω	damage index
ω	angular frequency [rad/s]
τ	effective time relaxation [s]
τ_N	Neél relaxation time [s]
τ_B	Brown relaxation time [s]
τ_0	time characteristic of the material [s]
χ	magnetic susceptibility
χ_0	relative susceptibility
$\chi^{'}$	real part of the complex magnetic susceptibility
$\chi^{''}$	imaginary part of the complex magnetic susceptibility
Φ	volume fraction

English summary

Cancer remains one of the world's most overwhelming diseases, with more than 10 million diagnoses every year. Due to the improved diagnostic devices and therapies, mortality has although decreased in the past two years. Traditional curative options for malignant tumors are surgery, chemotherapy, and radiotherapy. Among these cancer treatments, hyperthermia is used as an adjunctive therapy, in conjunction with radio- or chemotherapy to increase their effect or as a seperate therapeutic modality. Hyperthermia consists in heating the tumor tissue which causes cancer cells damage. Cancer cells are susceptible to temperature and can be killed by heat over a period of time. The primary effect starts with the thermal de-activation of the mitochondrial energy conversion within the cell and in a next stage dissociates and degrades the cellular membranes. Secondary, delayed thermal effects appear as pathologic responses to cell and tissue injury.

The principle of administering heat to treat cancer has been around for quite some time. However, the use of external heat sources, to obtain the desired temperature increase in hyperthermia, dates from mid 20th century. A recent and promising application of hyperthermia is based on the principle of exposing magnetic nanoparticles, which are injected in the patient, to an external alternating magnetic field (AMF). The interaction between the magnetic nanoparticles and the AMF results in the local heating of the particles, necessary for the treatment. Magnetic hyperthermia can be used to treat bone metastases where the vertebral body is invaded and weakened by pathological tissue. At the moment, there are methods which allow to either stabilize the spinal column or oncologically treat the metastases within the spinal column. Vertebral body augmentation by the injection of 'cement' by means of polymethylmetacrylate, PMMA, so-called vertebroplasty where PMMA is directly injected using a high pressure device; or kyphoplasty where a cavity is made in the vertebral body with a balloon before filling it with PMMA at relatively low pressure. These methods readily stabilize the spine but do not stop tumor progression. In this dissertation we propose an innovative multidisciplinary treatment modality where PMMA is mixed with magnetic nanoparticles and that is subsequently injected in the tumor cavity where the PMMA+MNP is thermally activated by the AMF. The temperature elevations due to this power source can damage adjacent cancer cells.

The main challenge in bone metastases hyperthermia treatment is associated to

having an appropriate AMF able to sufficiently increase the temperature in the tumor area while minimizing the heating of healthy tissues. Since the magnetic hyperthermia device needs to be placed outside the patient, it is paramount to achieve a certain level of magnetic field at a distance from the AMF generator. The AMF can be generated by a resonant inductor-capacitor circuit. The geometrical properties of the inductor give rise to the characteristic inductance of the inductor and together with the capacitance they determine the resonance frequency at which the AMF varies. The magnetic field strengths were mapped at a certain distance from the coils to the self-inductance values for the various coil topologies. The pancake coil design is selected over the cylindrical, helical and butterfly coil topology as being the most suitable topology for generating a maximal magnetic field strength at a certain distance from the coil. After the performed optimizations we analyzed the effect that the electrically conducting human body has on the attenuation of the magnetic field inside the human body and to what eddy current losses this leads. Results furthermore show that the magnetic field at the position of the spinal cord is hardly affected by the shielding effect of the human tissue. We concluded that having normal magnetic fields incident to the human body is preferred compared to tangential magnetic fields as this leads to lower eddy current losses.

The AMF can interact with materials resulting in heating power and a second challenge in this dissertation was to inspect the heating power depending on the material characteristics. As a matter of fact, the type and properties of the particles, such as its size, its magnetic and non-magnetic properties, affect the heating power. The mechanisms related to the heat generation are described based on the energies and losses of each type of material. Heating efficiency produced by the particles exposed to AMF is expressed using the specific loss power (SLP). SLP is traditionally measured using the calorimetric method where the change in heating power is related to the measured temperature increase. This method however contains uncertainties since it is difficult to achieve adiabatic conditions that are required for having accurate measurement.

Non-magnetic conducting materials subject to alternating magnetic fields generate heat due to eddy current losses. These losses are estimated for different conducting materials such as carbon and titanium. We experimentally evaluate the heating efficacy of particles experimentally using the calorimetric method. We furthermore check whether the prerequisite of maintaining mechanical stability of the PMMA-particles material, as well as its MRI compatibility, since these can be infringed by having too high concentrations of particles. We observed experimentally, in accordance to the theory of eddy current loss, that the temperature increase with samples consisting of a mixture of PMMA with non-magnetic particles remains limited and not sufficient for bone metastases hyperthermia treatment. Moreover, the performed analyses of the effect of these particles on the quality of magnetic resonance images shows that the non-magnetic particles' concentration needs to be low to have limited artifacts.

In magnetic materials, the specific loss mechanisms are related to hysteresis loss,

eddy current loss, and Néel and Brownian relaxation loss mechanisms in magnetic nanoparticles. We omit the particles to realize heating by Brownian motion since they are fixed in a PMMA matrix. State of the art considers the linear response theory for estimating the power loss of magnetic nanoparticles and we propose a correction of the linear response theory with respect to the size of the magnetic nanoparticles by considering their lognormal distribution. We conclude that using magnetorelaxometry measurement data it is possible to recover this characteristic length of time and include this together with the correction factor to predict the specific loss power due to Néel and Brownian relaxation. Specific loss power measurements were performed using the calorimetric method. We demonstrated that temperature increase can be achieved with PMMA+MNP and compared this when having ferrofluids. Since PMMA+MNP only has Néel relaxation the specific loss power was relatively lower but nevertheless we could achieve even with relatively low concentration of MNP a temperature increase of at least 6 °C that is needed for hyperthermia treatment. We also investigated the effect of MNP on the quality of magnetic resonance images. Both the concentration and type of MNP affect the MRI compatibility of PMMA mixed with MNP. Single core clustered powder resulted, for similar concentrations, in higher artifacts compared to multicore MNP. We showed that having multicore powder having an iron oxide concentration of 0.07 wt% in the PMMA+MNP, resulted in artifacts that are less than 2 mm and that gave rise to a temperature increase of 7°C which is sufficient for hyperthermia treatment of bone metastases. This resulted in a proper protocol for the material preparation PMMA+MNP of magnetic hyperthermia.

Based on the heating power that PMMA+MNP can generate when interacting with a given AMF, we follow a model based approach where the heat transfer within the vertebra is assessed. Based on Pennes' bioheat equation we calculate temperature distributions in space and time within biological tissues. A simplified geometrical model of the vertebra is used to perform extensive thermal analyses on the effect of the heating power of particles in PMMA and biological tissue properties on the temperature. We also appraise whether and when we satisfy the prerequisite of not thermally stimulating the spine and to not reach too high levels of temperatures in healthy tissues. Damage models are included to provide a means to measure the extent of inflicting damage to biological tissues. We assess the effect of the damage models and evaluate the possibility of performing hyperthermia for treating spinal metastases. Results of a computational study of temperature distributions and the tumor tissue damage release profiles due to an applied alternative magnetic fields through a PMMA-MNP implant for bone metastases therapy reveal that it is possible to define a switching On/Off strategy in order to increase the temperature in tumor region up to the required level of 43-45°C. We also observed the effect of the tumor volume on the required power. Results show that depending on the dimensions and the position of the tumor relative to the spinal cord, the applied power should be limited in order to avoid the damage in the spinal cord.

Finally, we integrate all above aspects to experimentally realize and validate *ex-vivo* the heating of PMMA+MNP in beef vertebra that is subject to AMF originating from an inductor-capacitor ciruit located at a certain distance from the vertebra. We demonstrate heating in an *ex-vivo* experiment for an inductor-capacitor circuit located at a certain distance from magnetic particles in a PMMA matrix. A coil was designed so to enable future animal and clinical tests; that satisfy technological constraints, i.e. the minimally allowed capacitance of the capacitors in the resonant inductor-capacitor circuit of the AMF generator; and that generates maximum alternating magnetic fields at a distance of 10 cm above the inductor. We demonstrate the feasibility of having hyperthermia on the basis of PMMA-MNP samples containing 22 wt.% iron oxide nanoparticles. The *ex-vivo* experiments show that the PMMA-MNP sample, which is in clinical application in the vicinity of the metastatic bone tumors, heats up to 7 °C with a negligible temperature increase in the spinal cord. We moreover experimentally verified the temperate rise in the PMMA-MNP sample and in the spine when applying On-Off switched AMF, mimicking a clinical procedure that enables the control of temperature elevations in healthy tissue as well as in the spine. The temperature rise in the spine was limited to 2 °C whereas in the PMMA-MNP a temperature rise was in the range of 6-8 °C.

Nederlandse samenvatting –Summary in Dutch–

Kanker is nog steeds een van 's werelds meest overweldigende ziekten, met elk jaar meer dan 10 miljoen diagnoses. Verbeterde therapieën en apparaten die meer accuraat diagnoses kunnen stellen hebben ervoor gezorgd dat de mortaliteit in de afgelopen twee jaar weliswaar is afgenomen. Traditionele opties om kwaadaardige tumoren tegen te gaan zijn chirurgie, chemotherapie en radiotherapie. Onder deze kankerbehandelingen wordt hyperthermie gebruikt als een aanvullende therapie, in combinatie met radio- of chemotherapie om hun effect te vergroten of als een afzonderlijke therapeutische modaliteit. Hyperthermie is een therapie die bestaat uit het opwarmen van het tumorweefsel dat op die manier kankercellen beschadigt. Kankercellen zijn immers gevoelig voor temperatuur waarbij zij worden gedood door warmte via verschillende processen. Het primaire effect begint met de thermische de-activering van de mitochondriale energieconversie in de cel en in een volgende fase dissocieert en degradeert de celmembranen. Secundaire, vertraagde thermische effecten verschijnen als pathologische reacties op cel- en weefselbeschadiging.

Het gebruik van warmte om kanker te behandelen bestaat al geruime tijd. Het gebruik van externe warmtebronnen om de gewenste temperatuurstijging bij hyperthermie te bereiken, dateert van het midden van de 20e eeuw. Een recente en veelbelovende toepassing van hyperthermie is gebaseerd op magnetische nanodeeltjes, die in de patiënt worden geïnjecteerd, en die onderhevig zijn aan een extern wisselend magnetisch veld. De interactie tussen de magnetische nanodeeltjes en het extern magnetisch veld resulteert in de lokale opwarming van de deeltjes, noodzakelijk voor de behandeling. Magnetische hyperthermie kan worden gebruikt voor de behandeling van botmetastasen. Deze botmetastasen kunnen actief zijn in de wervels van de ruggengraat en deze structureel verzwakken. Het stabiliseren van de wervelkolom is klinisch mogelijk via volgende methoden. Vertebroplasty is het injecteren van ``cement´´door middel van polymethylmetacrylaat, PMMA, met behulp van een hogedrukapparaat; of kyphoplastie waarbij een holte wordt gemaakt in het wervellichaam met een ballon voordat deze wordt gevuld met PMMA bij relatief lage druk. Deze methoden stabiliseren de wervelkolom gemakkelijk, maar stoppen de tumorprogressie echter niet. In dit proefschrift stellen we een innovatieve multidisciplinaire behandelingsmethode voor waarbij PMMA gemengd wordt met magnetische nanodeeltjes en die vervolgens wordt geïnjecteerd in de

tumorholte waarbij het PMMA samen met magnetische nanodeeltjes thermisch wordt geactiveerd door een extern magnetisch veld. De temperatuurverhogingen als gevolg van deze stroombron kunnen aangrenzende kankercellen beschadigen.

De belangrijkste uitdaging bij hyperthermiebehandeling van botmetastasen is het bekomen van een geschikt extern magnetisch veld dat in staat is om de temperatuur in het tumorgebied voldoende te verhogen terwijl het gezonde weefsels minimaal wordt opgewarmd. Aangezien het magnetisch veld extern aan de patiënt moet worden geëxciteerd, is het van het grootste belang om een bepaald niveau van magnetisch veld op afstand van de magnetische veld generator te bereiken. Het extern magnetisch veld kan worden gegenereerd door een resonante inductor-condensatorschakeling. De geometrische eigenschappen van de inductor resulteren in een karakteristieke inductantie van de inductor en bepalen samen met de capaciteit de resonantiefrequentie waarmee het magnetische veld varieert. De magnetische veldsterkten werden op een bepaalde afstand van de spoelen in kaart gebracht alsook de zelfinductiewaarden voor de verschillende spoeltopologieën. Het zogenaamde pannenkoekspoelontwerp, een ontwerp waarbij de windingen van de spoelen in een vlak liggen, wordt gekozen als meest geschikte topologie boven de cilindrische, spiraalvormige en vlinderspiraal-topologie. Deze topologie geeft een maximale magnetische veldsterkte op een bepaalde afstand van de spoel. Na de uitgevoerde optimalisaties hebben we het effect geanalyseerd dat het elektrisch geleidende menselijke lichaam heeft op de verzwakking van het magnetische veld in het menselijk lichaam en de daaraan gekoppelde wervelstroomverliezen. Resultaten geven aan dat het magnetische veld ter hoogte van het ruggenmerg nauwelijks wordt beïnvloed door het afschermende effect van het menselijke weefsel. We concludeerden dat het hebben van magnetische velden met een normale component ten opzichte van het menselijk lichaam de voorkeur geniet boven magnetische velden met een tangentiële component. Dit omdat magnetische velden die een normale component hebben tot lagere wervelstroomverliezen leiden.

Een tweede uitdaging was om het opwarmingsvermogen van nanodeeltjes, die interageren met het extern magnetisch veld, in te schatten. Het opwarmingsvermogen is afhankelijk van de materiaaleigenschappen van de nanodeeltjes, zoals het type van deeltjes, hun grootte, en hun magnetische en niet-magnetische eigenschappen. De mechanismen die aanleiding geven tot warmteontwikkeling worden beschreven op basis van de energieën en verliezen van elk type materiaal. De opwarmingsefficiëntie geproduceerd door de deeltjes blootgesteld aan het extern magnetisch veld wordt uitgedrukt als het specifieke verliesvermogen. Het specifiek verliesvermogen wordt traditioneel opgemeten met behulp van de calorimetrische methode waarbij de verandering in verwarmingsvermogen gerelateerd is aan de gemeten temperatuurstijging. Deze methode bevat echter onzekerheden omdat het moeilijk is om adiabatische condities te bereiken die vereist zijn voor een nauwkeurige meting.

Niet-magnetische materialen onderhevig aan wisselende magnetische velden ge-

nereren warmte als gevolg van wervelstroomverliezen. Verliezen van verschillende geleidende materialen zoals koolstof en titanium zijn geschat. Verder evalueren we experimenteel de warmte-efficiëntie van deze deeltjes met behulp van de calorimetrische methode. We controleren bovendien of de vereiste van het handhaven van de mechanische stabiliteit van de deeltjes samengevoegd met PMMA is gegarandeerd, alsmede de MRI-compatibiliteit ervan. Deze vereisten kunnen immers geschonden worden indien te hoge concentraties van deeltjes worden gebruikt. Experimentele analyses toonden aan dat de temperatuurstijging met monsters bestaande uit een mengsel van PMMA met niet-magnetische deeltjes beperkt blijft en niet voldoende is voor hyperthermiebehandelingen van botmetastasen, wat in overeenstemming is met de theorie van wervelstroomverlies. Bovendien dient de concentratie van niet-magnetische deeltjes relatief laag blijven om artefacten in magnetische resonantiebeeldvorming te beperken.

De specifieke verliesmechanismen in magnetische materialen zijn gerelateerd aan hysteresisverlies, wervelstroomverlies en Néel en Browniaanse relaxatieverliesmechanismen. Aangezien de deeltjes vastzitten in een PMMA-matrix, kan er geen opwarming via Browniaanse beweging gerealiseerd worden. De huidige literatuur beschouwt de lineaire-responstheorie als een schatting voor het vermogensverlies van magnetische nanodeeltjes. We stellen een correctie voor van de lineaire-responstheorie die corrigeert voor de grootte van de magnetische nanodeeltjes die een lognormale verdeling volgt. We stellen dat experimentele magnetorelaxometrie metingen gebruikt moeten worden om de karakteristieke tijdsduur te extraheren en dit samen met de correctiefactor te gebruiken om het specifieke verliesvermogen als gevolg van Néel en Browniaanse relaxatieverliesmechanismen te voorspellen. Specifieke verliesvermogensmetingen werden uitgevoerd met behulp van de calorimetrische methode. De temperatuurstijgingen van een mengsel van PMMA met magnetische nanodeeltjes werd vergeleken met ferrofluids. Het mengsel PMMA met magnetische nanodeeltjes heeft enkel Néel-relaxatieverliesmechanismen waardoor het specifieke verliesvermogen relatief lager ligt dan bij ferrofluids, maar toch konden we zelfs met een relatief lage MNP-concentratie een temperatuurstijging van ten minste 6°C bereiken die nodig is voor behandeling met hyperthermie. We onderzochten ook het effect van de magnetische nanodeeltjes op de kwaliteit van magnetische resonantiebeelden. Zowel de concentratie als het type magnetische nanodeeltjes beïnvloeden de MRI-compatibiliteit van PMMA gemengd met magnetische nanodeeltjes. Nanodeeltjes met een enkelvoudige magnetische kern in poedervorm resulteerde, voor vergelijkbare concentraties, in hogere artefacten in vergelijking met magnetische nanodeeltjes die een meervoudige magnetische kern hebben. We toonden aan dat deze laatste met een ijzeroxide-concentratie van 0.07 gew.% in het mengsel PMMA met magnetische nanodeeltjes resulteerde in artefacten die minder dan 2 mm waren. Dit mengsel gaf bovendien een temperatuurtoename van 7°C die voldoende is voor hyperthermiebehandeling van botmetastasen. Dit resulteerde in een adequaat protocol voor de materiaalbereiding van het mengsel PMMA met magnetische nanodeeltjes voor magnetische hyperthermie.

Op basis van het bestudeerde opwarmingsvermogen dat het mengsel PMMA met magnetische nanodeeltjes kan genereren bij interactie met een extern magnetisch veld, volgen we een modelgebaseerde benadering waarbij de warmteoverdracht binnen de wervel wordt nagegaan. We berekenen de temperatuursverdelingen in een wervel gebaseerd op de zogenaamde warmtevergelijking in biologisch weefsel van Pennes. Een vereenvoudigd geometrisch model van de wervel wordt gebruikt om de temperatuur te analyseren als gevolg van het verliesvermogen van het mengsel PMMA met magnetische nanodeeltjes in de wervel alsook het effect van de biologische weefseleigenschappen op de temperatuursdistributie is geanalyseerd. We beoordelen ook of en wanneer we voldoen aan de voorwaarde om de wervelkolom niet thermisch te stimuleren en dat niet te hoge temperaturen worden bereikt in het gezonde weefsel. In de analyses wordt gebruik gemaakt van schademodellen om de mate van het toebrengen van schade aan biologische weefsels door warmte te meten. We beoordelen het effect van de schademodellen en evalueren via numerieke berekeningen de vooropgestelde magnetische hyperthermie voor de behandeling van spinale metastasen. Resultaten van dit computationeel onderzoek onthullen dat het mogelijk is om een aan / uit-strategie te definiëren van het extern magnetisch veld om de temperatuur in het tumorgebied tot het vereiste niveau van 43-45 °C te laten toenemen. We hebben ook het effect van het tumorvolume op het vereiste vermogen waargenomen. Het vermogen, die afhankelijk is van de afmetingen en de positie van de tumor ten opzichte van het ruggenmerg, dient beperkt te zijn om schade via thermische stimulatie van de ruggenmerg te voorkomen.

Ten slotte integreren we alle bovengenoemde aspecten om experimenteel de opwarming van een mengsel van PMMA met magnetische nanodeeltjes te realiseren en voeren een ex-vivo validatie uit van de vooropgestelde modaliteit van PMMA met magnetische nanodeeltjes in een rundswervel waarbij het extern magnetisch veld afkomstig is van een op een bepaalde afstand van de wervel gelegen inductor-condensator circuit. Een spoel is ontworpen om toekomstige (pre-) klinische testen mogelijk te maken waarbij deze een maximaal extern magnetisch veld genereert op een aftand van 10 cm boven de inductor. We demonstreren de haalbaarheid van magnetische hyperthermie op basis van monsters met een mengsel PMMA met magnetische nanodeeltjes die 22 gew.% ijzeroxidenanodeeltjes bevatten. De ex-vivo experimenten tonen aan dat het PMMA met magnetische nanodeeltjes monster tot 7 °C opwarmt met een verwaarloosbare temperatuurstijging in het ruggenmerg. De aan / uit-strategie van het extern magnetische veld werd hier gevolgd waarbij een klinische procedure werd nagebootst die de regeling van temperatuurverhogingen in gezond weefsel beperkt houdt en opwarming van metastasen in de wervelkolom mogelijk maakt. De temperatuurstijging in de ruggenmerg was beperkt tot 2 °C, terwijl in de nabijheid van het mengsel PMMA met magnetische nanodeeltjes in het bereik van 6-8 °C was.

1 General introduction

'Nothing in life is to be feared, it is only to be understood. Now is the time to understand more, so that we may fear less'

Marie Curie

1.1 Introduction

This general introduction chapter 1 introduces the magnetic hyperthermia treatment for spinal metastases. Hyperthermia is a modality that inflicts heat to biological tissues and that needs to be tailored for enabling the treatment of spinal metastases. Since spinal metastases weaken the spinal cord, polymethylmetacrylate (PMMA) is used to stabilize the spinal cord. This dissertation explores the use of magnetic nanoparticles loaded in PMMA enabling magnetic hyperthermia of metastastatic bone tumors in the spinal cord. This interdiscplinary approach is extensively studied in this dissertation to come to an engineered treatment modality for neurosurgery. In Section 1.1 the biological aspects of cancer are shortly introduced together with possible treatment modalities of cancer. Section 1.2 presents the current hyperthermia techniques in oncology. Specifically the magnetic hyperthermia treatment modality is introduced in Section 1.3 for the treatment of spinal metastases. In Section 1.4 the challenges associated to engineering a spinal metastases hyperthermia treatment modality are presented.

1.2 Biological fundamentals of cancer

1.2.1 Cell cycle

Cell is the smallest functional unit within a living organism which can function independently. Similar cells from the same origin are grouped together and combined with their intercellular materials to form organs. Most tissues of the body grow by increasing their cell number, but this growth is highly regulated to maintain a balance between different tissues. An exception to this is the genetic material of cell, the deoxyribonucleic acid or DNA. The DNA is duplicated during the cell-division cycle, also known as DNA replication, leading to two daugther cells with the same genetic component as the parent cell [11]. Cell division consists of two stages: mitosis (M) and interphase. The cell division cycle is sketched in Fig.1.1. Mitosis is the process of nuclear division and includes prophase, metaphase, anaphase and telophase. Interphase is the interlude between two M phases and comprises G_1, S and G_2 phases, see Fig.1.1. Replication of DNA occurs in a specific part of the interphase called S phase. S phase is preceded by a gap called G_1 during which the cell is preparing for DNA synthesis and is followed by a gap called G_2 where the cell prepares for mitosis. G_1, S, G_2 and M phases are the traditional subdivisions of the standard cell cycle. Cells in G_1 can, before commitment to DNA replication, enter a resting state called G_0. Cells in G_0 account for the major part of the non-proliferating cells in the human body. The transition from one cell cycle phase to another is regulated by different cellular proteins [12].

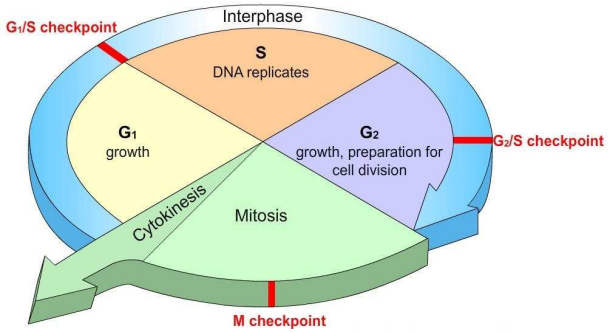

Figure 1.1: Cell division cycle: Interphase comprises the G_1, S and G_2 phases. DNA is synthesized in S. During G_2 the cell is prepared for the mitotic (M) phase, when the genetic material is duplicated and the cell divides. Nondividing cells exit the normal cycle, entering the quiescent G_0 state [http://ricochetscience.com/].

The cell cycle ends by the cell death. A cell is considered dead when it has lost the integrity of its plasma (cell membrane holding the integrity of the cell material) or its body has been engulfed by an adjacent cell [13]. Cell death comes in

two distinct types: apoptosis and necrosis. Apoptosis is a normal physiological process eliminating DNA-damaged or unwanted cell. It is a genetically directed process of cell self-destruction while necrosis is a premature death of cells caused by external factors such as infection, toxins, or trauma. These two processes occur concurrently to the cell division cycle. This guarantees the renewal of healthy tissue. However, imbalance in the above processes can ensue leading to new tissue growing. When a mass of new tissue grows independently of its surrounding structures and has no physiological function it is commonly called tumor. A tumor can be benign or malignant. The benign tumor cannot spread and mostly do not return afer being removed. Malignant tumors are cancerous tumors characterized by a fast growth of abnormal cells, as illustrated in Fig.1.2. The fast growth of cancer cells is due to cell cycle deregulation. It develops through mutations in the genes controlling the cell proliferation. Each cancer type is associated to a certain mutational signature [14]. For instance, the gene for the signaling protein RAS, are among those most commonly mutated in cancer cells. RAS proteins control cellular signaling pathways responsible for growth, migration, adhesion, cytoskeletal integrity, survival and differentiation. In cancer cells, RAS proteins become super-active and produce cells that are too strongly stimulated by growth receptors. Other cancer-related mutations inactivate the genes that suppress cell proliferation or those that signal the need for apoptosis. These genes, known as tumor suppressor genes, normally brake cell proliferation [15].

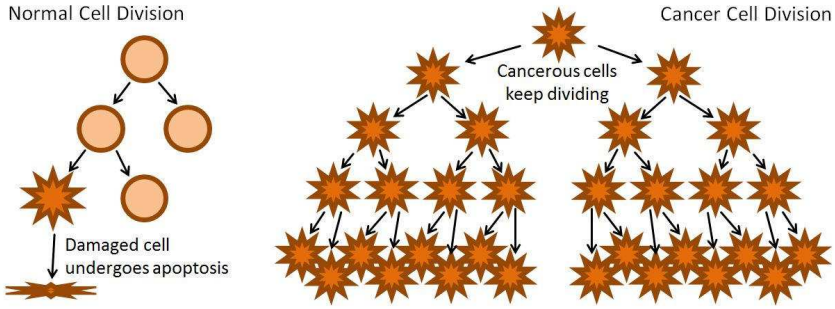

Figure 1.2: Normal cells division in comparison with cancer cells [SNS Web-November 2, 2016].

1.2.2 Types of cancer

There are more than 100 types of cancer based on their location in the body or the type of cell that formed them [16]. Primary cancer concerns the uncontrolled growth in a particular organ. The cancer cells have the same origin as the organ cells wherein they grow. In metastases, cancer cells spread to other parts

of the body through the blood or lymphatic systems. Thus, metastases have not the same type of cells in the site where they are located [17]. Carcinoma is the most common type of cancer. They are formed by epithelial cells, which are the cells that cover the inside and outside surfaces of the body [18]. Many types of carcinoma occur among older adults in prostate, breast, lung, liver and colon. Carcinoma are responsible for more than 80% of deaths associated to cancer. Sarcoma start in connective tissues, which are the supporting tissues of the body formed of mesenchymal cells. They mainly develop in the bone, cartilage and soft tissues including muscle, fat, blood and lymph vessels, and fibrous tissue e.g. tendons and ligaments tissues. Cancers that begin in the blood-forming tissue of the bone marrow are called leukemias. The bone marrow overproduce white cells which cause the dysfunction of blood cells. These cancers are the most common type in children [19]. Lymphomas and myeloma are cancers of the lymphatic system. Lymphoma is cancer that begins in lymphocytes (T cells or B cells). The abnormal lymphocytes start to collect in the lymph nodes or other places such as the bone marrow or spleen. They can then grow into tumors. Multiple myeloma is a cancer that begins in plasma cells, another type of immune cell [20]. Melanoma is cancer that begins in cells that become melanocytes, which are specialized cells that make melanin (the pigment that gives skin its color). Most melanomas form on the skin, but they can also form in other pigmented tissues, such as the eye [21].

1.2.3 Treatments of cancer

The objective of cancer thearapy is to provoke the death of cancer cells. Therefore, the conventional anti-cancer treatments aim to induce apoptosis where cells effectively get ordered to destroy themselves via proteins called caspases [22] [23]. Depending on the type and stage of cancer, specific treatments are recommended. Surgery, chemotherapy and radiotherapy are the most clinically available cancer treatments [24]. Moreover, recent applications based on the increase of temperature are heavily investigated to treat various types of cancer. The most common treatment modalities of cancer are surgery, radiation and chemotherapy. These techniques are common in clinical oncology and have undergone different phases of preclinical research before first-in-man studies and ultimately as common treatment modality. Preclinical research may vary from assessing the efficacy of surgery techniques on *in-vivo* small animals to drug development in chemotherapy. A fourth treatment modality is hyperthermia and which is central in this dissertation. Opposed to the previously mentioned cancer treatment modalities, hyperthermia is still much in the phase of preclinical research.

1.2.3.1 Surgery

Surgery has been the first curative option for cancer patients. It consists in removing all malignant cells located in the tumor area. The surgeon might take out all or part of the organ affected by the cancer such as for prostate cancer where the prostate gland might be removed. Unfortunately, only a small proportion of patients who have cancer can benefit from surgical therapy because of unfavorable tumor location or high operative risk [25]. Advancements in a series of minimally invasive tumor ablation techniques have amongst others been developed in this context [26]. These techniques aim at achieving necrosis of cancer cells by inflicting relatively high temperatures (order of 50-80°C) to the cancer cells. These temperature ranges are much higher than the temperatures considered in hyperthermia (Section 1.2.3.4).

1.2.3.2 Radiation therapy

Radiation therapy uses waves of radiation to treat cancers and tumors. It works by stopping or slowing the growth of cancer cells. The main objective of this theapy is to provoke DNA damage of cancer cells [27]. This way the cell-division cycle (i.e. the S phase in Fig.1.1) is altered. The treatment uses high doses of radiation to kill cancer cells. The form of radiation used in cancer therapy is a high-energy type known as ionizing radiation. Most side effects of radiation therapy are due to the uncontrolled deposition of ionizing radiation in the treated region leading to affecting healthy tissue near the tumor [28].

1.2.3.3 Chemotherapy

As radiation therapy, chemotherapy aims at killing or slowing the spread of cancer cells. Chemotherapy drugs can be administered as a pill or directly injected into a vein through a needle. Most chemotherapeutic agents interfere with replication, either by damaging DNA or by acting as nucleoside analogues which often cause S-phase arrest or prevent mitosis by stabilizing microtubules cells. By combining different chemotherapy drugs, it becomes possible to damage cancer cells at various stages in the process of cell division [29]. Chemotherapy has beneficial effects to fight cancer that has spread because drugs travel to nearly all parts of the body. For instance, leukemia are mainly treated with chemotherapy [30]. Nonetheless, tumor cells are generally located in poorly vascularized areas where it is difficult to have the adequate concentration of chemotherapy drugs. Consequently, high drugs doses are used to have an efficient treatment which damage not only cancer cells but also the healthy cells. This can cause side effects for the patient such as fatigue, hair loss and nausea [31].

1.2.3.4 Hyperthermia

Unlike the previous treatment modalities, hyperthermia is much less frequently used for treating cancer. Only recently, hyperthermia has gained increased interest, initiating a vast amount of preclinical research activities. In this subsection, we introduce hyperthermia as treatment modality and how it can be combined with other treatment modalities. In the subsequent section 1.3, we will detail hyperthermia and the different existing hyperthermia techniques. Hyperthermia is used to raise the body or local tissue temperature to the range of 41-47°C. When using higher temperatures eg. above 50°C, we talk about thermal ablation. It refers also to the destruction of tissue by extreme hypothermia or cryoablation using temperatures between -10°C and -75°C. The heating of the tissue induces a sequence of biological processes leading to degradation of tumor cells. Previous research demonstrated that malignant and normal cells have different response to heat [32]. The microenvironment of cells in solid tumors is particularly sensitive to heat. The tumor environment is characterized as having a low pH, low oxygen tension and lack of nutrients [33]. The combination of those parameters tends to make tumor cells extremely responsive to elevated temperatures. Hyperthermia is most commonly used in combination with other treatment modalities such as radiotherapy and/or chemotherapy to make the tumor cells more sensitive to radiation doses or drugs administered to the patient [34]. It has been shown that the increase of body temperature enhances the effect of radiation therapy [35]. In fact, cancer cells under acidic and low oxygen conditions resist radiation therapy while there are effectively sensitized by heat [36]. Hyperthermia is particularly advantageous when used in conjunction with highly effective radiotherapy modalities such as proton therapy and brachytherapy [37] [38]. On the other hand, the use of hyperthermia increases the uptake of specific group of chemotherapeutic drugs since it increases the blood flow. This group includes doxorubicin, cyclophosphamide and ifosphamide [39]. The last type shows a distinct sensitization at temperature ranges of 41 to 43 °C. These are drugs such as cisplatin, carboplatin and bleomycin [40].However, there are drugs where hyperthermia does not have an action, these include drugs like 5-fluorouracil, methotrexate and taxane [41]. In this case, chemotherapy is combined to other anti-cancer techniques such as immunotherapy or radiation therapy [42]. Fig.1.3 shows the response percentage of randomized clinical trials (RCT) with a significant enhancement in clinical outcome when hyperthermia was added to radiotherapy and/or chemotherapy. The highest improvement is observed in the case of bladder cancer where the response rate increases from 15% to 53%. For breast, head, neck and thyroid cancers, the combined treatment double the response percentage. Positive effect of hyperthermia on response rate is also noticed in cervical, esophageal, rectal, sarcoma and pediatric cancers. A summation of the data from these studies (total 713 lesions) shows an increase in complete response rate from 31% to 67%.

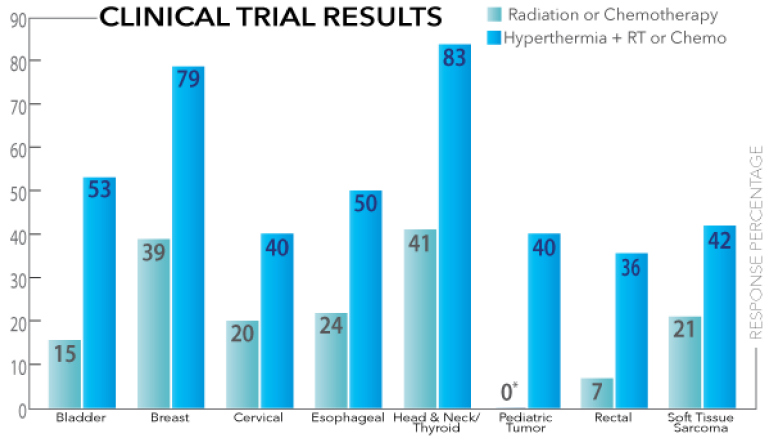

Figure 1.3: The advantage on response rates of using chemotherapy and/or radiotherapy with hyperthermia against the use of either chemotherapy or radiotherapy alone in various cancers [1].

1.3 Hyperthermia in oncology

As highlighted in previous section, hyperthermia is a cancer therapy that can induce cell damage and that can be used in conjunction with other cancer therapies. In subsection 1.3.1 we elaborate on the effects of heat on cells and what the cellular mechanisms are of hyperthermia. In the subsequent subsections we detailed the different types of hyperthermia and the ways how heat can be induced in cells.

1.3.1 Effects of heat on cells

Protein damage, heat shock response and immune response are the most common effects of heat on cells [43]. When subjected to high temperature, the hydrophobic portions of the protein shield itself from the hydrophilic environment of the cell by burying into the interior of the protein. This folding process induce the aggregation of proteins and it is reversible in the presence of specific molecules such as heat shock proteins (HSP). HSP are activated through an upregulated process by which a cell increases the quantity of a cellular component. They prevent protein aggregation by allowing cell thermotolerance, i.e. cells become insensitive to the effect of temperature. [39]. However, higher temperatures cause not only aggregation of proteins but also denaturation. Denaturation induces the arrest of cell cycle and the inactivation of protein synthesis which normally balances the degradation of proteins or their export to other destinations within the cell. Since the balance becomes disrupted, protein damage occurs and this at different cell levels. In fact, elevated temperatures cause the lowering of viscosity and permeability and ulti-

mately damage of the cell membrane. As a result, the intracellular concentration of Na^+, H^+ and Ca^{2+} increases, leading to toxic cell environment. Besides the cell membrane, high temperatures cause also damage to the DNA. In fact, it provokes the inhibition of DNA synthesis (i.e. G1 phase in Fig.1.1), transcription and blocks its reparation. Applying high temperatures to cells also cause other cellular effects such as immune response [44]. There are several different mechanisms that activate both the adaptive and innate immune system. The initial innate immune response uses germline genes to recognise foreign substances or damaged tissue. The adaptive one utilises somatically rearranged genes to generate multiple structural specificities that allow the induction of responses specific to individual invading organisms and damaged cells. As always, these mechanisms depend on the elevation of the applied temperature, and the amount of time to which the cells are subjected to the temperatures, also called exposure time [43].

1.3.2 Modalities of hyperthermia

Hyperthermia can be classified into the extent of the treated region to which elevated temperatures are applied. Three types of hyperthermia are commonly considered: whole body hyperthermia, partial or regional hyperthermia and local hyperthermia.

1.3.2.1 Whole body hyperthermia

Whole body hyperthermia (WBH) is used to treat metastatic cancer that has spread throughout the body. All tissues are heated up to 42°C using the following possible approaches [45]:

- Thermal conduction (surface heating): Patients wear heated circulating water suits that aim at fully heating the body. Sometimes heating blankets and hot wax baths are used as well.
- Extra-corporeal induction: Blood is heated by extracorporeal circulation, also referred to as venous perfusion WBH.
- Radiant heat or microwave radiation: By microwave radiation, a certain dose of heat is deposited to the body. The initial power absorption is non-uniform but the circulatory system leads to a redistribution of the thermal energy in the whole body.

1.3.2.2 Regional hyperthermia

In regional hyperthermia a part of the body, such as an organ, limb, or body cavity is heated. It is usually combined with chemotherapy or radiation therapy, cfr. the

mechanisms mentioned in 1.3.1. In one approach, called regional perfusion or isolation perfusion, the blood supply to a part of the body is isolated from the rest of the circulation. The blood in that part of the body is pumped into a heating device and then pumped back into the area. Chemotherapy can be injected at the same time. This technique is currently being studied as treatment for certain cancers in the arms or legs, such as sarcomas and melanomas. Another approach to regional hyperthermia is deep tissue hyperthermia. This treatment uses devices that are placed on the surface of the organ or body cavity and produce high energy waves directed at a certain area. These devices give off radiofrequency or microwave energy to heat the area that requires treatment [46].

1.3.2.3 Local hyperthermia

Contrary to a whole-body and regional approaches, local hyperthermia is used to heat small scale tumors or small regions of tumors. The higher the temperature and duration of exposure, the greater is the damage to the cancer tissues. Diverse forms of energy can be used to heat the tumor area. Superficial tumors can be heated by means of antennas or applicators emitting mostly microwaves or radiowaves placed on their surfaces with a contacting medium. Several types of applicators have been used, such as waveguide applicators, spiral and sheets with high frequency electrical currents flowing in it [34]. The resulting heat distributions result in therapeutic depths of only a few centimeters and is even further limited in regions with an irregular surface, such as the head and neck area. For other techniques, we refer to the next subsection.

1.3.3 Thermotherapy techniques

There are four hyperthermia techniques that are mainly used to produce heat either regionally or locally: ultrasound, radiofrequency, microwave and magnetic hyperthermia.

1.3.3.1 High intensity focused ultrasound

High intensity focused ultrasound (HIFU) is a hyperthermia technique that uses waves at a frequency of 2–20 MHz. The absorption of ultrasound energy deposits heat in the biological tissues. Ultrasound waves are able to attain deep sites and to focus power into small size regions [47]. HIFU has been reported as being benefical in provoking damage to cells and being able to focus to small regions for local hyperthermia. Nevertheless, they also come with disadvantages such as that the pressure waves are blocked by air and have difficulties in penetrating bone.

1.3.3.2 Radiofrequency ablation

Radiofrequency ablation (RFA) deposits heat by means of electric fields at frequencies of about 500 kHz. Electric energy then acts as heat source leading to temperature increase of the biological tissue [48]. RFA is based on the adequate conversion of electrical energy into thermal energy. During the RFA procedure, an electrode is guided into the cancer tissue using ultrasound, MRI, or CT scans.This can be done in a percutaneous manner. Radiofrequency current flows from the generator through the non insulated tip of the electrode into the tissue and follows the natural paths in the interstitium toward the dispersive electrode or grounding pad to form an entire electric circuit [49]. Next to using a single electrode with grounding pad, it is also possible to use multiple electrodes that can increase the extent of the region to which heat is applied to the biological tissue. Note that RFA is mostly used as thermotherapy to elevate temperature in the tumor to regions of 50-80°C, which is much higher than the temperature regions of hyperthermia [49].

1.3.3.3 Microwave hyperthermia

Microwave hyperthermia (MH) employs antennas working at 300 MHz to 300 GHz. These electromagnetic waves induces heat due to the rotation of polar molecules such as water together with ionic displacements [50]. Contrary to radiofrequency, microwaves can penetrate tissues containing air like lung tissues. It is also commonly used for the treatment of prostate or breast cancer in conjunction with other cancer therapies, such as radiation [51].

1.3.4 Magnetic nanoparticles hyperthermia

1.3.4.1 Magnetic nanoparticles

Magnetic nanoparticles (MNPs) have demonstrated many advantages in biomedical applications especially in diagnostics and therapeutics such as improving the quality of magnetic resonance imaging and hyperthermic treatment for malignant cells [52]. They consist of a magnetic core (single or multicore), of well-defined chemical composition, size and shape, a coating which ensures desired physicochemical properties and, possibly, a surface functionalization which gives them specific biological properties.The first experiments on the medical application of MNPs were performed by Gilchrist in 1957. In this study, iron oxides particles, having diameters of 20–100 nm, were injected in the intestinal wall of dogs with the expectation that the MNPs would end in regional lymph nodes. The regional lymph-nodes were then dissected and exposed to an alternating magnetic field of intensity 1.6–2 kA/m and frequency 1.2 MHz [53]. It was found that a concentration of 5 mg of magnetite per gram of lymph-node tissue yielded a temperature increase of 14°C in 3 min. Since then, there have been extensive and diverse works

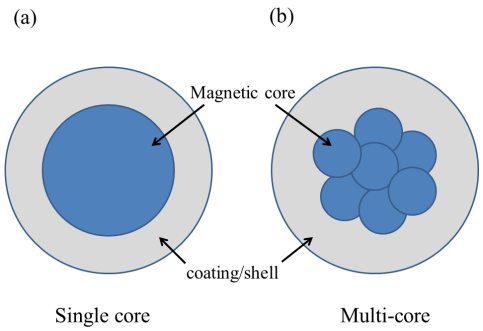

Figure 1.4: Scheme of single core and multicore magnetic nanoparticles with coating.

describing different alternating magnetic field (AMF) strengths and frequencies and variety types of MNPs. Most of the MNPs used clinically are covered with biocompatible coating. The role of the biocompatible coating is to avoid risks related to the toxicity of the magnetic core. For instance, although iron is largely present in the human body (about 50–60 mg of Fe per kg of body weight, mostly bound to transferrin), free iron is highly susceptible to oxidation. Consequently, in the cellular environment it reacts with water producing free radicals (in particular reactive oxygen species (ROS)) which causes oxidative stress and consequent cell damage. The most common coatings are derivatives of dextran, polyethylene glycol (PEG), polyethylene oxide (PEO), poloxamers and polyoxamines. Large numbers of biomedical studies focus on iron oxide nanoparticles as they have a more favorable toxicity profile compare to other MNP types containing manganese, nickel or cobalt [54] [55].

1.3.4.2 Clinical application of magnetic nanoparticles hyperthermia

Magnetic nanoparticles hyperthermia (MNH) consists of introducing magnetic nanoparticles (MNPs) inside the tumor and locally heating cancer tissue using an external alternating magnetic field (AMF), commonly at frequencies of around 200 kHz [56]. Depending on the duration of treatment and the temperatures achieved within the tumor tissue, the cancer cells are either irreparably damaged or sensitized for additional chemo- or radiotherapy. By exciting a magnetic coil with a time varying electrical current, the AMF can be generated. This coil can be placed outside the body where the generated AMF inside the body can interact with magnetic nanoparticles. We refer to Chapter 2 for further details on MNH. Here we shortly describe MNH currently used for clinical applications. The size of MNPs used in MNH is generally between 10 and 100 nm which gives them the ability to come in the vicinity of cancer cells. Dedicated magnetic nanoparticles with specific magnetic properties need to be synthesized to allow MNH. The reason is

that the repeated and selective heating of tumors requires the administration of a significant dose of MNPs, which must be kept in the body for all the treatment duration (typically more than one session scheduled at weekly intervals). The only magnetic materials currently allowed for clinical use are iron oxides, like magnetite (Fe_3O_4) and maghemite ($\gamma - Fe_2O_3$), because of their chemical stability against oxidation, low biological interaction and known pathways of metabolism. Other magnetic materials, like iron, nickel or cobalt, although characterized by better magnetic properties at nanoscale, cannot be used due to their strong reactivity in contact with the cellular environment. The first clinical trials on patients has been carried out by MagForce®. The approach includes the exposure system, MFH300F (1.5a), the injected MNP suspension, NanoTherm (1.5b), and a software, NanoPlan (1.5c), for the treatment planning [57]. The MFH®300F generates AMF at 100 kHz with amplitude variable between 0 and 18 kA/m in a cylindrical treatment volume of diameter of 20 cm and height of 30 cm. It can be used for tumor up to 5 cm, in all parts of the body. The NanoTherm®is a mixture of magnetite and maghemite particles having core size of 12–15 nm and coated with aminosilane. The MNPs are suspended in water at a concentration of 112 mgFe/ml. The treatment is planned through a software NanoPlan®, based on the Pennes bioheat transfer equation, which we will review in Chapter 4. The software receives the distribution of the injected MNPs in the tumor (as input data from CT scan) and the measured specific absorption rate (SAR) of the employed MNPs. Then, NanoPlan returns an estimation of the temperature distribution and the AMF amplitude required to achieve therapeutic heating of the tumor [58] [59].

Figure 1.5: MNH system developed by MagForce (a) MFH®300F applicator (b) NanoTherm®ferrofluid (c) Nanoplan®software (images available on line at www.MagForce.de

1.4 Hyperthermia for bone metastases

Bone is the most common site of cancer metastases [60]. It is a result of the spread of cancer cells from their initial site to the bone. Most types of cancers metastasize in advanced stage. Particulary, breast and prostate cancer are likely

to spread to bone making the spine and pelvis common sites of bone metastases [61]. In spinal metastatic cancer, the vertebral body is invaded and weakened by pathological tissue, which can lead to the collapse of the vertebral body and a progressive compression of the spinal cord. This in turn may lead to a severe neurological function deficit [62].

1.4.1 Spinal metastases

1.4.1.1 Spinal anatomy

The anatomy of the spine is depicted in Fig.1.6. The spinal cord is located near the vertebra where spinal metastases can occur. In between vertebrae, the inter vertebral disc is situated, making slight movements of the vertebra possible but also acting as a ligament, holding the vertebrae together. The descending aorta, in which blood flows at a flow rate of 3 to 7 liter/minute, runs rather close to the vertebrae. Also the inferior vena cava (IVC) is located near the vertebra. Via the IVC, deoxygenated blood returns to the heart.

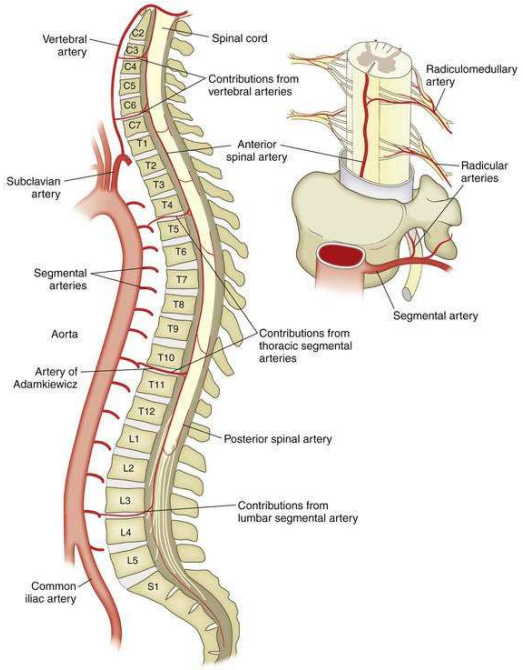

Figure 1.6: Anatomy of the spine including the spinal cord, the vertebrae and the inter vertebral discs. The aorta and the different arteries can be seen in left of the vertebral column [2].

In the cross-sectional view of Fig.1.7, the vertebral body can be seen as well as the

spinal cord. Starting at the brainstem, the spinal cord extends down to the region between the first and second lumbar vertebrae (L1 and L2 in Fig.1.6). Because the spinal cord is located in the direct vicinity of the vertebrae, the MNP hyperthermia treatment can heat it up, potentially harming the patient.

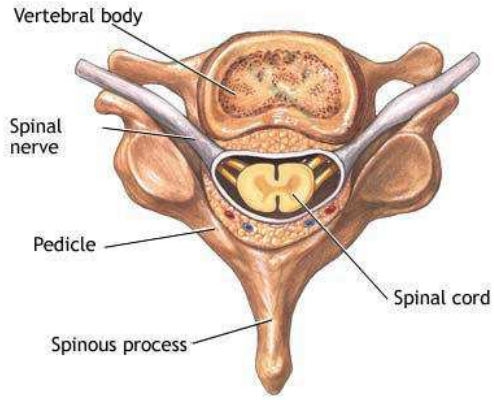

Figure 1.7: Cross section of vertebra region (www.sci-recovery.org).

1.4.1.2 Metastatic spinal tumor

As mentioned before, cancer cells can spread from an initial location and travel via blood or lymph system to a secondary location. In many cases, this metastatic location is the spinal region, where tumors can be formed in vertebrae. About 30% of patients with various neoplastic conditions develop symptomatic spinal metastases during the course of their illness, although it is hard to put an exact number to it [63].

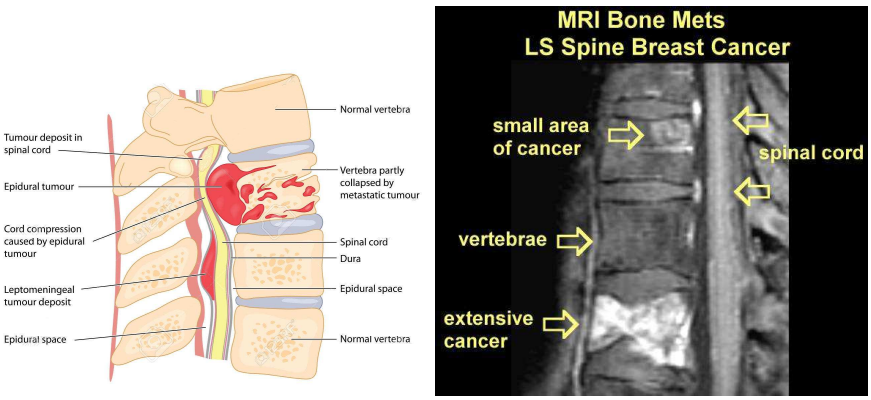

Figure 1.8: Lateral column view: schematic view (left) MRI image (right) [2].

A tumor can be formed in the anterior part of vertebrae (vertebral body). This can cause compression and fracture of the vertebrae and also compression on the spinal cord, which results in severe neurological function deficit [64]. The patient can experience pain in the spinal area caused by the tumor or due to mechanical pain of a collapsed/fractured vertebra. Operative and non-operative treatments can be applied for metastatic spinal tumors. Non-operative treatments consist of radiotherapy, hormone therapy and medication. The operative treatments involve reconstruction of the vertebrae via injection of PMMA or with use of a spine prothesis and stabilization with pedicle screws. The operative solution is associated with significant postoperative recovery and is seldom applied for patients with multifocal spinal disease.

1.4.1.3 Current treatments for bone metastasis

Current treatments of bone metastasis allow either stabilization or oncological treatment of the spinal column. Vertebral body augmentation by the injection of "bone cement", eg. polymethylmetacrylate, PMMA, so-called vertebroplasty, i.e. the direct injection of PMMA with high pressure device or kyphoplasty, i.e. making a cavity in the vertebral body with a balloon before filling it with PMMA at relatively low pressure, readily stabilizes the spine, but does not stop tumor progression [65]. Current spinal metastatic disease treatments, such as the standard and most common neurosurgery, radiofrequency ablation and laser induced thermotherapy techniques are performed before the injection of the cement and can thus be realized only once. Surgical procedures are possible for 10-15% of the patients, but because of the frequent progression of spinal metastases, the surgery needs to be repeated which is costly and unwanted for the patient. The treatment should ideally be performed in a repetitive way, without additional invasive manipulations. Traditional bone cement can be clinically administered in a minimally invasive way as it is being done in vertebroplasty or kyphoplasty, see Fig.1.9 and 1.10. Both techniques are well established in clinical use. In this dissertation we will load particles in the PMMA that can be used both for vertebroplasty or kyphoplasty. Fig.1.9 gives a view of the vertebroplasty procedure as can be seen with use of fluoroscopic imaging.

Figure 1.10 gives a view of the kyphoplasty procedure. First, a hole is drilled in the vertebra (3). Via the cannula (2), a biopsy needle (1) or the balloon is inserted in the vertebra. After inflation, PMMA is injected in the created void (5).

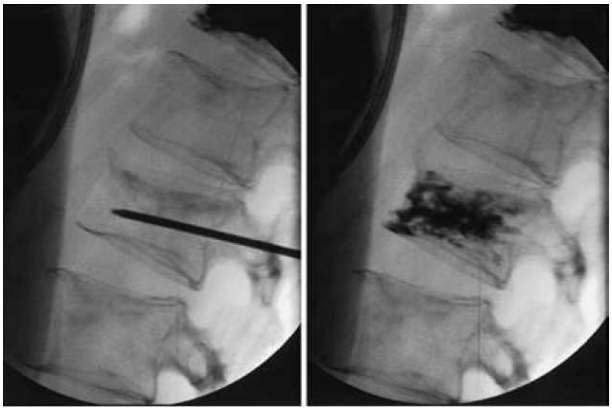

Figure 1.9: Vertebroplasty: view of vertebra before (left) and after (right) injection of PMMA [3].

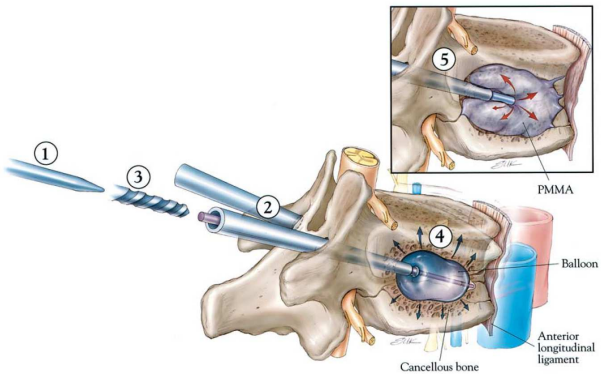

Figure 1.10: Five steps of kyphoplasty: 1 placement of a guide wire; 2 insertion of a working cannulas; 3 reaming of working channels; 4 inflation of the balloons, and 5 injection of polymethylmetacrylate [4].

The steps in the kyphoplasty surgery, as discussed above, can be visualised with fluoroscopic imaging as well. The result is the following sequence of: insertion, inflation of the balloon and eventually injection of PMMA.

1.4.2 Bone cement

Bone cement was for the first time used by the English surgeon, John Charnley, for total hip arthroplasty in 1958 [66]. He realized that bone cement can be used as a space filler and is easy to blend with the bone structure. Since 1970's, bone cement was approved by the U.S. Food and Drug Administration (FDA) for im-

plant fixation. Polymethyl methacrylate (PMMA) is the most common type of bone cement. It is widely used in diverse orthopaedic surgeries. Other types of commercially available bone cement like calcium phosphate cements (CPC) and Glass polyalkenoate (ionomer) cements (GPC) are successfully used in a variety of orthopaedic and dental applications. CPC and GPC are bioresorbable and biocompatible, but are mainly used in cranial and maxillo-facial surgeries because of their low mechanical strength. Thereby, PMMA is preferable for vertabrae surgeries.

1.4.2.1 Bone cement preparation

PMMA bone cements are made up of two components: a copolymer powder and a monomer liquid methylmethacrylate (MMA). The blend of the copolymer powder with the MMA monomer liquid forms the poly(methyl methacrylate) (PMMA) cement. These two components are mixed at an approximate ratio of 2:1 to start a chemical reaction called polymerization. It is an exothermic reaction inducing a temperature increase up to 80°C. The polymerization process can be divided into four different phases: mixing, waiting, working, and setting.

- Mixing Phase: The mixing phase represents the time taken to fully integrate the powder and liquid. As the monomer starts to dissolve the polymer powder, the benzoyl peroxide is released into the mixture. This release of the initiator benzoyl peroxide and the accelerator DMPT (N,Ndimethyl-para-toluidine) is actually what causes the cement to begin the polymerization process. It is important for the cement to be mixed homogeneously to minimize the number of pores.

- Waiting Phase: The cement takes several minutes to achieve a suitable viscosity for handling. Dough time is the time measured from the beginning of mixing to the point when the cement no longer sticks to hands. Under typical conditions (23°C-25°C, 65% relative humidity), dough time is about 2 to 3 minutes after beginning of mixing for most bone cements. Before this time, after the components are well mixed, the bone cement may be loaded into a syringe, cartridge, or injection gun for assisted application.

- Working Phase/Working Time: The working phase is the period during which the cement can be manipulated and inserted in the bone of the patient. The working phase results in an increase in viscosity and the generation of heat from the cement. The working time is the interval between the dough and setting times, typically 5-8 minutes.

- Setting Phase: During this phase, the cement hardens and sets completely, and the temperature reaches its peak. The cement continues to undergo both

volumetric and thermal shrinkage as it cools to body temperature. Setting time is the time measured from the beginning of mixing until the time at which the exothermic reaction heats the cement to a temperature that is exactly halfway between the ambient and maximum temperature, usually about 8-10 minutes. The temperature increase is due to conversion of chemical to thermal energy as polymerization takes place.

The dough, working, and setting times may be affected by different factors such as the mixing process, the ambient temperature and humidity. For instance, a fast mixing can accelerate dough time which is not desirable since the resulting bone cement may be porous. Furthermore, a high humidity accelerates setting time whereas low humidity retards it. Despite the fact that basic PMMA bone cement materials are the same, the behavior of various cement products can be significantly different when they are mixed under similar conditions. In fact, the size, shape and weight of the polymer molecules can vary considerably. Also, the manufacturing and sterilisation methods may differ from one company to another.

1.4.2.2 Mechanical properties of bone cement

Cement properties are critical during clinical use. Key properties are the porosity, viscosity and mechanical strength of the cement and are determined during the four polymerization phases explained in section 1.4.2.1. These properties will influence cement handling, penetration, and interaction with the bone.

Cement Porosity: Porosity is the ratio of the volume of all the pores in a material to the total volume. High bone cement porosity compromises the cement's mechanical strength and decreases its fatigue life. Trapped air in the cement during mixing and the transfer from mixing container to application device are the main sources of porosity. Hand mixing bone cement in an open bowl may introduce the greatest possibility of these occurrences, which is why hand-mixed cement can contain a substantial number of pores. Centrifugation and vacuum mixing methods can reduce the porosity of bone cement [67].

Cement Viscosity: Cement viscosity determines the handling and working properties of the cement. Mixing together the powder and the liquid components marks the start of the polymerization process. During the reaction, the cement viscosity increases, slowly at first, then later more rapidly. During the working phase, there are two requirements for bone cement viscosity – it must be sufficiently low to facilitate the delivery of the cement dough to the bone site, and it must penetrate into the interstices of the bone [68]. On the other hand, the viscosity of the bone cement should be sufficiently high to withstand the back-bleeding pressure, thus avoiding the risk of inclusion of blood into the cement because this could significantly reduce the stability of the bone cement. It is important that the cement retains an optimized viscosity for an adequate duration to allow a "comfortable"

working time.

Mechanical Properties: The aim of a good cement mixture is to produce bone cement that has the best mechanical properties possible so that it can carry out its load transfer role successfully over the lifetime. Once positioned within the bone the cement is subjected to a series of physical forces that will have an effect on the lifespan of the cement. These physical forces subject the cement to fatigue, creep and high stresses [69]. The mechanical properties of the cement (eg. resistance to fatigue and strength) should be enhanced as much as possible.

1.4.2.3 Bone cement loaded with magnetic particles

From the previous section 1.4.1.3 on vertebro- and kyphoplasty, it is clear that both procedures aim to stabilize/restore a fractured or compressed vertebra. Tumour progression on the other hand is not stopped. The treatment of the metastatic spinal tumor is thus performed once, before the vertebra is restored with PMMA [70]. However, spinal metastases often progresses, resulting in the necessity to repeat the surgical procedure, which is costly and unwanted for patients. This is where the principle of loading the PMMA with magnetic nanoparticles comes in to play. In this way, both the vertebra is restored mechanically, with use of the PMMA, and tumor treatment can be continued with the presence of the magnetic nanoparticles and application of an alternating magnetic field. MNPs can be mixed with the PMMA powder with a restricted concentration of MNPs to not alter the mechanical properties of the PMMA, see also the former section 1.4.2.2. The polymerization of the PMMA-MNP can be achieved directly in the core vertebra using the same delivery system as in vertebroplasty. A cavity can be created in the vertebra by removing the tumor area. The cement mixed with the nanoparticles is placed in the center of the cavity using a needle in the pedicles. Then MNPs are activated through the externally generated AMF so that they heat the PMMA and thus the surrounding biological tissue [71]. This procedure enables on the one hand the stabilization of the bone and on the other hand the hyperthermia of the spinal metastatic tumors. The effectiveness of hyperthermia largely depends on the precision of having temperature increase in the tumor and minimizing the heating of normal tissue elsewhere.

1.5 Research objectives, prerequisites and challenges

In this section we elaborate on the main research objectives of this dissertation and highlight the prerequisites of the work. To attain the objectives and to comply with the requirements, several challenges are faced in a multi-/interdisciplinary context. This work considers aspects of:

- **Electrical energy engineering** based on low frequency electromagnetic principles, we aim at manufacturing a dedicated AMF source.

- **Material engineering** the AMF source interacts with magnetic nanoparticles that are loaded in PMMA where dedicated material models provide insights on the heat source that particles produce under an AMF.

- **Biomedical engineering** these heat sources result in elevated temperatures in biological tissues that can be assessed using numerical modelling incorporating geometrical and tissue properties and that ultimately leads to damage of spinal metastases.

1.5.1 Research objectives

The combination of the above disciplines were crucial to tackle the main overall objective of this dissertation: find solutions that enable hyperthermia of spinal metastases ultimately providing a novel hyperthermia modality as therapy for spinal metastases that goes beyond the state of the art. PMMA is used in clinical practice to stabilize the spine whereas in this work we load the PMMA with particles that in presence of an AMF become heat sources so that we can establish both mechanical stabilization of the spine and hyperthermia in the vicinity of spinal metastases. To reach the above mentioned overall objective we need to comply with basic prerequisites:

- To attain higher magnitudes of heat sources and thus elevated temperatures one can aim at increasing the AMF magnitude and frequency which however faces difficulties in the electrical circuits and power supply to meet this requirement. An introduction to the associated challenges is provided in subsection 1.5.2.1.

- On the other hand, AMF induces eddy currents in the biological tissue and can become painful for the patient leading to the local heating of the healthy biological tissue and can moreover at certain levels of frequencies and magnetic fields result in nerve and cardiac stimulation. Challenges associated to this requirement is sketched in subsection 1.5.2.4.

- Another way of increasing the heat source is to increase the concentration of particles in the PMMA-particles mixture. Having too high concentration of particles may however result in the weakening of the mechanical stability of the PMMA-particles mixture. Challenges associated to this requirement are introduced in subsection 1.5.2.2.

- Next to mechanical weakening, inserting particles in the body need to be biocompatible but also MRI compatible so that it remains possible to adequately image the tumor region after treatment. See subsection 1.5.2.3.
- Finally, the temperature distribution in the spine needs to be controlled to not have too high temperature increases to the spinal cord. See also subsection 1.5.2.4 for an introduction on the challenges to limit the effects on the environment.

Satisfying these requirements to meet the overall objective led to the following focused innovation goals: (1) Engineer an adequate AMF source (2) Load the PMMA with suitable particles that result in sufficient heat source and that satisfy the above mentioned requirements (3) Assess the temperature distribution in the spine and specifically the cell damage in the spinal metastases. These three innovation goals are detailed in chapters 2, 3 and 4. Achieving these three goals leads to enabling magnetic hyperthermia of spinal metastases by loading the PMMA-based bone cements with magnetic particles.

1.5.2 Basic prerequisites for hyperthermia of spinal metastases

1.5.2.1 Technical challenges for generating the alternating magnetic field

A first technical challenge is to engineer a device capable to produce sufficient heat at a predefined distance from the AMF source. The AMF can be produced by means of a resonant inductor-capacitor circuit that is characterized by the inductance (L) and the capacitance values of the circuit (C). The inductance is generally a magnetic coil consisting of a number of windings that determine L. A capacitance C can be realized by means of e.g. two conducting plates with a distance between each other and where a dielectric material is inserted. The circuit is a closed circuit where the inductor and the capacitor are connected in series or parallel. Since the circuit is a closed circuit, resonance may occur where energy is stored in two ways; electric energy as electric field due to the charging of the capacitor and magnetic energy as magnetic field due to the electrical current flowing through the inductor. Energy is transferred from the electrical to the magnetic domain within the circuit and vice versa. Note that the inductor as well as the capacitor have a certain resistance (R) so that in fact we have a RLC resonance circuit. The resistance does not affect the resonance frequency at which the circuit operates but does affect the resonance peak of the electric current magnitudes flowing in the circuit. Increasing resistor values lead to increasing decay of these oscillations, i.e. damping. The resonance frequency of the RLC circuit is $f_r = \frac{1}{(2\pi\sqrt{LC})}$. The capacitors used in the capacitors bank of the circuit have a restricted value which define the theoretical maximum current I allowed to flow through these capacitors. The heating station is composed of a coil with a variable number of turns.

By increasing the number of turns in order to obtain a higher AMF, the inductance coefficient L rises whereas the resonance frequency decreases. Therefore, smaller capacitance C should be used to keep the resonance frequency at the same level. A first alternative to obtain a higher AMF is to increase the current flowing through the coil. A second option for the enhancement of the generated heat is to increase the MNPs concentration. Here again, there are mechanical constraints further discussed in Chapter 3.

1.5.2.2 Mechanical stability of PMMA-particles mixture

Next to increasing the AMF, the second alternative to have an efficient temperature increase during MNH treatment is the use of high concentration of MNPs. Increasing the particles concentration has however an impact on the mechanical stability of the PMMA-MNP mixture. Various aspects of the mechanical properties of bone cements and particularly PMMA mixtures have been investigated in earlier studies such as in [69] [72]. In these studies, MNPs were dispersed in the cement matrix and it has been shown that the maximum particles content was around 60 wt.$\%$ vs. the total weight of the PMMA-MNP mixture in order to ensure mechanical stability. In this work, we considered this limit as prerequisite in the development of a hyperthermia modality with PMMA-MNP mixtures.

1.5.2.3 MRI and particles biocompatibility

The issue of biocompatibility in magnetic nanoparticle based hyperthermia can be seen from various perspectives. In typical MNH procedure, biocompatibility concerns the ability of the MNPs to be metabolized by the human body with no or tolerable adverse effects. This depends on several factors such as the chemical nature of the magnetic core, type of coating, aggregation and concentration of MNPs. In the case of MNH for bone metastases, the effects of MNPs degradation may be neglected as the MNPs are trapped in the PMMA matrix and unable to spread throughout the body. However, the MNPs concentration and the type of core are essential requirements for the magnetic resonance imaging (MRI) diagnosis and the follow-up of bone metastasis [73]. In fact, the presence of metal core such as MNPs causes artefacts on MRI which leads to misinterpretation of imaging results and the inability to conclude a diagnosis [74] [75]. MRI artefacts depend on the concentration of MNPs and the size and orientation of the magnetic core with regard to the direction of the AMF. It is for instance conventionally known that ferromagnetic implants produce more artefacts than the titanium ones. Consequently, an appropriate choice of the magnetic core and the concentration of the MNPs need to be adjusted to the limits of the MRI procedure. In order to keep an effective concentration of MNPs, alterations to the MRI protocol can help reduce artefacts, such as the choice of pulse sequence and the direction of the magnetic

field. For instance, the artefact size increases proportionally with an increase in the angle between the long axis of the magnetic implant and the main magnetic field direction [76].

1.5.2.4 Limitations related to the biological environment

Heat effects on the spinal cord and thermotolerance: When the particles act as heat sources because of their presence in the AMF, the temperature diffuse throughout the biological tissue. It is of paramount importance to assess how the temperature distribution evolves spatially and temporally since we may damage healthy tissue. Furthermore, in bone metastases, exposing the spine to high temperatures due to an uncontrolled heat process may subsequently cause neuronal damage and lead to paraplegia, i.e. paralysis of the lower half of the body. Animal experiments indicate that the effect of the MNH on the spinal cord depends on the exposure time and how fast the maximum temperature is reached. In [77], the maximum temperature tolerated for the spinal cord is situated in the range of 42–42.5°C for exposure times of 40–60 min. In case temperatures in the order of 43°C are applied, the exposure time needs to be reduced to 10–30 min [78] [77]. Another study was done in the epidural space where the spinal cord was heated to a maximum of 47°C instantly and for 30 minutes. The heat effect was appraised by measuring the spinal cord evoked potential (SCEP), i.e. an electrical potential recorded from the nervous system following presentation of a stimulus. The heat caused instantly the SCEP to increase inversely proportional to the increase in the temperature. Maintaining heating for 30 minutes and for temperatures lower than 44°C, the SCEP amplitudes decreased by 25% to 75% of the control value in the first 5 minutes and recovered to over 75% of the control value in 30 minutes. The amplitudes returned approximately to their control value after bringing back the spinal cord temperatures to their normal temperatures. Nevertheless, at 45°C and above, the amplitudes were reduced or disappeared in the first 5 min and never returned to the initial values. These results indicate that in the epidural space 44°C is the highest tolerable temperature for normal spinal cord function [79].
On the other hand, transient exposure of cells to temperatures between 43 and 45°C during short periods of time, ranging from 10 to 30 minutes increased heat resistance known as thermotolerance. In this phenomenon, cells become more resistant to such high temperature [80] [81]. The effect of heat on cells were already introduced in section 1.3.1.
Skin burn due to eddy currents: When an AMF is applied to a conductive medium, like the human body, it generates eddy currents in the medium, whose intensity increases as the magnetic field amplitude H and frequency f of the AMF increases. Therefore, increasing the magnetic field also increases the unwanted heating produced in the healthy tissue. In clinical magnetic hyperthermia, this issue has been addressed by requiring that the product $H{\times}f$ does not exceed the

safety threshold of $4.85 \times 10^8 \frac{A}{ms}$. This constraint dates back to 1984 when Atkinson *et al.* [56] performed some clinical tests on the tolerability of the effects of eddy currents induced by the application of radiofrequent AMF with different H and f values. In this study, a single-turn coil was placed around the chest of healthy volunteers. Atkinson *et al.* found that field intensities up to 35.8 A turns/m, at a frequency of 13.56 MHz, can be thermally tolerated for extended periods of time. Afterwards, Brezovich *et al.* used Atkinson's results to establish the aforementioned safety threshold as upper bound for the product $H{\times}f$ assuring minimal patient's discomfort and that is tolerable when having treatment durations of 1 h [82]. This is an empirical rule as it relies on the patient's discomfort and not on the actual heating produced by the eddy currents. Moreover, it does not take into account the extent and the anatomy of the region to be exposed and the magnetic field spatial pattern within the exposed tissue, both influencing the amplitude of the induced eddy currents. For instance, as the eddy currents intensity decreases by reducing the extent of the exposed region, it is reasonable to expect that the above threshold in most cases underestimates the employable values of H and f, especially in cases where the extent of the region exposed to the field is smaller than that of the chest. For this reason in many experiments this quite stringent upper bound is often arbitrary increased, up to 30–40 times, leading to the opposite problem, i.e. to an overestimation of the allowed $H{\times}f$ for a safe treatment. In this thesis the $H{\times}f$ limit is a prerequisite towards developing a hyperthermia modality for spinal metastases so that we do not end up with a modality that is unrealistic for clinical usage.

1.6 Outline of the dissertation

In order to achieve the goals set forward in this dissertation, we detail the aspects considered in the upcoming chapters. Fig.1.11 schematically depicts the different mechanisms that are considered in this dissertation.
In Chapter 2 we provide an introduction to magnetic hyperthermia where a magnetic heating device consisting of an inductor-capacitor circuit gives rise to a certain alternating magnetic field (AMF). This is represented by the function f_{AMF} in Fig.1.11. A time-varying electric current flowing through an inductor, i.e. a tube wound into a coil, generates a magnetic field. How the tube is wound affects the magnetic field amplitude (H) and specifically the magnetic field decay at a certain distance from the inductor. Since the magnetic hyperthermia device needs to be placed outside the patient, it is paramount to achieve a certain level of magnetic field at a distance from the inductor. The geometrical properties of the inductor give rise to the characteristic inductance (L) of the inductor and together with the capacitance (C) they determine the resonance frequency (f_r) at which the AMF varies. A magnetic analysis on the effect of the inductor-capacitor parameters on

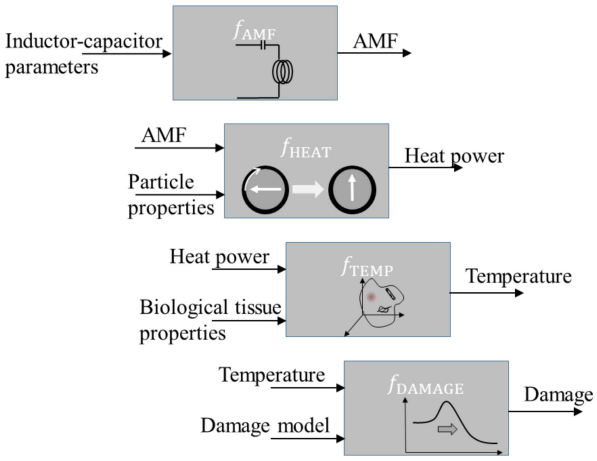

Figure 1.11: Schematic presentation of the key mechanisms for realizing hyperthermia on the basis of particles. Having a certain AMF is function (f_{AMF}) of the inductor-capacitor parameters (Chapter 2); the heat power of particles is function (f_{HEAT}) of the AMF and particles properties (Chapter 3); the temperature/damge distribution in biological tissue is function (f_{TEMP}/f_{DAMAGE}) of the heat power and the thermal/damage biological tissue properties (Chapter 4). In Chapter 5 all mechanisms are integrated to realize hyperthermia of spinal metastases based on the heating of particles loaded in PMMA.

the AMF is provided in this chapter. We also study the technological limits related to the hyperthermia device for attaining high levels of AMF at the site of the spine. We evaluate whether and when the prerequisite of limiting the unwanted heating by eddy current of healthy tissues is satisfied.

Chapter 3 details the heating power that particles can realize when subjected to an AMF. The influence of the type and properties of the particle such as their size, magnetic and nonmagnetic properties on the heating power is studied. This is represented by the function f_{HEAT} in Fig.1.11. We omit the particles to realize heating by Brownian motion since they are fixed in a PMMA matrix. To assess the effect of magnetic particle properties in an AMF on the heating power, simulations are performed. We also evaluate the heating efficacy of non-magnetic particles where heating can occur due to eddy currents dissipated in the particles. We evaluate whether and when the prerequisite of maintaining mechanical stability of the PMMA-particles material is maintained, as well as its MRI compatibility, since these can be infringed by having too high concentrations of particles.

Chapter 4 provides a behavioral model based on Pennes' bioheat equation that allows to calculate temperature distributions in space and time within biological tissues for given heating power, and geometrical and thermal properties of biological

tissues. Based on a simplified model of the spine we perform thermal analyses on the effect of the heating power of particles in PMMA and biological tissue properties on the temperature (function f_{TEMP} in Fig.1.11). We also appraise whether and when we satisfy the prerequisite of not reaching too high levels of temperatures in healthy tissues. We also include in this chapter damage models that provide a means to measure the extent of inflicting damage to biological tissues. We assess the effect of the damage model (function f_{DAMAGE} in Fig.1.11) and evaluate the possibility of performing hyperthermia for treating spinal metastases.
In Chapter 5 we experimentally realize heating in an *ex-vivo* experiment for an inductor-capacitor circuit located at a certain distance from magnetic particles in a PMMA matrix.

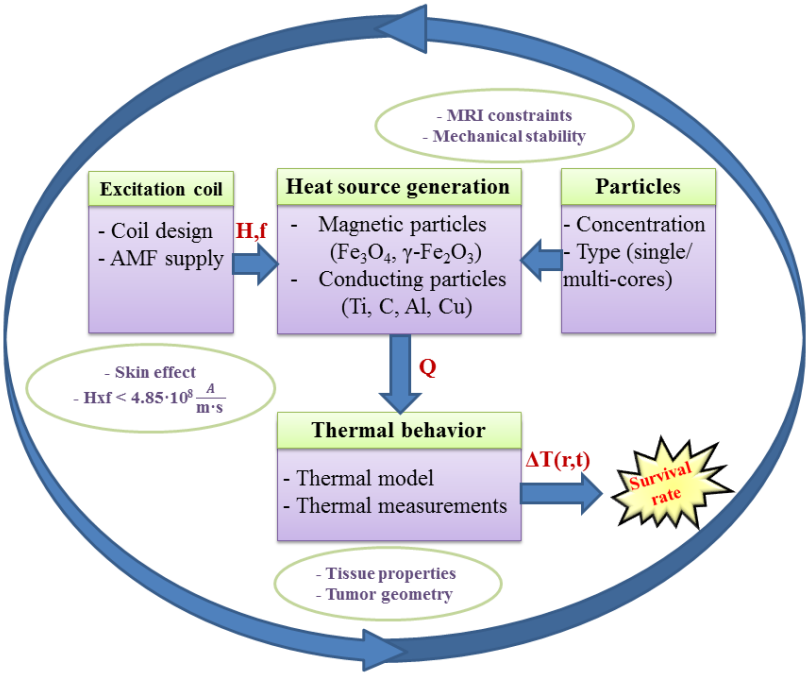

Figure 1.12: Overview of the technical parameters involved in magnetic hyperthermia

2

Alternating magnetic field generation

'Divide each difficulty into as many parts as is feasible and necessary to resolve it.'

Rene Descartes

2.1 Introduction

This Chapter considers the alternating magnetic field that is generated by the inductor-capacitor circuit for hyperthermia. We start this chapter with providing the fundamentals of the inductor-capacitor circuit (Section 2.2) that is in essence a resonant electrical circuit with resonance frequency characterized by the self-inductance (excitation coil) and capacitance (capacitor bank) values of the circuit. In Section 2.3, the governing equations in low frequency electromagnetism are introduced that are related to the magnetic field that the current carrying excitation coil generates. We also introduce the self-inductance value of a coil as they are primordial to take into account as this affects the resonance frequency. In the subsequent section 2.4, analytical descriptions are provided to calculate the magnetic field amplitudes and self-inductance values of three different coil topologies: short cylindrical, helical, and pancake coil. We also assess their validity by comparing the analytical results with finite element based simulations. Starting from the valid models we analyze the possibilities and limitations of generating sufficient alternating magnetic fields for large animals and human bodies that ultimately can be

used for hyperthermia treatment purposes. We perform an in-depth analysis for exploiting magnetic fields inside the coils (Section 2.5) and outside the coils (Section 2.6). For the latter we analyze the proper coil topology to maximally generate a magnetic field strength at a certain distance from the excitation coil. We furthermore perform a geometrical optimization of the coil that maximizes the magnetic field for various self-inductance values. Finally, Section 2.7 analyzes whether and how the electrically conducting human body attenuates the alternating magnetic field because of shielding effect. We also assess the induced eddy currents in the human body. We conclude this chapter by providing insights on the optimal excitation coil for treating bone metastases.

2.2 Fundamentals of the inductor-capacitor circuit

A magnetic heating device typically consists of a high frequency power supply, a magnetic excitation coil (inductor) and a capacitor bank. The high frequency supply converts electrical power from the 50 Hz grid to a high frequency power, having a frequency f in the range of 150-700 kHz. The high frequency power is connected to a capacitor bank and the magnetic excitation coil. By means of this high power resonant inductor-capacitor, a sufficiently high electrical AC current is generated in the magnetic excitation coil, giving rise to an alternating magnetic field (AMF).
Magnetic nanoparticles that are subject to this AMF will generate heat. The amount of heat depends on the characteristics of the magnetic nanoparticles, the design of the magnetic excitation coil (with inductance L) and the capacitance (denoted as C) of the capacitor bank connected to the power supply. Further details on the heat generation mechanisms are provided in Chapter 3.
The inductor-capacitor LC circuit can be implemented into two configurations, as schematically sketched in Fig. 2.1: as series resonant circuit (Fig. 2.1(a)) or as parallel resonant circuit (Fig. 2.1(b)). The choice mainly affects the design of the high frequency supply (with voltage V) which is out of scope of this dissertation. The series resonant circuit is one of the most important elementary circuits and we focus for simplicity on the series circuit. The total impedance in series seen by the high frequency supply is given by

$$\underline{Z} = R + j(\omega L - 1/\omega C) \tag{2.1}$$

with j the imaginary unit and $\omega = 2\pi f$ the angular frequency of the current flowing through the magnetic excitation coil and capacitor bank. The impedance (2.1) is a complex number. Multiplying a phasor current $\underline{I}$ by the impedance gives the phasor voltage $\underline{V}$. A phasor is in this dissertation denoted by $\underline{\cdot}$ and is a complex number representing a sinusoidal function whose amplitude, angular frequency

and initial phase are time-invariant. The phasor current $\underline{I}$ in the series resonant circuit for a given voltage of the power supply $\underline{V}$ is

$$\underline{I} = \frac{\underline{V}}{\underline{Z}} = \frac{\underline{V}}{R + j(\omega L - 1/\omega C)} \tag{2.2}$$

The current in the resonant circuit is maximal if

$$\omega L = \frac{1}{\omega C} \tag{2.3}$$

when inspecting the denominator of (2.2). In other words, the current flowing through the inductor capacitor is maximized when L and C are chosen in such a way that the frequency of the power supply equals the resonance frequency:

$$f_r = \frac{1}{2\pi\sqrt{LC}} \tag{2.4}$$

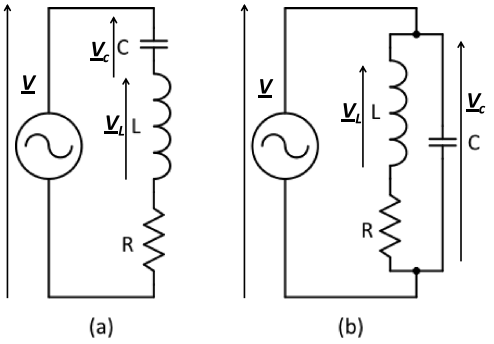

Figure 2.1: Resonant electrical circuit in series (a) and parallel (b) of the magnetic nanoparticle heating system

In order to control the amplitude of the current (2.2) flowing through the coil, there are two possible ways: (i) modifying the amplitude of $\underline{V}$ at resonance frequency in order to obtain the required amplitude of the current $\underline{I}$; or (ii) with a fixed value of the amplitude of $\underline{V}$, modifying the frequency f, in such a way that the difference with respect to the resonance frequency f_r results in the required amplitude of $\underline{I}$. When operating the inductor-capacitor circuit at resonance frequency f_r, the current flowing in the circuit is $\underline{I} = \frac{\underline{V}}{R}$. The voltage over the capacitor bank and the excitation coil have, compared to the voltage of the power supply, a large amplitude

$$|\underline{V}_C| = |\underline{V}_L| = |\omega L \underline{I}| = |\underline{I}/\omega C| \tag{2.5}$$

They however compensate each other since the power supply voltage is $\underline{V} = R\underline{I}$. The capacitor bank is practically realized by N_p parallel branches, each branch consisting of N_s capacitors connected in series. When having identical capacitors C_1, the total capacitance of the capacitor bank then becomes

$$C = C_1 \frac{N_p}{N_s} \tag{2.6}$$

Each capacitor in the capacitor bank has limitations with respect to the maximal current that may flow through the capacitor ($I_{C_1,\text{max}}$) as well the voltage over the capacitor ($V_{C_1,\text{max}}$): $|\underline{I}_{C_1}| < I_{C_1,\text{max}}$ and $|\underline{V}_{C_1}| < V_{C_1,\text{max}}$.

2.3 Magnetic fields generated by the coil

The electrical current flowing through the magnetic excitation coil in the inductor-capacitor circuit at a certain amplitude and frequency gives rise to a certain alternating magnetic field. Maxwell's equations (Section 2.3.1) with the Biot-Savart law (Section 2.3.2) allow to calculate the magnitude of the AMF. The self inductance coefficient (L) of the magnetic excitation coil can be derived from the stored magnetic energy in the coil, detailed in Section 2.3.3.

2.3.1 Maxwell's equations

Maxwell's equations are a set of fundamental equations that govern all macroscopic electromagnetic phenomena. The equations can be written in both differential and integral forms. The equations in differential form are given by:

$$\nabla \times \mathbf{E} = -\frac{\partial\, \mathbf{B}}{\partial t} \qquad \text{(Faraday's law)} \tag{2.7}$$

$$\nabla \times \mathbf{H} = \frac{\partial \mathbf{D}}{\partial t} + \mathbf{J} \qquad \text{(Maxwell-Ampère law)} \tag{2.8}$$

$$\nabla \cdot \mathbf{D} = \rho \qquad \text{(Gauss's law - electric)} \tag{2.9}$$

$$\nabla \cdot \mathbf{B} = 0 \qquad \text{(Gauss's law - magnetic)} \tag{2.10}$$

where

E = electric field intensity [V/m]
D = electric flux density [C/m^2]
H = magnetic field intensity [A/m]
B = magnetic flux density [Wb/m^3]
J = electric current density [A/m^2]

ρ = electric charge density [C/m^3]

Another fundamental equation, known as the equation of continuity, is given by

$$\nabla \cdot \mathbf{J} = -\frac{\partial \rho}{\partial t} \tag{2.11}$$

This equation, which can be derived from (2.8) and (2.9), is the mathematical form of the law of the conservation of charge. Depending on the material characteristics wherein the electromagnetic phenomena occur, the field quantities can be related to each other via the constitutive relations. The constitutive relations describe the macroscopic properties of the medium being considered. For an isotropic, linear and homogeneous medium, the constitutive relations are

$$\mathbf{D} = \epsilon \mathbf{E} \tag{2.12}$$

$$\mathbf{B} = \mu \mathbf{H} \tag{2.13}$$

$$\mathbf{J} = \sigma \mathbf{E} \tag{2.14}$$

where the constitutive parameters ϵ, μ and σ denote, respectively, the permittivity [F/m], permeability [H/m] and electrical conductivity [S/m] of the medium. In case the media is anisotropic, these parameters need to be represented as tensors; and in case of isotropic media as scalars. For inhomogeneous media, they are functions of position, whereas for homogeneous media they are not. In this work, we will only consider linear homogeneous media, except mentioned otherwise.

When field quantities in Maxwell's equations are sinusoidal functions, the field is referred to as as being time-harmonic. Using the complex phasor notation, (2.7)-(2.10) can be written in a simplified form as

$$\nabla \times \underline{\mathbf{E}} = -j\omega \underline{\mathbf{B}} \tag{2.15}$$

$$\nabla \times \underline{\mathbf{H}} = j\omega \, \underline{\mathbf{D}} + \, \underline{\mathbf{J}} \tag{2.16}$$

$$\nabla \cdot \, \underline{\mathbf{D}} = \rho \tag{2.17}$$

$$\nabla \cdot \, \underline{\mathbf{B}} = 0 \tag{2.18}$$

when the time convention $e^{j\omega t}$ is used and ω is the angular frequency. It is evident that the static case is the limiting case of the harmonic fields as the frequency $f = \omega/2\pi$ approaches zero. The electromagnetic quantities calculated in this chapter are based on the equations above. The equations can be calculated analytically

when considering simplified geometries and numerically with the finite element method when having more complex geometries.

2.3.2 Biot-Savart law

When the field quantities do not vary with time (static) or the time-dependent phenomena can be neglected (quasi-static), Maxwell's equations (2.7)-(2.10) reduces to

$$\nabla \times \underline{\mathbf{E}} = 0 \tag{2.19}$$

$$\nabla \times \underline{\mathbf{H}} = \underline{\mathbf{J}} \tag{2.20}$$

$$\nabla \cdot \underline{\mathbf{D}} = \rho \tag{2.21}$$

$$\nabla \cdot \underline{\mathbf{B}} = 0 \tag{2.22}$$

resulting in decoupled electric and magnetic phenomena. In case of considering air coils where the electromagnetic fields are in a medium with absence of magnetic materials or where the presence of magnetic materials may be neglected such as magnetic nanoparticles having a sufficiently low concentration, the constitutive law (2.9) is $B = \mu_0 H$ that holds in each point in space. $\mu_0 = 1.257\,10^{-6}$ H/m is the permeability of free space and can be used as the permeability of biological tissues.
Using this constitutive law, the solution of (2.16) and (2.18) is given by Biot-Savart law. Here, the magnetic field $\underline{\mathbf{H}}$ at a certain spatial coordinate $\mathbf{r}$ can be calculated by integrating over the volume of the conductor V_c where a current density $\underline{\mathbf{J}}(\mathbf{s})$ is flowing at coordinate $\mathbf{s}$. This gives rise to the following expression:

$$\underline{\mathbf{H}}(\mathbf{r}) = \frac{1}{4\pi} \int_{V_c} \frac{\underline{\mathbf{J}}(\mathbf{s}) \times (\mathbf{r} - \mathbf{s}) \mathrm{d}\upsilon_s}{|\mathbf{r} - \mathbf{s}|^3} \tag{2.23}$$

For any shape of the conductor within which an electric current flows (specified by V_c), this magnetic field $\underline{\mathbf{H}}$ can be computed by e.g. a finite element method. Notice that in the case the displacement current density $j\omega\underline{\mathbf{D}}$ in (2.16) can not be neglected, the following expression for the time harmonic magnetic field needs to be considered:

$$\underline{\mathbf{H}}(\mathbf{r}) = \frac{1}{4\pi} \int_{V_c} \frac{(\underline{\mathbf{J}}(\mathbf{s}) + j\omega\underline{\mathbf{D}}) \times (\mathbf{r} - \mathbf{s}) \mathrm{d}\upsilon_s}{|\mathbf{r} - \mathbf{s}|^3} \tag{2.24}$$

Fig. 2.2 depicts relevant coil geometries that are considered in this thesis. We distinguish between cylindrical coils (a), pancake coils (b), and butterfly type coils

(c). The geometrical properties of these coils, i.e. the coordinates **s** where electrical current is flowing through the conductor of the coil, affect the spatial distribution of the magnetic field $\underline{\mathbf{H}}$ as can be observed from equation (2.23) and (2.24).

2.3.3 Self inductance coefficient L of a coil

When a DC electric current I_m is flowing in the inductor with a self inductance coefficient L, there is energy w_m stored in the magnetic field H. It is well known that the stored magnetic energy is related to the self inductance coefficient L of the coil as being:

$$w_m = \int_V (\frac{1}{2}\mu_0 H^2)\mathrm{d}V = \frac{1}{2}LI_m^2 \tag{2.25}$$

which allows to quantify the inductance coefficient starting from the field pattern H in and around the coil (volume V).
Expression (2.25) is also valid for an instantaneous current $i(t)$. In the case of a sinusoidal current $i(t) = I_m \cos(\omega t)$, the instantaneous stored magnetic energy becomes

$$w_m(t) = \int_V (\frac{1}{2}\mu_0 H^2(t))\mathrm{d}V$$

$$= \frac{1}{2}Li^2(t) = \frac{1}{2}LI_m^2 \cos^2(\omega t) = \frac{1}{4}LI_m^2(1 - \cos(2\omega t)) \tag{2.26}$$

Note that the time varying magnetic field is here space (**r**) dependent, cfr. equations (2.23) or (2.24). The relation between the flux linkage $\psi(t)$ of the coil and the current $i(t)$ flowing through the coil like in the resonant electrical circuit of Fig.2.1 is directly described by the self inductance coefficient L: $\psi(t) = Li(t)$. For the cylindrial coils, pancake coils and butterfly type coils, a certain magnetic field distribution $\underline{\mathbf{H}}(\mathbf{r})$ within the volume V in and around the coil can be calculated using Biot-Savart's law where it is apparent that for each coil type this results in different self inductance coefficients L.

2.4 Analytical description of magnetic fields generated by the coil

In the next subsections, we will assume a current flowing in a set of thin wires or curves in order to simplify the quantification of the magnetic field. Thinking in these terms will give rise to simplified models, however already resulting in valuable conclusions with respect to the effect of coil topologies on their magnetic properties, i.e. the spatial distribution of magnetic fields and their self inductance.

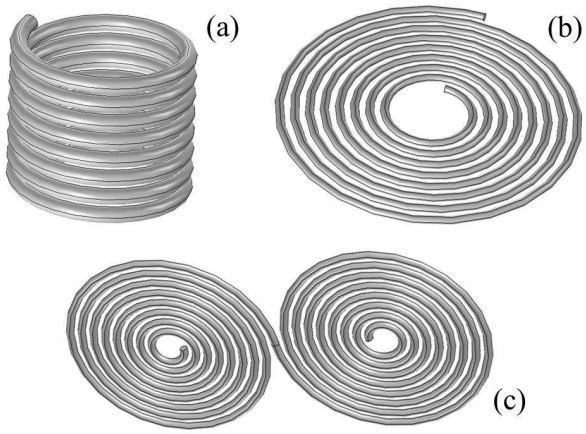

Figure 2.2: Relevant geometries for the coils considered (a) cylindrical/helical coil (b) pancake coil and (c) butterfly coil

2.4.1 Magnetic field due to a current in a one turn circular coil

As a first approximation, in order to simplify equations, one may introduce the principle of basic current elements. The basic current element I d$\mathbf{l}_1$ in point P_1 of Fig. 2.3 is the source for a magnetic field $d\mathbf{H}$ in point P:

$$d\mathbf{H} = \frac{Id\mathbf{l}_1 \times \mathbf{1}_r}{4\pi r^2} \tag{2.27}$$

Here, $\mathbf{1}_r$ is the unit vector along the line connecting the point P and P_1. The orientation of this unit vector is from P_1, the source point of I d$\mathbf{l}_1$, to P, the point in which we want to know the magnetic field $d\mathbf{H}$. The symbol r denotes the distance between the points P and P_1.
The magnetic field in an arbitrary point P due to a current I in a one turn circular coil with radius R, as in Fig. 2.3, can be computed by considering the contribution of each basic current element I d$\mathbf{l}_1$, of the one turn coil and integrating over the conductor represented as a filament

$$\mathbf{H} = \oint \frac{Id\mathbf{l}_1 \times \mathbf{1}_r}{4\pi r^2} \tag{2.28}$$

For a point P_3 at a distance z from the plane of the circular current filament and on the axis through the center of the circle and perpendicular to the circle, the amplitude of the AMF equals

$$H_3(z) = \frac{IR^2}{2(z^2 + R^2)^{3/2}} \tag{2.29}$$

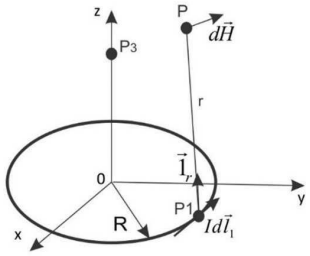

Figure 2.3: Biot-Savart law describing the relation between the magnetic field strength H and the current in an air coil

By applying superposition, this equation can be easily used to approximate the magnetic field along the axis of coil geometries as shown in Fig.2.2 (a) and (b) when these geometries are simplified as an assembly of thin of circular current filaments (cross section of wire equals to zero). From (2.29) it is clear that the magnetic field H_3 in a point on the axis is the highest inside the coil ($z = 0$) and decreases very fast at a distance outside the coil, which will be confirmed by finite element calculations.
Notice that for a predefined distance h_0 from the coil and a given current I, the magnetic field at that distance and on the z-axis may be maximized by an optimized geometry, i.e. an optimized radius $R = \sqrt{2}h_0$.

2.4.2 Alternating magnetic field inside the coil

Fig.2.4 shows the cross section of a cylindrical coil with length l, radius R and N_t number of turns. We assume a time varying electrical current $i(t)$ is flowing through the coil. The axis of the coil corresponds with the z-axis. The magnetic field H in point P_1 ($z = 0$) is oriented along the axis of the coil. If the distance from point P_1 to the end of the coil at the right is denoted by l_1, the magnetic field is expressed by:

$$H = \frac{N_t i(t)}{2l}\left[\frac{l_1}{\sqrt{l_1^2 + R^2}} + \frac{l - l_1}{\sqrt{(l - l_1)^2 + R^2}}\right] \tag{2.30}$$

In the middle of the cylindrical coil $l_1 = l - l_1 = l/2$ holds and consequently

$$H_{middle} = \frac{N_t I}{\sqrt{l^2 + D^2}} \tag{2.31}$$

At the right and left end of the coil we have $l_1 = 0$ and $l_2 = l$. Resulting in the following magnetic field

$$H_{end} = \frac{N_t I}{2\sqrt{l^2 + R^2}} \tag{2.32}$$

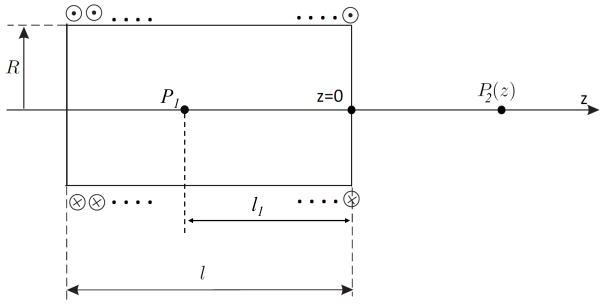

Figure 2.4: Cross section of a cylindrical/helical coil with length l, radius R and N_t number of turns

In the case the length l of the coil is large in comparison to the radius R (long cylindrical coil, $l >> R$), the magnetic field on the axis, in the middle and at the end of the air coil becomes

$$H_{middle} = \frac{N_t I}{l} \tag{2.33}$$

$$H_{end} = \frac{N_t I}{2l} = \frac{H_{middle}}{2} \tag{2.34}$$

For a coil for which $l >> R$ the magnetic field inside the coil will be, from practical point of view, uniform except at the end of the coil. For a coil infinitely long the magnetic field inside the coil becomes

$$H = \frac{N_t I}{l}$$

In that case, the magnetic field H is the same in all points of the axis of the cylindrical coil. For a short cylindrical coil, i.e. $l << R$, equation (2.23) and (2.24) become:

$$H_{middle} = H_{end} = \frac{N_t I}{2R}$$

Notice that the equations above are only valid along the axis of the coil. The space dependence of the magnetic field inside the coil is more complex. See for instance the non-homogeneous magnetic field pattern in Fig. 2.5 obtained from finite element computations.

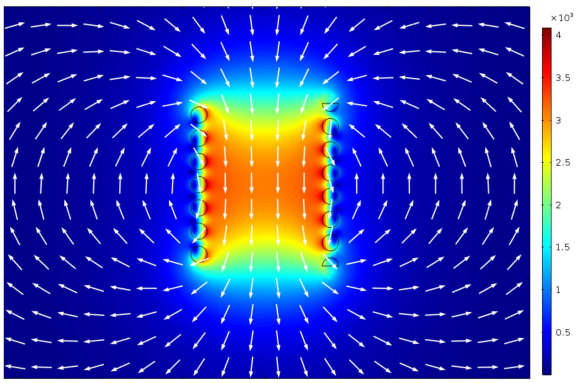

Figure 2.5: Non-homogeneous magnetic field pattern of a helical coil. The magnetic field amplitude H (A/m) (I_m=100 A) is obtained from finite element computations of 8-turns cylindrical coil. The color scale show the magnetic field strength while the white arrows are normalized and indicate the magnetic field directions.

2.4.3 Alternating magnetic field outside the coil

It will be shown in the next sections that for the application of hyperthermia on larger animals or human bodies, the magnetic field outside the coil is crucial. Considering analytical expressions for the inductance coefficient as well as for the magnetic field strength along the z-axis of the coil, we will deal with the short cylindrical coil (denoted with subscript c), the helical coil (h) and the pancake (p) type coil. These three different types are illustrated in Fig.2.6 together with their basic characteristic parameters. Starting from (2.29), for these three types of coils the magnetic field along the z-axis may be approximated by

$$H_c(h_0) = \sum_{i=1}^{N_R}\sum_{i=1}^{N_l} \frac{(R_i + (i-1)\Delta R)^2}{2((h_0 + (i-1)\Delta z)^2 + (R_i + (i-1)\Delta R)^2)^{3/2}} I$$

$$\Delta R = \frac{R_o - R_i}{N_R - 1}; \Delta z = \frac{l}{N_l - 1}; N_t = N_R.N_l \tag{2.35}$$

$$H_h(h_0) = \sum_{i=1}^{N_t} \frac{R^2}{2((h_0 + (i-1)\Delta z)^2 + R^2)^{3/2}} I; \Delta z = \frac{l}{N_t - 1} \tag{2.36}$$

and

$$H_p(h_0) = \sum_{i=1}^{N_t} \frac{(R_i + (i-1)\Delta R)^2}{2({h_0}^2 + (R_i + (i-1)\Delta R)^2)^{3/2}} I, ; \Delta R = \frac{R_o - R_i}{N_t - 1} \tag{2.37}$$

with N_t total number of turns, N_R number of turn layers in R-direction, N_l number of turn layers in z-direction and h_0 the distance between the point on the z-axis for which the field in evaluated and the nearest turn of the coil.

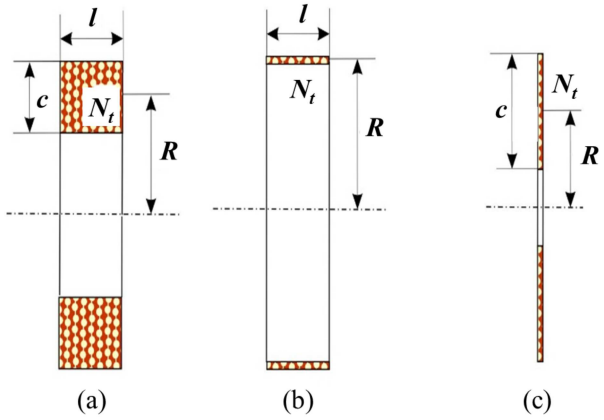

Figure 2.6: Basic characteristic parameters for the short cylindrical (a), the helical (b) and the pancake type coil (c).

The inductance of the short cylindrical coil geometry (N_t turns) in Fig.2.6.(a) may be well approximated by:

$$L_c = \frac{0,8 \times 39.37 R^2 N_t^2}{6R + 9l + 10c} 10^{-6} \tag{2.38}$$

in the case the three terms in the denominator are close to each other [83]. For the single helical coil of Fig.2.6.(b) the coil inductance becomes:

$$L_h = \frac{39.37 R^2 N_t^2}{9R + 10l} 10^{-6} \quad , l > R \tag{2.39}$$

or

$$L_h = \frac{39.37R^2N_t^2}{8R+11l}10^{-6}, R > l > 0.2R \tag{2.40}$$

For the pancake type coil of Fig.2.6.(c), one may approximate the coil inductance L_p by

$$L_p = \frac{39.37R^2N_t^2}{8R+11c}10^{-6} \tag{2.41}$$

Here, skin effects, proximity effects and capacity effects are neglected while spacing between turns is assumed to be small. These effects may alter the coil inductance to some extent. This is investigated in the next subsection.

In general, the coil inductance has the following form as can be observed when inspecting (2.38)-(2.41):

$$L = \frac{\mu_0 A_m N_t^2}{l_m} \tag{2.42}$$

with A_m a characteristic surface for the magnetic flux coupled with the coil and l_m a characteristic magnetic path length for the region with a relevant magnetic field strength. Notice that the field pattern of the air coil, as well as the inductance value is hardly changed by the presence of magnetic nanoparticles.

2.4.4 Validity of the analytical expressions and static approach: comparison with FEM

In this subsection we inspect the validity of working in a quasi-static manner, i.e. use of Biot-Savart law that are based on the quasi-static Maxwell's equations (2.15)-(2.18). For this we will first perform calculations based on quasi-static Maxwell's equations and time harmonic Maxwell's equations that include displacement currents when calculating the magnetic field (cfr. (2.12)). Secondly, we investigate whether the use of filaments as geometrical approximation of the coil are valid. We will perform magnetic field and self inductance calculations using the analytical expressions and finite element calculations. We analyze whether a quasi-static approach is allowed where calculations are performed using the finite element method for the static case as well as for frequencies up to 1 MHz. We will perform these calculations along the symmetry z-axis of the coils.

For the analysis we consider two short cylindrical coils having a small and large radius with geometrical details given in Table 2.1. The current amplitude is I_m =100 A and we assume that the conductivity of the coil is $\sigma_{\text{coil}} = 6\,10^7$ S/m.

Table 2.1: Dimensions of the small coil and the large coil

Properties	small coil	large coil
radius coil (m)	0.05	0.2
length of coil (m)	0.096	0.384
axial pitch (m)	0.012	0.048
number of turns	8	8

Finite element calculations of the magnetic fields are performed on the basis of (2.16) that includes next to the displacement current $j\omega D$ the current density J that consists of the enforced current density in the coil, denoted by J_e, and the current density σE. The magnetic vector potential A, that is related to the magnetic induction $B = \nabla \times A$, is used in the finite element calculations to find the current density

$$\underline{\mathbf{J}}_e + \sigma \underline{\mathbf{E}} = \underline{\mathbf{J}}_e - \sigma\omega \underline{\mathbf{A}}. \tag{2.43}$$

where equation (2.15) is employed to relate the electric field to the magnetic vector potential. The finite element calculations reconstruct the values of the magnetic vector potential A from which the magnetic fields can be derived. Fig.2.7 and 2.8 depict the magnetic field amplitude for the small and large coil respectively. Both static (0 Hz) and time harmonic calculations (250, 500, 750, 1000 kHz) that include displacement currents are carried out using the finite element method (that calculate the values of the magnetic vector potential). It is clear from these results that for relevant dimensions and frequency range the effect of the displacement current is negligible. It is clear from these results that below 1000 kHz the field pattern along the axis of the coil is hardly affected by the frequency. This is also observed when inspecting the inductance coefficient values L of the small and large coil in Table 2.2 for varying frequencies. Thes values were calculated by means of (2.25) and (2.26) for the static case and time harmonic case, respectively. Similar observations were obtained for the pancake and butterfly type coils.

It is clear that below 1000 kHz, the field pattern along the axis of the coil is hardly affected by the frequency, which is also observed for the inductance coefficient L of the coil, see Table 2.2. Similar observations were obtained for the pancake and the butterfly type coils.

The validity of the analytical expressions can be checked by comparing the analytical magnetic field and self inductance calculations with finite element calculations. This is carried out for the small cylindrical coil with geometrical properties provided in Table 2.1 and analytical expression (2.35). We also perform calculations for a helical coil with analytical expression (2.36) and pancake coil with analytical expression (2.37). The geometrical properties of the helical coil are radius

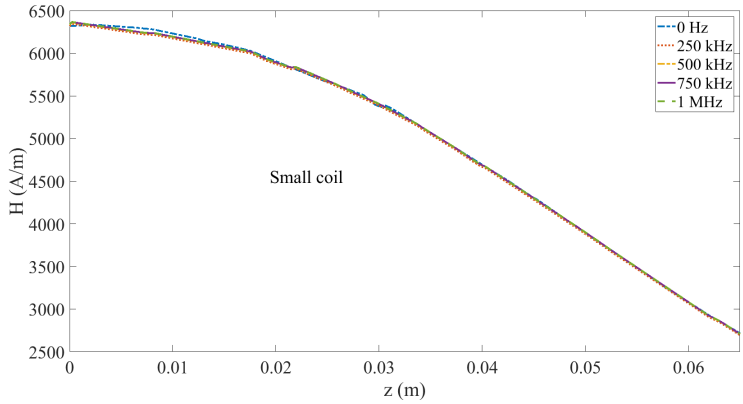

Figure 2.7: Magnetic field along the z-axis of the small coil in static case (0 Hz) and in the time harmonic case (250, 500, 750 and 1000 kHz). The calculations are all performed for an excitation current with amplitude I_m=100A.

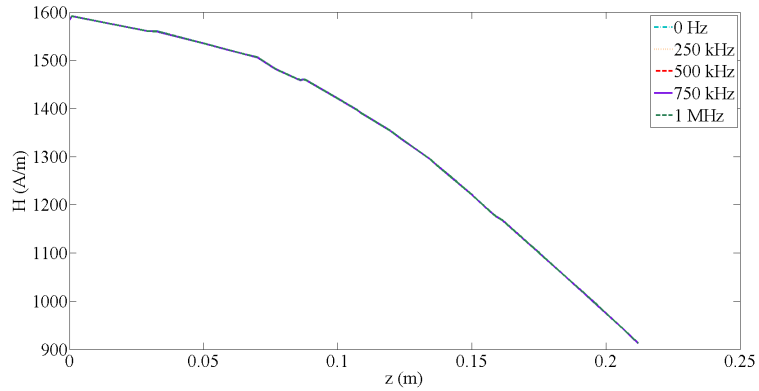

Figure 2.8: Magnetic field along the z-axis of the large coil in the static case (0 Hz) and in the time harmonic case (250, 500, 750 and 1000 kHz). The calculations are all performed for an excitation current with amplitude I_m=100A.

$R = 0.05$ m ; length $l = 0.096$ m, $N_t = 8$ and for the pancake coil: radius $R = 0.05$ m, $c = 0.096$ m, and $N_t = 8$ turns. Fig.2.9 compares the magnetic field strength H along the axis (z-axis) of the considerd helical and pancake coil. Only a limited discrepancy between the analytical models and the FEM model results can be observed. This discrepancy can be attributed to the assumed ideal stacking of the turns in the analytical models while a more realistic positioning of these turns is considered for the FEM models.

Based on the presented results we validate the use of the quasi-static approxima-

Table 2.2: Magnetic energy stored and corresponding inductance coefficient as a function of frequency for a current amplitude I_m=100 A; For the static computation w_m=$0.5LI_m^2$ while for the computation in the frequency domain w'_m=$0.25LI_m^2$, according to (2.25) and (2.26). Calculations are performed based on the geometrical properties mentioned in Table 2.1

freq [kHz]	w_m [J]	w'_m [J]	L [μ H]
Small cylindrical coil			
0 (static)	0.025101	-	5.0202
250	-	0.012463	4.9852
500	-	0.012539	5.0156
750	-	0.012518	5.0072
1000	-	0.012546	5.0184
Large cylindrical coil			
0 (static)	0.1004	-	20.0800
250	-	0.050183	20.0732
500	-	0.050200	20.0800
750	-	0.050199	20.0796
1000	-	0.050201	20.0804

tion and the analytical expressions with respect to the magnetic properties of the hyperthermia excitation coil. Based on the above we further analyze the usage and the design of the inductor-capacitor ciruit for hyperthermia.

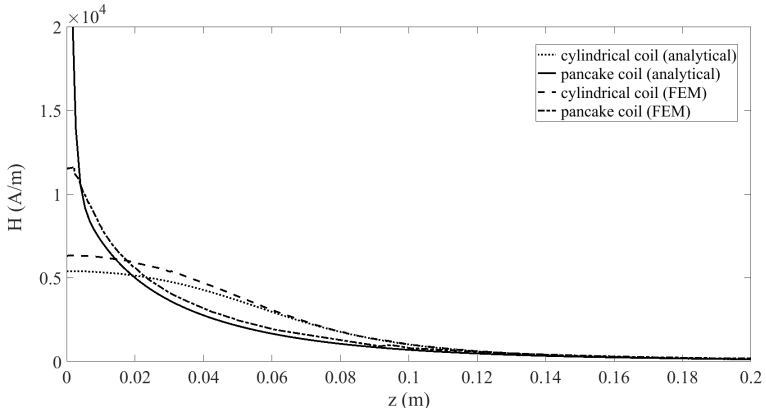

Figure 2.9: Comparison of the analytical expressions and FEM for the small cylindrical coil and a pancake type coil for a current of 100 A. Notice that the helical and the pancake coil are positioned in such a way that z=0 m corresponds with the middle of the coils, i.e. z=0 m and z=0.048 m correspond with respectively the right end of the pancake and helical coil.

2.5 Exploitation of magnetic field inside solenoid coils: limitations for large animals and human bodies

Cylindrical coils are the traditional inductor geometry used for performing hyperthermia on individual cell cultures and small animals. This is due to the fact that these coils generate a uniform field in a limited volume within the coil. Samples that are placed within the coil are exposed to an almost homogeneous magnetic field, i.e. the 3D magnetic field amplitude is almost constant in the sample or small animal that needs to be subjected to hyperthermia. See for instance the magnetic field distribution within the coil in Fig. 2.5. However, rescaling these cylindrical coils in order to treat deep-seated tumors in larger animals or human bodies is not evident. Scaling laws on how the geometrical dimensions of the excitation coil - defined by its number of turns N_t or its coil dimensions (diameter of coil) - affect the relevant quantities that characterize the magnetic nanoparticle heating equipment need to be drawn. This can provide insights on how we can scale the hyperthermia equipment and up to what limit this is possible specifically for bone metastases hyperthermia. The scaling laws are such that the magnetic field amplitude H and the resonance frequency f_r remain the same when scaling up. Two cases are here specifically considered: the number of turns N_t are multiple with the scaling factor k (Case 1); the number of turns N_t are kept constant but the coil dimensions are multiplied with the scaling factor k (Case 2). Since we are interested in the upscaling of the excitation coil, $k > 1$. Table 2.3 shows the scaling laws for the two considered cases. The scale dependence of L can be derived from the general formulation of coil inductance (2.42) that affects the scaling of C to have a constant resonance frequency (2.4). The current I flowing through the connected coil with capacitor bank scales according to (2.30) for a given constant magnetic field amplitude. The voltage over the coil (V_L) and over the capacitor bank (V_C) are given by:

$$\underline{V}_C = \frac{-j\underline{I}_C}{\omega C} \tag{2.44}$$

$$\underline{V}_L = j\omega L\underline{I}_L \tag{2.45}$$

resulting in the scale dependence of V_C and V_L as mentioned in Table 2.3. Equation (2.6) results in the proper scale dependence of N_s/N_p. Taking into account the voltage and current limits of the capacitors in Table 2.4 it is clear that for Case 1, the number N_s of capacitors in series should be adapted in order to take into account the voltage limit for each capacitor and keeping the number of parallel branches N_p constant as the current is not influenced by the rescaling, while for Case 2, the number of parallel branches N_p in the capacitor bank becomes proportional to the geometrical scaling factor k as I_C becomes proportional with k.

Table 2.3: Scaling laws of quantities in magnetic nanoparticle heating equipment when all dimensions of the excitation coil as well as the number of turns N_t are multiplied with k, ($k > 1$) (case 1) and when only the coil dimensions are multiplied with k while the number of turns N_t remain constant (case 2)

-	L	C	I	V_C	V_L	N_s/N_p
Case 1	k^3	k^{-3}	k^0	k^3	k^3	k^3
Case 2	k^1	k^{-1}	k	k^2	k^2	k^1

Rescaling an inductor geometry used for individual cell cultures or small animals to larger coils and having the same alternating magnetic field at the same resonance frequency gives rise to unrealistic high voltages over the coil and over the capacitor bank, as well as high voltages between neighboring coil turns and capacitor (high values for N_p and N_s...).
Let us consider the following exemplary inductor: an 8-turns helical coil of Fig.2.2 of a radius $R = 0.05$ m, a length $l = 0.096$ m and a diameter of the wire $c = 0.01$ m. According to (2.39), the self inductance of this specific coil becomes: 4.0210^{-6} H. For a frequency of 200 kHz and a current of 100 A, the voltage of the coil and the capacitor bank V_C and V_L becomes: 505 V. Using the previous coil in large animals and human experiments means that the radius R of the coil should be increased from $R = 0.05$ m to $R = 1$ m (which corresponds with a scaling factor of $k = 20$), results in a voltage of the coil and the capacitor bank of 4.041 kV (Case 1) and 202 kV (Case 2).

Table 2.4: Voltages and current limits of the capacitors

Capacitor C (μF)	V_{max} (V)	$I_{\text{max}}(A)$
1.5	500	750
1	700	750
0.5	700	600
0.25	1000	450

2.6 Exploitation of magnetic field outside coils

In this section we exploit the presence of the magnetic fields outside the excitation coils, contrary to scaling up existing helical coils that are currently used for magnetic hyperthermia of small animals or of culture cells. This is schematically presented in Fig.2.10. This poses the question on what coil topology, cfr. Fig. 2.2 - cylindrical, helical, pancake, butterfly coil - is best suited to exploit the presence of the magnetic fields outside the coils for performing magnetic hyperthermia. A

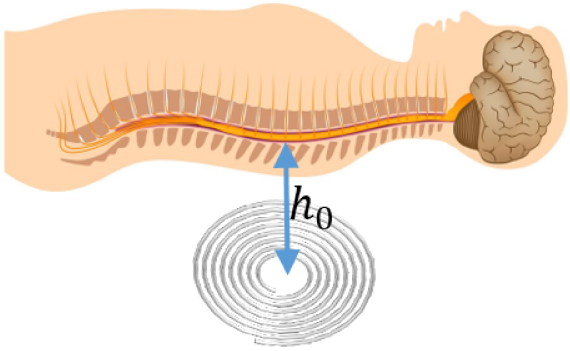

Figure 2.10: Schematic representation of exploiting magnetic fields outside excitation coils. At distance h_0 from the excitation coil a magnetic field with amplitude H is generated. By optimizing the geometrical properties of the excitation coil, the magnetic field at distance from the excitation coil is maximized.

subsequent question is whether the generated magnetic field amplitudes H are sufficient and the required resonance frequency f_r is satisfied for achieving magnetic hyperthermia at a certain distance h_0 from the coil for a limited predefined maximum current I_m flowing in the coil. To answer these questions we will explore for the different coil topologies what the effect is of their geometrical properties on the magnetic field amplitudes at a distance from the coil as well as on the associated inductance values L (that also affects f_r). Based on these explorations we will perform an optimization of the coils by maximizing the magnetic field amplitude at distance h_0 and by subsequently inspecting the corresponding coils' geometrical properties, each time for fixed excitation current I_m.

To perform our study and optimization we make use of analytical and 3D finite element method (FEM) based simulations of the coil topologies. On the symmetry (z) axis of cylindrical, helical and pancake coils, the magnetic field is maximal. Therefore, the analytical expressions for the generated magnetic fields presented in (2.35) for cylindrical coils, (2.36) for helical coils, and (2.37) for pancake coils can be used. The inductance values can, starting from the geometrical parameters, be calculated via equations (2.38)-(2.41) with the general expression (2.42). Their corresponding basic geometrical parameters are illustrated in Fig.2.6 that constitute the design space, i.e. for the short cylindrical coil topology that design space is characterized by R, c, l, N_t; helical coil topology that is R, l, N_t; pancake coil topology that is R, c, N_t. For the butterfly coil, the design space is similar to the pancake coil topology as this topology consists of two pancakes that are in

series connected. As the butterfly coil topology has no symmetry axis, FEM based simulations will be performed to inspect the generated magnetic field amplitudes and the resonance frequency. The purpose of this section is to find the geometrical parameters that maximize the magnetic field amplitude at a certain distance h_0 from the coil and know its effect on the inductance as this influences the resonance frequency.
A typical distance that is required is in the range of $h_0 = 10 - 15$ cm. The calculations are performed for an arbitrary choosen unit current of $I_m = 1$ A. The magnetic field values are linear with the excitation current (see also (2.35)- (2.37)) and can thus be easily extended for different excitation currents I_m.

2.6.1 Analytical optimization short cylindrical, helical and pancake coils

In this section, analytical expressions are used to optimize the short cylindrical, helical and pancake coil topologies. A parameter sweep in the design space is first performed to explore the effect of the various geometrical parameters on the magnetic field amplitude. The following range of geometrical parameters are considered: $0.01\text{m} \leq R \leq 0.40\text{m}$, $0.01\text{m} \leq l \leq 0.40\text{m}$, $0.01\text{m} \leq c \leq 0.40\text{m}$ and $2 \leq N_t \leq 25$. Each combination of these geometrical parameters is considered. For each of these geometrical parameter values a magnetic field and inductance value can be calculated analytically. Figure 2.11 shows the magnetic field and inductance values that correspond to various design points within the above specified range of a pancake coil topology (with geometrical design parameters R, c, N_t, see also Fig. 2.6(c)). The calculations are based on (2.37) with magnetic field along the symmetry (z) axis of the pancake coil at a distance $h_0 = 10$ cm from the excitation coil that is excited with maximal excitation current $I_m = 1$ A. This H-L plot shows the important effect that the geometrical parameters can have on the magnetic field and inductance values. Figure 2.11 also shows that for increasing inductance values, the maximal magnetic field amplitude values correspondingly increase. Since we are only interested in the designs that correspond to maximal magnetic field, we only keep record of the points that give rise to maximal magnetic field H_{max}. The optimized pancake coil topology is shown in Fig.2.12 and comparison is made with the optimized cylindrical and helical coil topologies. These curves were generated for coils at a distance of $h_0 = 10$ cm and excitation current $I_m = 1$ A via a parameter sweep. This figure clearly shows the effect of the chosen coil topology on the maximal magnetic field. From Fig.2.12 it can be deduced that the pancake coil topology gives rise to the maximal magnetic field values at a distance of $h_0 = 10$ cm for all inductance values.
We also inspected whether for an increasing distance of $h_0 = 15$ cm this conclusion holds. Figure 2.13 shows for this distance (and same excitation current as in

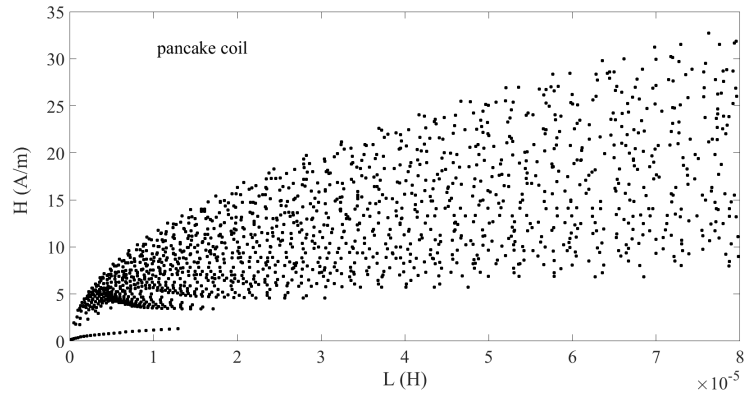

Figure 2.11: Magnetic field (H) and inductance (L) values at a distance of $h_0 = 10$ cm from pancake coil excited with current $I_m = 1$ A. The cloud of points are generated via a parameter sweep on the geometrical parameters R, c, N_t.

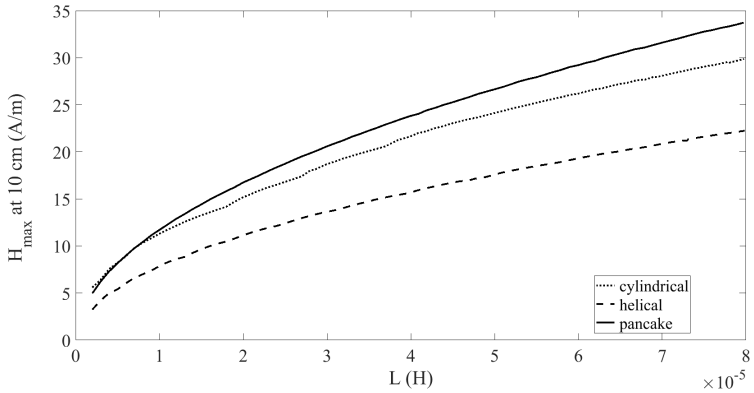

Figure 2.12: Maximal magnetic field (H_{max}) and corresponding inductance (L) values at a distance of $h_0 = 10$ cm from optimal pancake coil, helical and pancake coils; each excited with current $I_m = 1$ A.

Fig.2.12) the maximal magnetic field values for the optimized pancake, helical and cylindrical coils. As was readily observed from Fig. 2.9, the maximal magnetic fields shown in Fig. 2.13 are also lowered compared to the ones of Fig. 2.12. From this figure we conclude that – based on the analytical expressions - the pancake is the preferred coil topology to generate a maximal magnetic field outside the excitation coil.

The geometrical properties (R, c, N_t) of the pancake coil topology that give rise to the maximal magnetic field for varying inductance values at distance $h_0 = 10$ cm and $h_0 = 15$ cm are depicted in Fig. 2.14 and 2.15 respectively. For increasing

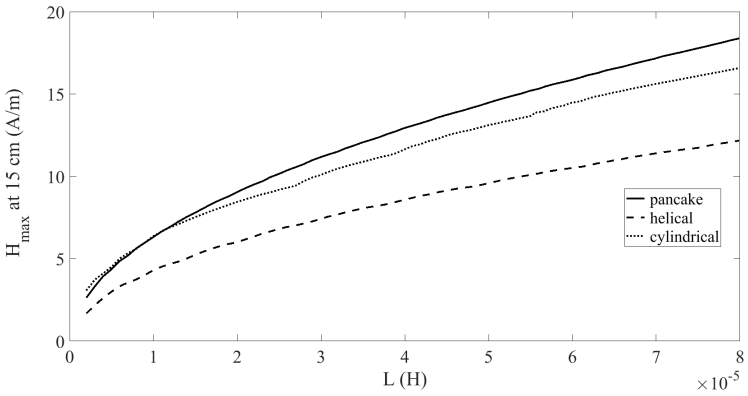

Figure 2.13: Maximal magnetic field (H_{max}) and corresponding inductance (L) values at a distance of $h_0 = 15$ cm from optimal pancake coil, helical and pancake coils; each excited with current $I_m = 1$ A.

inductance values we have an increase of the number of turns N_t of the pancake coil. The important effect of N_t on L can also be observed from (2.42), but also R and c affect the inductance value. The red line in Fig. 2.14 and 2.15 shows that when N_t increases with 1 turn, this results in a corresponding decrease of R and c; but that after the increase of the number of turns, R and c increase so to maximize the magnetic field. From Fig. 2.14 and 2.15 it can observed that depending on what distance we wish to achieve a maximal magnetic field, this results in a different optimized coil geometry (i.e. different R, c and N_t values).

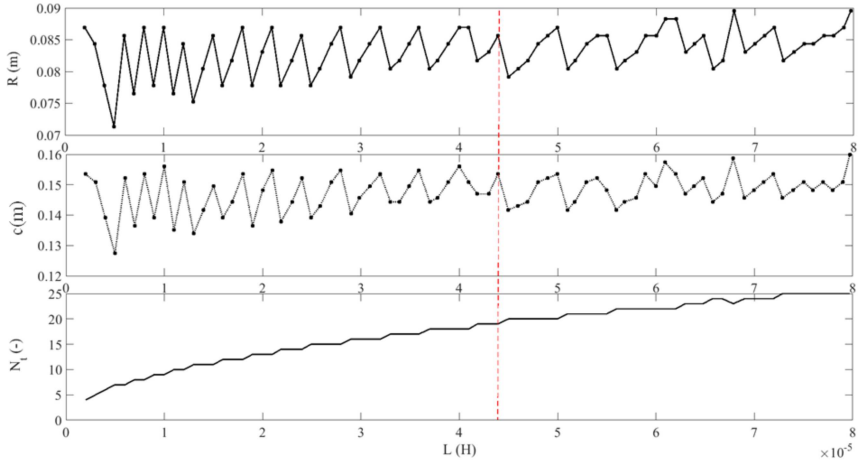

Figure 2.14: Geometrical parameter values R, c, N_t of the pancake coil topology that maximize the magnetic field values at a distance of $h_0 = 10$ cm from the coil, for varying inductance values L.

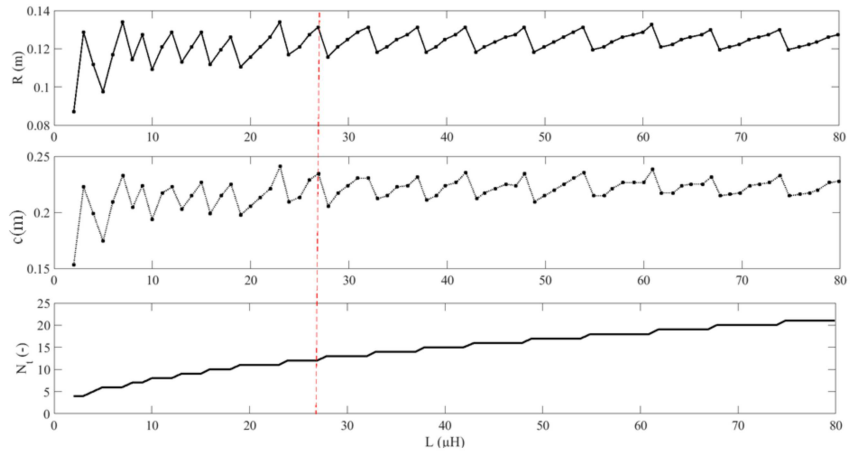

Figure 2.15: Geometrical parameter values R, c, N_t of the pancake coil topology that maximize the magnetic field values at a distance of $h_0 = 15$ cm from the coil, for varying inductance values L.

2.6.2 FEM optimization of butterfly and pancake coils

In this section the excitation coil is optimized on the basis of FEM simulations. As in previous section the aim is to maximize the magnetic field amplitude H at a height h_0 above the excitation coil for a given excitation current I_m in the coil. As in Section 2.6.1, the maximal magnetic field is put in relation with the inductance L. From the results of that section it is clear that the pancake coil is a favorable topology compared to the helical and short cylindrical coil topologies. We limit the FEM optimization to the pancake coil and the butterfly coil topology. The finite element simulations are performed in 3D so to assess the spatial configuration of the magnetic field since for the butterfly coil topology there is no symmetry axis and calculations are required in 3D. The coil configurations implemented in FEM are realistic, i.e. the wire diameter has a finite dimension (no infinitesimally small current elements as in the analytical expressions). Around the coil a large sphere is considered wherein the computations are performed. The FEM simulations revolve on finding the magnetic vector potential values $\mathbf{A}$ in the domain where a current density $|\underline{\mathbf{J}}_e| = I_m/S$ is enforced in the coil where S is the cross-section area of the wire of the coil. On the boundary of the computational domain we enforce magnetic insulation $\mathbf{n} \times \mathbf{A} = 0$ with $\mathbf{n}$ being the normal vector pointing outwards the domain. This boundary condition is commonly choosen in quasi-static magnetic field computations and makes it possible to have unique magnetic vector potential values. Volumetric meshing is performed as depicted in Fig. 2.16 and 2.17. The center of the domain ($x = 0$,$y = 0$,$z = 0$) corresponds with the middle of the pancake and butterfly coil. In the FEM calculations we have the following material properties for air and copper, defining the constitutive equations (2.12), (2.13) and (2.14): the electrical conductivity of the coil (copper) is $\sigma = 5.997 \cdot 10^7$ S/m and for air $\sigma = 0$ S/m; the relative permeability and the relative permittivity of both the coil and air are $\mu_r = 1$ and $\epsilon_r = 1$, respectively.
Figure 2.18 shows the spatial distribution of the magnetic field intensity H in a plane parallel to the pancake coil at a distance of $h_0 = 10$ cm. As can be observed, maximal magnetic field is attained on the symmetry (z) axis of the pancake, as was presumed in section 2.6.1, and that decays radially at a distance from that symmetry axis. Figure 2.19 shows how the magnetic field originating from a pancake coil is distributed in the (x,z) plane for $y = 0$. This figure clearly shows the spatial decay of the magnetic field strength outside the pancake coil as well as the spatial dependence of the direction of the magnetic field. In and near the symmetry axis we have mainly a direction normal to the plane of the pancake coil whereas this shifts towards a tangential direction near the outer radius of the pancake coil. From this figure it is clear that maximal magnetic field strength is realized near the symmetry axis, as was analyzed in Section 2.6.1.
FEM calculations presented in Fig. 2.18 and 2.19 for the pancake coil were also performed for the butterfly coil, depicted in Fig. 2.20 and 2.21 respectively. From

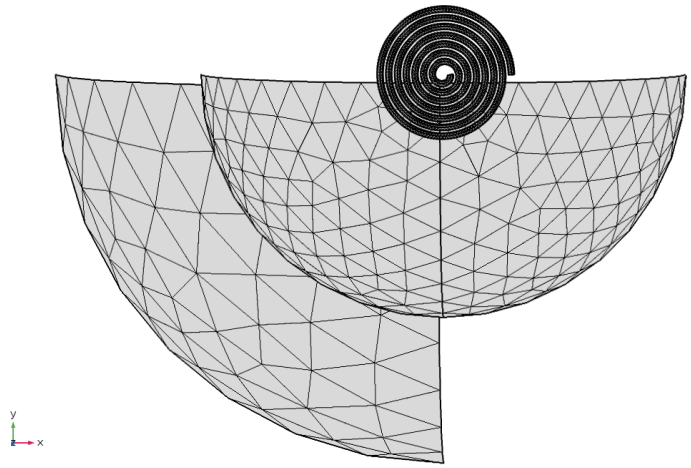

Figure 2.16: Volumetric meshing of the pancake coil in 3D for the finite element based computations of the magnetic field pattern. The z axis corresponds with the symmetry axis of the pancake coil.

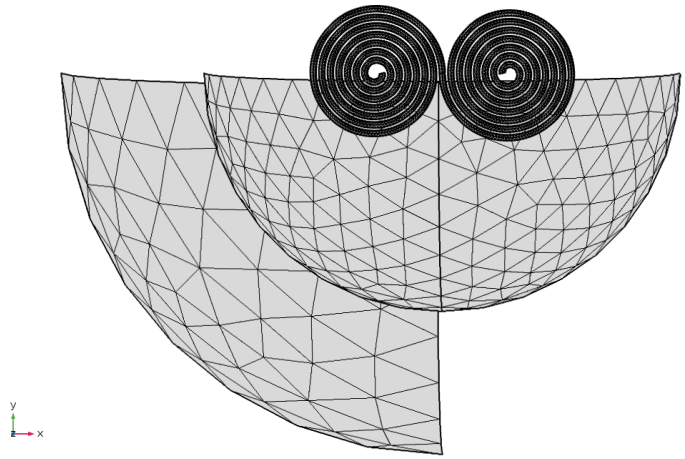

Figure 2.17: Volumetric meshing of the pancake coil in 3D for the finite element based computations of the magnetic field pattern. The z axis corresponds with the normal direction in the middle of the butterfly coil, i.e. where the two pancake coils (that give rise to the buttery coil) interconnect.

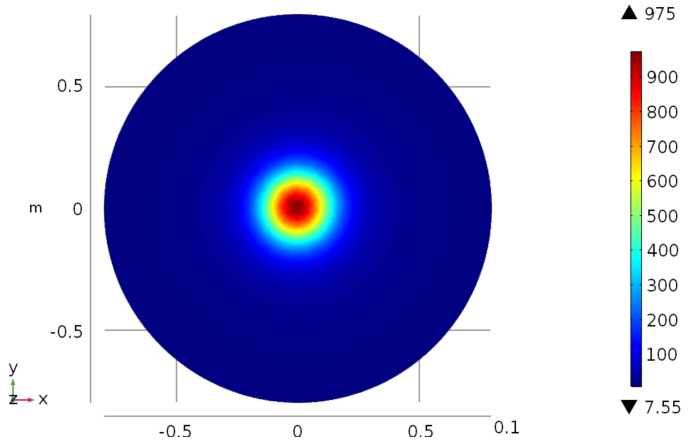

Figure 2.18: Magnetic field intensity in a plane parallel to the pancake coil at a distance of $h_0 = 10$ cm. The color bar shows the magnetic field strength (A/m) when enforcing the pancake coil with a current of $I_m = 100$ A.

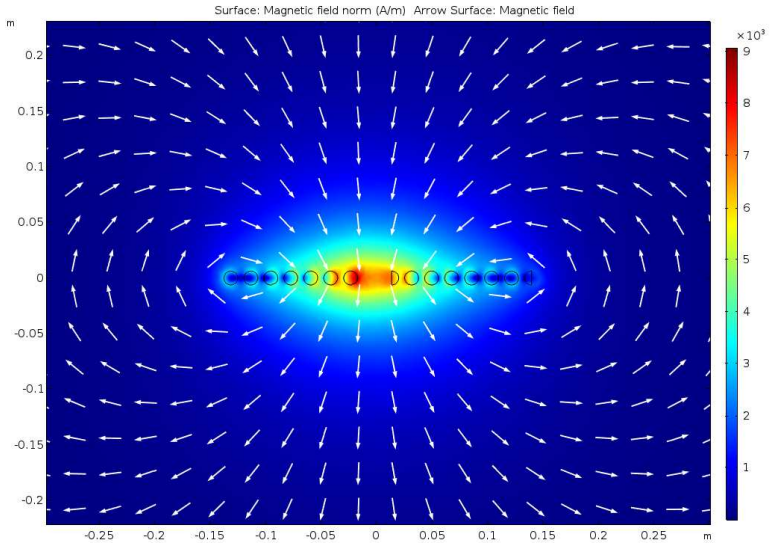

Figure 2.19: Magnetic field intensity in the (x,z) plane (with $y = 0$) of a pancake coil. The color bar shows the magnetic field strength (A/m) when enforcing the pancake coil with a current of $I_m = 100$ A. The directions of the magnetic field are depicted by the arrows.

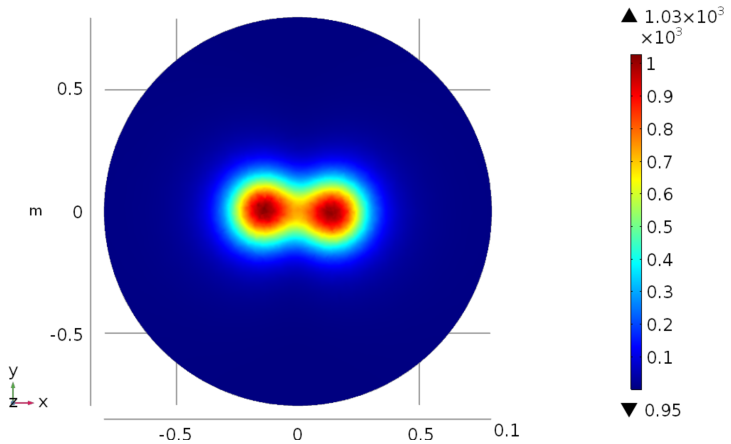

Figure 2.20: Magnetic field intensity in a plane parallel to the butterfly coil at a distance of $h_0 = 10$ cm. The color bar shows the magnetic field strength (A/m) when enforcing the butterfly coil with a current of $I_m = 100$ A.

Fig. 2.20 it is clear that the magnetic field strength cannot be found in the middle of the butterfly coil and that when comparing the spatial distribution with Fig. 2.19 that the magnetic field has a larger spatial spread since a butterfly coil can be regarded as two series connected pancake coils. This can also be observed in Fig.2.21 where the direction of the magnetic field is different than in case of the pancake coil (Fig. 2.19). For the butterfly coil we have in the z axis (with $x = 0$ and $y = 0$) mainly a tangential field direction whereas near the center of the two pancake coils the direction becomes again normal to the plane of the butterfly coil. Direct quantitative comparison between the butterfly and pancake coil is made in Fig. 2.22 and 2.23. From Fig. 2.22 it can be observed that the magnetic field increases when coming near to the center of one of the two pancake coils that constitute the butterfly coil and that the magnetic field strength can be similar and even larger than the pancake coil's magnetic field strength in its center axis. This is due to the fact that the butterfly coil is a superposition of the magnetic field of two pancake coils. Due to the radial decay of the magnetic field in the pancake coil the difference in magnitude is relatively small. Figure 2.23 depicts the decay of the magnetic field at a certain distance normal to the plane of the pancake and butterfly coil. We can observe that the decay of the magnetic field originating from the pancake and butterfly coil follows a similar trend and that the magnetic field strength from the pancake coil along its symmetry (z-axis going through (0,0) cm) and butterfly coil along the normal axis going through the coordinate (12, 0) cm are similar.

A geometrical optimization of the pancake and butterfly coil topology is performed on the basis of FEM computations. The optimization goal is, as in previous sub-

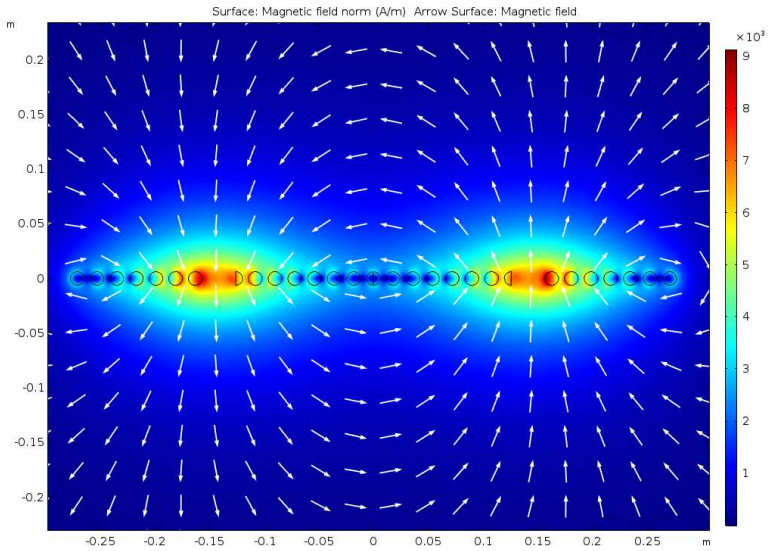

Figure 2.21: Magnetic field intensity in the (x,z) plane (with $y = 0$) of a butterfly coil. The color bar shows the magnetic field strength (A/m) when enforcing the pancake coil with a current of $I_m = 100$ A. The directions of the magnetic field are depicted by the arrows.

section, to maximize the magnetic field at a height h_0 above the coil for a given excitation current in the coils. The same steps are followed as in the optimization based on analytical expressions. We limit ourselves to the pancake coil as this came out as having superior magnetic field strengths at a certain distance from the coil; and compare this with the butterfly coil. A parameter sweep of the geometrical properties of the pancake and butterfly coil topology is shown in Fig.2.24. The pancake coil is characterized by the geometrical parameters R, c, N_t (see Fig. 2.6 (c)) and are also used for characterizing the butterfly coil. From Fig. 2.24 we can conclude that for a given inductance value L and for a certain excitation current I_m, the pancake coil generates superior magnetic field strengths at a predefined distance from the plane of the coil.Indeed, the butterfly coil can be seen as two in series connected pancake coils resulting in a higher inductance value. For the geometrical optimization of the pancake coil itself, we refer to Section 2.6.1 and more specifically to figures 2.14 and 2.15.

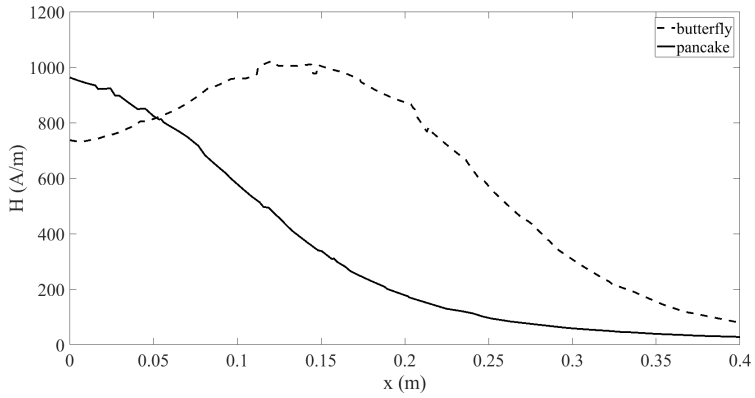

Figure 2.22: Comparison of magnetic field strength (norm) in case of butterfly and pancake coil along the x-line y=0 m, z=0.1 m. (Use of right handed coordinate system where pancake/butterfly coil plane defines xy-plane and origin of the coordinate system is in the center of pancake coil and in the node (middle of the two centers) of butterfly coil)

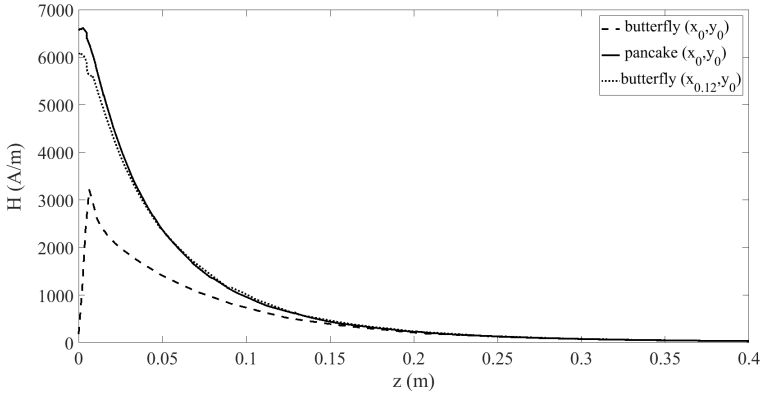

Figure 2.23: Comparison of magnetic field strength (norm) in case of butterfly (along the z-lines x=0 m, y=0 m and x=0.12 m, y=0 m) and pancake coil (along the line x=y=0 m).

2.7 Shielding effect and induced eddy currents in the human body

In previous sections we analyzed the magnetic field originating from the excitation coil in the surrounding air. This was each time without considering the presence of the human body. Since the human body is electrically conducting, the alternating magnetic field induces eddy currents within the human body that on its turn will give rise to an alternating magnetic field that is counteracting the external ap-

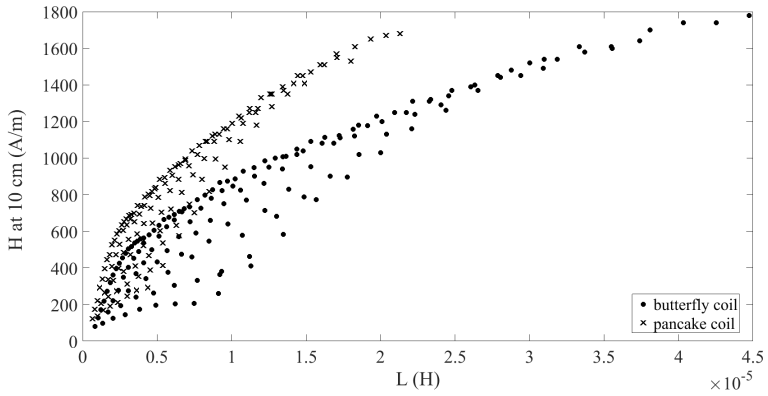

Figure 2.24: Cloud of design points for pancake coil and butterfly coil on the basis of FEM computations, for I_m=100A, at h_0=10 cm,

plied magnetic field. This Faraday effect is mathematically represented by (2.7) where an alternating magnetic field ($\frac{\partial \mathbf{B}}{\partial t}$) gives rise to electrical field $\mathbf{E}$ and associated current density $\mathbf{J}$. This effect is commonly refered to as shielding effect of conducting material when subject to an alternating magnetic field. In this Section we analyze to which extend the magnetic field at the position of the spinal cord, at height h_0 above the excitation coil, is attenuated due to the electrical currents induced in the human body by the magnetic field generated by the excitation coil. We furthermore quantify the heat that is generated by the eddy currents as they result in associated eddy current loss. Notice that the excitation may have a dominant component orthogonal to the surface of the human body (see e.g. the field pattern near the inner turn for the pancake type coil in Fig.2.19) or may have a dominant component tangential to the surface of the human body (see e.g. the field pattern at the center of the butterfly coil in Fig. 2.21). Both cases will be analysed by a simple analytical model that will provide insights on the attenuation of the magnetic field in the human body as well as the heating within the body due to eddy current losses.

In this section, eddy currents are analyzed as the electrical currents induced within tissues by the changing magnetic field due to Faraday's law of induction (2.7). These eddy currents flow in closed loops within tissue in planes perpendicular to the magnetic field. The magnitude of the current in a given loop is first of all proportional to the strength of the local magnetic field, the area of the loop, the rate of change of the magnetic flux coupled with the loop and to the conductivity and permittivity of the tissues. The eddy currents themselves create a magnetic field that opposes the magnetic field that created it. As a consequence, time varying magnetic fields do not penetrate completely into the interior of tissues. Here, we

investigate to which extend the electrical currents induced in tissue reduce the magnetic field at the position of the magnetic nanoparticles. This reduction definitely effects the heat production of the magnetic particles. On the other hand the induced electrical currents themselves produces heat in the tissue. Simple analytical models are introduces based on magnetic fields tangential respectively orthogonal to the surface of the skin. The permeability is assumed to be equal to the one of air.

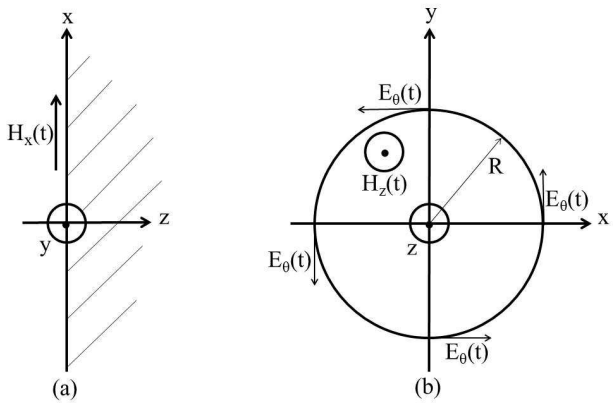

Figure 2.25: Half space linear material subject to a tangential (a) and normal (b) incident magnetic field.

We assume the human body as being a half space with material properties being electric - characterized by its permittivity ε and conductivity σ - and magnetic - characterized by permeability μ. These material properties are linear and we furthermore assume here that the values are constant (i.e. homogeneous) within the half space. The location of this human tissue in a coordinate system is shown in Fig.2.25(a). A sinusoidal electromagnetic field $\mathbf{H} = H_x(t)\mathbf{1}_x$ with $H_x = H_0 \cos(\omega t)$ with $\omega = 2\pi f$ being the angular frequency (and frequency f); acts upon the surface $z = 0$ parallel to the x-axis. This field is here tangential to the surface of the human body. This corresponds for instance to the magnetic field orientation that arises in the middle (z-axis) of the butterfly coil (as depicted in Fig. 2.21). For such a simplified case, the spatial derivatives of the electric and magnetic field quantities to x and y equal 0 and the equations (2.15)-(2.16) and (2.12)-(2.14) result in

$$-\frac{d\underline{E}}{dz} = -j\omega\mu_0\underline{H} \tag{2.46}$$

$$\frac{d\underline{H}}{dz} = (\sigma + j\omega\epsilon)\underline{E} \tag{2.47}$$

and consequently

$$\frac{d^2\underline{H}}{dz^2} = k^2\underline{H} \tag{2.48}$$

$$\frac{d^2\underline{E}}{dz^2} = k^2\underline{E} \tag{2.49}$$

with the so-called propagation constant k defined as:

$$k^2 = -\omega^2\mu_0\epsilon + j\omega\mu_0\sigma \tag{2.50}$$

The expression for the magnetic field strength that satisfies (2.48) then becomes

$$\underline{H}_x = H_1 e^{kz} + H_2 e^{-kz} \tag{2.51}$$

with

$$k = \frac{1}{a} + j\frac{1}{b} = \left(\sqrt{\frac{\sigma\mu_0\omega}{2}}\sqrt{\sqrt{1+\frac{\omega^2\epsilon^2}{\sigma^2}} - \frac{\omega\epsilon}{\sigma}}\right) + j\left(\sqrt{\frac{\sigma\mu_0\omega}{2}}\sqrt{\sqrt{1+\frac{\omega^2\epsilon^2}{\sigma^2}} + \frac{\omega\epsilon}{\sigma}}\right) \tag{2.52}$$

resulting in

$$\underline{H}_x = H_0 e^{-kz}$$

$$\underline{J}_y = (\sigma + j\omega\epsilon)\underline{E}_y$$

$$\underline{E}_y = \frac{-k}{\sigma + j\omega\epsilon} H_0 e^{-kz} \tag{2.53}$$

as $\underline{H}_x(z=0) = H_0$ and $\underline{H}_x(z \to +\infty) = 0$. In the time domain, the magnetic field H_x becomes

$$H_x(z,t) = H_0 e^{-\frac{z}{a}} \cos(\omega t - \frac{z}{b}) \tag{2.54}$$

with a being the skin depth, defining the position in the material where the amplitude of field strength is reduced with a factor e^{-1} compared to the field strength H_0 at the surface.
In Tables 2.5-2.10 the conductivity and permittivity of two different tissues are given as a function of frequency. As a consequence also the skin depth a, defined by (2.52), is frequency dependent through both electrical properties. It is observed

that for skin tissue we hardly have a reduction of the magnetic field, while 0.02 m inside muscle tissue, a reduction of the magnetic field may be observed up to 2.5 percent for a frequency of 1000 kHz. For the electric field intensity, we obtain the expression

$$\underline{E}_y = \frac{-k}{\sigma + j\omega\epsilon} H_0 e^{-kz}; \tag{2.55}$$

resulting in a local eddy current loss due to a tangential magnetic field (denoted by P_t) that is expressed in W/m^3 and given by

$$P_t = \frac{1}{2}\sigma \underline{E}_y . \underline{E}_y^* = \frac{\sigma^2 \mu\omega}{2\sqrt{\sigma^2 + \omega^2\epsilon^2}} H_0^2 e^{-\frac{2z}{a}} \tag{2.56}$$

A maximum value for the eddy current loss is obtain at the surface ($z = 0$):

$$P_t = \frac{\sigma^2 \mu\omega}{2\sqrt{\sigma^2 + \omega^2\epsilon^2}} H_0^2 = L_{tiss,t} H_0^2 \tag{2.57}$$

The tissue and frequency dependent parameter $L_{tiss,t}$ are given in Table 2.5-2.10.

Table 2.5: Electromagnetic parameters for skin tissue, the corresponding skin depth a as a function of frequency and the corresponding reduction of the magnetic field at 10 cm in the tissue.

f [kHz]	σ_{skin} [S/m]	$\epsilon_{r_{skin}}$ [-]	a [m]	$L_{tiss,t}(skin)$	$L_{tiss,n}(skin)$
100	0.000451	1120	394.205	1.286E-05	8.785E-08
250	0.00146	1100	120.737	0.000137	1.777E-06
500	0.00436	1060	39.751	0.001259	2.123E-05
750	0.00839	1030	20.403	0.004762	9.193E-05
1000	0.0132	991	12.750	0.012139	0.000257

Table 2.6: Electromagnetic parameters for fat tissue, the corresponding skin depth a as a function of frequency and the corresponding reduction of the magnetic field at 10 cm in the tissue.

f [kHz]	σ_{fat} [S/m]	$\epsilon_{r_{fat}}$ [-]	a [m]	$L_{tiss,t}(fat)$	$L_{tiss,n}(fat)$
100	0.0434	101	7.6895205	0.0171312	8,45411E-06
250	0.0436	67.8	4.873215	0.0430189	5.30817E-05
500	0.0438	56.8	3.4629158	0.0863965	0.0002133
750	0.0439	52.9	2.8443493	0.1298112	0.00048102
1000	0.0441	50.8	2.4746827	0.1737335	0.00085905

Table 2.7: Electromagnetic parameters for muscle tissue, the corresponding skin depth a as a function of frequency and the corresponding reduction of the magnetic field at 10 cm in the tissue.

f [kHz]	σ_{musc} [S/m]	$\epsilon_{r_{musc}}$ [-]	a [m]	$L_{tiss,t}(musc)$	$L_{tiss,n}(musc)$
100	0.362	8090	2.814532	0.1418127	7.05159E-05
250	0.396	5760	1.768678	0.383061152	0.0004823
500	0.446	3650	1.193147	0.8583781	0.0021719
750	0.48	2500	0.934342	0.307651	0.0052595
1000	0.503	1840	0.785125	1.9458030	0.0097982

Table 2.8: Electromagnetic parameters for red marrow bone, the corresponding skin depth a as a function of frequency and the corresponding reduction of the magnetic field at 10 cm in the tissue.

f [kHz]	σ_{red_m} [S/m]	$\epsilon_{r_{red_m}}$ [-]	a [m]	$L_{tiss,t}(red_m)$	$L_{tiss,n}(red_m)$
100	0.103	173	4.982454	0.040659	2.00639E-05
250	0.103	127	3.1635	0.101636	0.0001254
500	0.104	110	2.23985	0.205187	0.000506
750	0.104	103	1.839738	0.307651	0.0011395
1000	0.104	99	1.602545	0.409977	0.0020259

Table 2.9: Electromagnetic parameters for yellow marrow bone, the corresponding skin depth a as a function of frequency and the corresponding reduction of the magnetic field at 10 cm in the tissue.

f [kHz]	σ_{yell_m} [S/m]	$\epsilon_{r_{yell_m}}$ [-]	a [m]	$L_{tiss,t}(yell_m)$	$L_{tiss,n}(yell_m)$
100	0.00382	111	27.9095	0.001488	7.44118E-07
250	0.0041	65.5	17.55211	0.0039501	4.99163E-06
500	0.00435	49	12.59139	0.0081936	2.1184E-05
750	0.00454	43	10.45914	0.307651	4.97458E-05
1000	0.00471	9.2039	1.602545	0.016682	9.17485E-05

Table 2.10: Electromagnetic parameters for cortical bone, the corresponding skin depth a as a function of frequency and the corresponding reduction of the magnetic field at 10 cm in the tissue.

f [kHz]	σ_{corti} [S/m]	$\epsilon_{r_{corti}}$ [-]	a [m]	$L_{tiss,t}(cortic)$	$L_{tiss,n}(corti)$
100	0.0208	228	11.377	0.0081958	4.05174E-06
250	0.0212	197	7.373	0.020749923	2.58104E-05
500	0.0222	175	5.326	0.042802568	0.000108
750	0.0232	43	158	4.389	0.000254
1000	0.0244	145	3.790	0.091458	0.000475

Notice, that the analytical model above applies a uniform magnetic field tangential to the surface of the human tissue while in the case of cylindrical, pancake, butterfly ... coils, the magnetic field pattern in the direct surroundings contains also a component orthogonal to the tissue. Consequently, in order to quantify the eddy current loss in the neighboring tissue, we also consider a simplified analytical model for the case of a sinusoidal homogeneous magnetic field $H = H_0 \cos(\omega t)$ with z orientation, in a circular area (radius = R) orthogonal to the human tissue and absent outside the circular area, as shown in Fig.2.25(b). In the shown cylindrical coordinate system, the magnetic field strength and the induced electrical field takes the following form:

$$\mathbf{H} = \underline{H}_z \mathbf{1}_z (r < R);\ \mathbf{H}\ = 0\, \mathbf{1}_z (r > R); \mathbf{E} = \underline{E}(r)\, \mathbf{1}_\theta \tag{2.58}$$

Faraday's law in integral form along a circle in the (x,y)-plane and with the origin of the coordinate system as midpoint gives rise to

$$\underline{E}_\theta = -j \frac{r\omega\mu}{2} \underline{H}_z, r < R; \mathbf{E} = \underline{E}_\theta \mathbf{1}_\theta \tag{2.59}$$

and

$$\underline{E}_\theta = -j \frac{R^2\omega\mu}{2r} \underline{H}_z, r > R \tag{2.60}$$

The eddy current loss density due to a normal incident magnetic field (denoted by P_n) is expressed in W/m^3 and given by

$$P_n = \frac{\sigma}{2} \underline{E}_\theta . \underline{E}_\theta^* = \frac{\sigma r^2 \omega^2 \mu^2}{8} H_0^2, r < R \tag{2.61}$$

and

$$P_n = \frac{\sigma}{2} \underline{E}_\theta . \underline{E}_\theta^* = \frac{\sigma R^4 \omega^2 \mu^2}{8r^2} H_0^2, r > R \tag{2.62}$$

with a maximum value at $r = R$ of

$$P_n = \frac{\sigma R^2 \omega^2 \mu^2}{8} H_0^2 = L_{tiss,n} H_0^2 \tag{2.63}$$

As for the power loss coefficients $L_{tiss,t}$, we provide the frequency dependent $L_{tiss,n}$ values for the various tissues, see Tables 2.5-2.10. For the computation of $L_{tiss,n}$ we choose $R = 5$ cm since this is a realistic overestimation for the considered cylindrical, pancake and butterfly coils. The values in the tables show the strong frequency dependence of the $L_{tiss,t}$ and $L_{tiss,n}$ due to the strong frequency dependence of the tissues' permittivity and to a less extend the tissues' conductivity. We can furthermore observe from the values in the tables that $L_{tiss,t}$ has values that are much higher than the $L_{tiss,n}$ values. We can consequently state that in order to keep the eddy current loss in the tissues sufficiently low, a field pattern with a normal field component is more preferable than a field pattern with a tangential component to the tissue. Analyzing the field patterns in Figs.2.18, 2.19, 2.20 and 2.21, it is clear that for the same magnetic field level a pancake type coil gives rise to less eddy current loss than a butterfly coil.

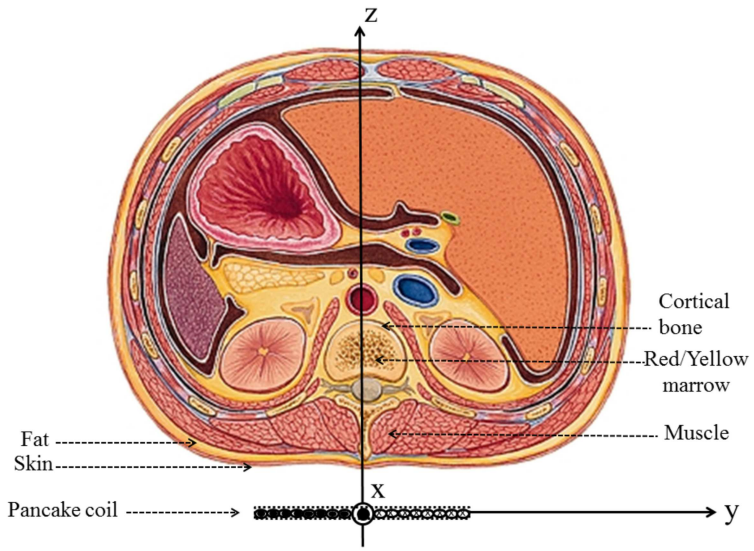

Figure 2.26: Scheme of the different tissue layers for the quantification of the eddy current loss

In order to have a rough estimation for the eddy current loss in the tissues, we start from the cross section of the body of Fig.2.26 and consider a simplified geometry containing a skin layer of 0.5 cm, a fat layer of 1 cm, a muscle layer of 2.5 cm,

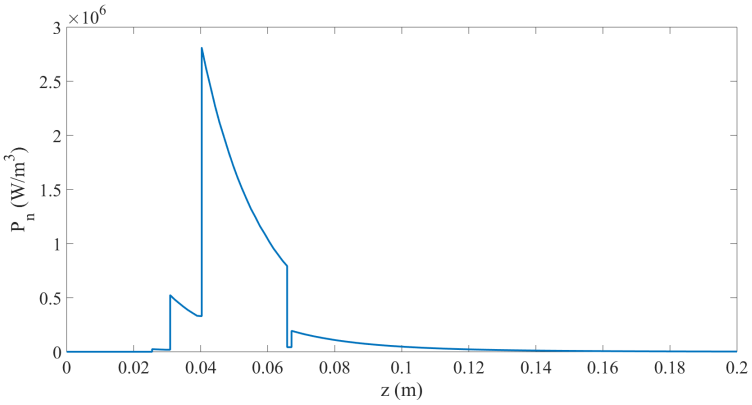

Figure 2.27: The eddy current loss values in the different tissues under normal field magnetic field conditions along the symmetry axis of the pancake coil of Fig.(2.26), applying (2.63) and at 250 kHz. Notice the jump in P_n at each surface between different tissues.

a cranial bone layer of 0.2 cm and a yellow/red layer of marrow bone of 5 cm. Taking into account the field pattern of Fig.(2.19) and (2.21), we approximate the field pattern as a magnetic field oriented along the z-axis uniform within each circle (radius R= 0.05 m, midpoint on z-axis) parallel to the xy-plane and with a decay along the z-direction as given in Fig.2.9. When positioning the pancake coil 2.5 cm from the skin surface, the z-dependence of the eddy current loss $[W/m^3]$ obtained by (2.63) at 250 kHz and 100 A in the coil is shown in Fig.(2.27). Notice that the eddy current loss is the highest in the muscle region under the skin and fat region.

Finally, it is clear that the eddy current loss in the yellow/red marrow bone is much lower than the heat produced by 1 gram of magnetic nanoparticles – see data in Appendix A.

We conclude from the above that the magnetic field at the position of the spine and spinal cord is hardly affected by the shielding of the human tissue and that a coil producing a normal magnetic field such as a pancake coil is the utmost preferred coil topology.

2.8 Conclusion

This Chapter considered in detail the alternating magnetic field that is generated by an inductor-capacitor circuit. Starting from the fundamentals of the inductor-capacitor circuit and low frequency electromagnetism, analytical descriptions for the magnetic field and self-inductance were drawn in Section 2.4 for short cylindri-

cal, helical and pancake coil topologies. The magnetic field strength calculations can not be considered without the self-inductance values as the latter affects the resonance frequency of the inductor-capacitor circuit. We also validated the use of the quasi-static approximation and the analytical expressions by comparing the analytical simulations with finite element based simulations of the magnetic field and the self-inductance values. We subsequently (Section 2.5) analyzed whether we can scale up small coils towards large coils wherein a large animal or human is placed in. This led us to conclude that this is technologically limited: unrealistic high voltages over the coil and over the capacitor bank, as well as high voltages between neighboring coil turns and capacitor banks that would require a very high number of parallel branches and series connected capacitor elements as these elements pose limits due to their maximal voltages and currents they can withstand. Contrary to scaling up existing helical coils that are currently used for magnetic hyperthermia of small animals or cell cultures we exploited in Section 2.6 the presence of the magnetic fields outside the excitation coils. We selected the pancake coil topology over cylindrical, helical and butterfly coil topology as being the most suitable topology for generating a maximal magnetic field strength at a certain distance from the coil for performing magnetic hyperthermia. This was concluded after mapping the magnetic field strengths at a certain distance from the coils to the self-inductance values for the various coil topologies. After the performed optimizations we analyzed in Section 2.7 the effect that the electrically conducting human body has on the attenuation of the magnetic field inside the human body and to what eddy current losses this leads. Results furthermore show that the magnetic field at the position of the spine and spinal cord is hardly affected by the shielding effect of the human tissue. We concluded in that section that having normal magnetic fields incident to the human body is preferred compared to tangential magnetic fields as this leads to lower eddy current losses. This again advocates the use of a pancake coil, certainly over a butterfly coil topology, as the excitation coil topology for generating the alternating magnetic fields that will interact with the materials to produce heat in the vicinity of the bone metastases.

3

Heat generation of materials subject to alternating magnetic fields

'There are no incurable diseases - only the lack of will. There are no worthless herbs - only the lack of knowledge.'

Avicenna

3.1 Introduction

Previous Chapter 2 treated how coils generate a magnetic field and how they can be geometrically optimized taking into account the requirements with respect to resonance frequency (that is affected by the inductance value of the excitation coil) and the requried magnetic field strength. In this chapter we place material in an alternating magnetic field (AMF) that due to the interaction of the materials with the magnetic field generate heat. We consider in this chapter heat generation of both non magnetic conducting materials (Section 3.2) as magnetic materials (Section 3.3).

Non magnetic conducting materials subject to alternating magnetic fields generate heat due to eddy current losses. These losses are estimated in Section 3.2 for different conducting materials such as carbon and titanium materials that are applied in other biomedical engineering applications for implants. As stressed in Chapter 1, an important prerequisite of hyperthermia and specifically for the treatment of

bone metastases is that the materials need to maintain compatibility with respect to magnetic resonance imaging (MRI). Next to the power losses that non magnetic conducting materials generate when subject to alternating magnetic fields we study their MRI compatibility.
Section 3.3 considers magnetic materials and first describes the physical mechanisms that give rise to heat when having these materials subject to an alternating magnetic field. The mechanisms are described based on the energies and losses of each type of material. The specific loss mechanisms in magnetic materials are related to hysteresis loss, eddy current loss (since they can be conducting), and the important Néel and Brownian relaxation loss mechanisms in magnetic nanoparticles (MNP). State of the art considers the linear response theory for estimating the power loss of magnetic nanoparticles and we propose a correction of the linear response theory with respect to the size of the magnetic nanoparticles by considering their lognormal distribution.
Since we need to maintain mechanical stability, the materials that give rise to heat need to be mixed with PMMA for the treatment of bone metastases. Section 3.4 experimentally determines the heat generated by the mixture PMMA+MNP using the calorimetric method. As in Section 3.2 we also study the compatibility of these materials towards MRI and how that restricts the amount of concentration of MNP in the PMMA+MNP mixtures. Finally, a proper protocol for magnetic hyperthermia is drawn in this chapter.

3.2 Heat generation in non-magnetic materials

Various materials have been used for many decades in different medical applications. Advances in the synthesis and characterization of non-magnetic conducting materials, especially titanium alloys and carbon, have been used for implant application [84], minimally invasive surgery and hyperthermia applications [85].
Non-magnetic materials are materials that are not attracted to an external magnetic field. They show no or slight response to a magnetic field. The most commonly non-magnetic metals used in biomedical applications are alloys of copper, titanium and aluminum. Their good mechanical properties, wear resistance, and durability make them good materials for many orthopedic and dental applications [86] [87] [88]. The possibility of using these materials in hyperthermia procedure is limited to their ability of producing sufficient power to heat tumors. Eddy current losses is the main mechanism for heat production of non-magnetic conducting materials subject to an alternating magnetic field.

3.2.1 Eddy current loss

Let us consider a particle being a sphere with radius R and characterized by material properties permeability μ, permittivity ϵ, and electrical conductivity σ. This sphere is located in an AMF with induction field

$$\mathbf{B} = B_m \cos(\omega t + \phi)\mathbf{1}_z \tag{3.1}$$

having amplitude B_m, angular frequency $\omega = 2\pi f$ and that is homogeneous with specific fixed direction (here we assume that this is in the z-direction). Figure 3.1 schematically represents this sphere that is subject to an induction field **B**. Since we consider frequencies in the range of 100 kHz to 700 kHz, the induction field (3.1) has a free-space wavelength $\lambda = c/f$ (with speed of light $c = 1/\sqrt{\mu_0 \varepsilon_0}$) that is much greater than the considered sphere radius. Otherwise high frequency electromagnetic computations need to be carried out. The aim of this study is to derive the free-current density $\mathbf{J}_f$ induced in a spherical particle. From these current densities we will derive the time-averaged electromagnetic power P dissipated within the particle.
We start from Maxwell's equations introduced in subsection 2.3.1 together with the constitutive equations; Ohm's law is used:

$$\mathbf{J}_f = \sigma \mathbf{E} \tag{3.2}$$

as well as the relationship of the electric displacement to the electric field, i.e.

$$\mathbf{D} = \epsilon \mathbf{E} \tag{3.3}$$

and

$$\mathbf{B} = \mu \mathbf{H} \tag{3.4}$$

By taking the curl operator on (3.2), we have

$$\nabla \times \mathbf{J}_f = \sigma \nabla \times \mathbf{E} \tag{3.5}$$

The right hand side can be rewritten as follows by using Faraday's law (2.7):

$$\nabla \times \mathbf{J}_f = -\sigma \frac{\partial \mathbf{B}}{\partial t} \tag{3.6}$$

Next to this governing equation for the free-current density $\mathbf{J}_f$, a next equation can be found by applying the curl operator on (3.6):

$$\nabla \times (\nabla \times \mathbf{J}_f) = -\sigma \frac{\partial \nabla \times \mathbf{B}}{\partial t} \tag{3.7}$$

assuming that we have a homogeneous spherical particle (i.e. constant σ values). Replacing **B** in (3.7) with the expression of the material law (3.4) and using Maxwell-Ampère law (2.8) results in

$$\nabla \times (\nabla \times \mathbf{J}_f) = -\sigma \mu \frac{\partial \nabla \times \mathbf{H}}{\partial t} \tag{3.8}$$

$$\nabla \times (\nabla \times \mathbf{J}_f) = -\sigma\mu\frac{\partial \mathbf{J}_f}{\partial t} - \epsilon\mu\frac{\partial^2 \mathbf{J}_f}{\partial t^2} \tag{3.9}$$

where also the constitutive relations (3.2) and (3.3) were inserted. Gauss's law (2.9) results in the following equation for the $\mathbf{J}_f$ when using (3.3) and (3.2):

$$\nabla \cdot \mathbf{J}_f = \frac{\sigma}{\epsilon}\rho_c \tag{3.10}$$

Divergence equation (3.10) can be related to the equation of continuity (2.11) giving rise to the following dynamic equation for the free charges ρ_c:

$$\frac{\sigma}{\epsilon}\rho_c = -\frac{\partial \rho_c}{\partial t} \tag{3.11}$$

with solution $\rho_c(t) = \rho_0 \exp(-\frac{t}{\tau_\rho})$ that will decay from the initial free charge ρ_0 with decaying time constant $\tau_\rho = \frac{\epsilon}{\sigma}$. At sufficiently low frequency, we have $\nabla \cdot \mathbf{J}_f = 0$.
We use (3.9) as starting point to derive the governing equation for the $\mathbf{J}_f$. Identity $\nabla \times (\nabla \times \mathbf{J}_f) \equiv \nabla(\nabla \cdot \mathbf{J}_f) - \nabla^2 \mathbf{J}_f$ is used together with the fact that the effect of charge separation can be ignored at low frequencies (i.e $\nabla \cdot \mathbf{J}_f = 0$) to derive the following equation:

$$-\nabla^2 \mathbf{J}_f = -\sigma\mu\frac{\partial \mathbf{J}_f}{\partial t} - \epsilon\mu\frac{\partial^2 \mathbf{J}_f}{\partial t^2} \tag{3.12}$$

that transforms in the frequency domain into

$$\nabla^2 \underline{\mathbf{J}}_f + (-j\sigma\mu\omega + \mu\epsilon\omega^2)\underline{\mathbf{J}}_f = 0 \tag{3.13}$$

Introducing the spatial propagation constant

$$k = \sqrt{\mu\epsilon\omega^2 - j\sigma\mu\omega} = \sqrt{\omega\mu(\epsilon\omega - j\sigma)} \tag{3.14}$$

gives the following reformulation of (3.13):

$$\nabla^2 \underline{\mathbf{J}}_f + k^2 \underline{\mathbf{J}}_f = 0 \tag{3.15}$$

Note that in (3.14) for non-magnetic particles, $\epsilon\omega \ll \sigma$ is valid for the considered frequency ranges and that the permeability is the permeability of free space. The propagation constant can thus be written as

$$k = \sqrt{-j\omega\mu\sigma} \tag{3.16}$$

The electromagnetic skin depth

$$\delta = \sqrt{\frac{2}{\mu\sigma\omega}} \tag{3.17}$$

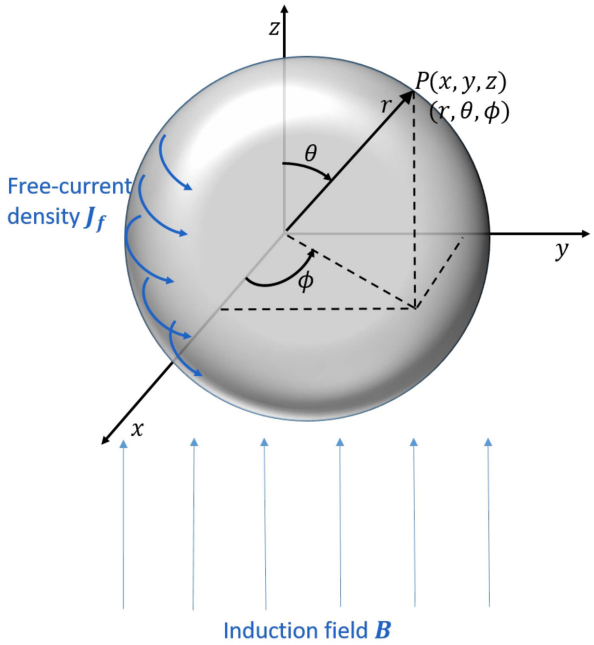

Figure 3.1: External induction field incident to a conducting sphere, generating a free-current density $\underline{\mathbf{J}}_f$. The spherical coordinate system (r, θ, ϕ) for a certain spatial coordinate (x, y, z) is schematically shown.

can be inserted into (3.16) leading to

$$k = \frac{\sqrt{-2j}}{\delta} \tag{3.18}$$

We need to find a solution for the Helmholtz equation (3.15).
Figure 3.1 shows the spherical coordinate system (r, θ, ϕ) for a certain spatial coordinate. Since we consider a spherical particle, we have that the currents have only an azimuthal (with direction $\mathbf{1}_\phi$) component due to symmetry reasons and that furthermore we can separate the r and θ variables into a function $f(r)$ and $\sin(\theta)$ respectively [89]:

$$\underline{\mathbf{J}}_f = \underline{J}_\phi \mathbf{1}_\phi = \underline{f}(r)\sin(\theta)\mathbf{1}_\phi \tag{3.19}$$

When substituting (3.19) in (3.15) we have

$$(\frac{\partial^2}{\partial r^2} + \frac{2}{r}\frac{\partial}{\partial r})\underline{J}_\phi + \frac{1}{r^2\sin(\theta)}\frac{\partial}{\partial\theta}(\sin(\theta)\frac{\partial}{\partial\theta})\underline{J}_\phi + \frac{1}{r^2\sin^2(\theta)}\frac{\partial^2}{\partial\phi^2}\underline{J}_\phi + k^2\underline{J}_\phi = 0 \tag{3.20}$$

that using the separation of variables (3.19) becomes

$$\frac{\mathrm{d}^2\underline{f}(r)}{\mathrm{d}r^2}+\frac{2}{r}\frac{\mathrm{d}\underline{f}(r)}{\mathrm{d}r}+(k^2-\frac{2}{r^2})\underline{f}(r)=0 \tag{3.21}$$

This equation (3.21) has the general solution $\underline{f}(r) = Aj_1(kr) + By_1(kr)$ with $j_1(\cdot)$ and $y_1(\cdot)$ being spherical Bessel functions of the first and second kind. Since $y_1(kr)$ diverges at $r = 0$, the coefficient B must equal zero, thus leading to

$$\underline{f}(r) = Aj_1(kr) \tag{3.22}$$

The coefficient A can be determined on the basis of satisfying the boundary conditions for the magnetic field at the radius of the sphere $r = R$. For further details, we refer to [89]. The power dissipated in the spherical particles can be calculated as

$$Q=\frac{1}{2\sigma}\int \underline{J}_\phi\cdot\underline{J}_\phi^*\mathrm{d}V \tag{3.23}$$

using (3.19) with (3.22) and where the propagation constant is determined by (3.18) with skin depth (3.17). We obtain the following power dissipated in the spherical particle [89]:

$$Q(W)=\frac{\pi\sigma\omega^2R^5B_m^2}{15}(1-\frac{4R^4}{105\delta^4}) \tag{3.24}$$

when assuming particles with radius $R \ll \delta$, the factor $(1 - \frac{4R^4}{105\delta^4}) \approx 1$ and the power dissipated per sphere volume becomes:

$$P(W/m^3)=\frac{3}{15}\sigma\pi^2R^2f^2B_m^2 \tag{3.25}$$

The power lost per mass unit of non-magnetic material, later named specific loss power (SLP) is expressed in Watt per gram as follows:

$$SLP_{eddy}(W/g)=\frac{3}{15\rho}\sigma\pi^2R^2f^2B_m^2 \tag{3.26}$$

where $\rho(g/m^3)$ is the mass density of the non-magnetic material.

3.2.2 Analytical estimation of losses in non-magnetic particles

Based on the above analytical expressions for the SLP that arises in conducting non-magnetic particles due to eddy current losses, we compare three different materials. We consider two materials that are also considered in other biomedical engineering applications such as for implants but also for hyperthermia. We also examine the SLP in iron oxide particles (that are magnetic) but that are also electrically conducting. The parameters characterizing these particles and that affect

the SLP, i.e. radius R, electrical conductivity σ, mass density ρ, are specified in Table 3.1. Material values are based on the standard works [3-4]. We assume that the spherical particles are in a homogeneous AMF (see Fig. 3.1) at a frequency of $f = 250$ kHz and a magnetic field amplitude of $H = 15$ kA/m, that corresponds with an induction magnetic field $B_m = \mu_0 H_m = 0.01884$ T. The largest SLP due to eddy current losses can be observed for the Titanium B material having a relatively large radius R. The Carbon A and B fail to generate sufficiently high SLP due to eddy current losses due to their relatively lower electrical conductivity when compared to their Titanium counterpart. From (3.26) we can deduce that the radius has a quadratic effect on the specific loss power. For instance when comparing the Titanium B with the eddy current losses in MNP having a nm radius leads to significantly lower SLP even though the electrical conductivity is larger. Having MNP that has an inherent high mass density makes it such that the SLP is worsened. One could deduce that having MNP in the micrometer range would result in large eddy current SLP; however it is technologically difficult to manufacture MNPs with radius in the order of 100 nm. Even then the SLP due to eddy currents remains too small to have significant heating due to eddy currents losses. In this section, SLP values are computed on the basis of (3.26) in 3 different materials: titanium, carbon and iron oxide particles. The radii, electical conductivities and densities of the particles are presented in Table 3.1. The AMF used has a frequecy f=250 kHz and an amplitude H=15 kA/m (B_m=0.01884 T).

Table 3.1: Properties of the considered sample types and the resulting SLP values when applying a magnetic field f= 250 kHz and H=15 kA/m (B_m=0.01884 T) [7] [8]

Material	**R** (μm)	σ **(S/m)**	ρ **(g/m^3)**	**SLP**$_{eddy}$ **(W/g)**
Titanium A	45	2.38 10^6	4506000	0.0468
Titanium B	150	2.38 10^6	4506000	0.5209
Carbon A	50	10^3	3515000	3.11 10^{-4}
Carbon B	300	10^3	3515000	11.22 10^{-4}
MNP	10^{-6}	10^7	5242000	8.362 10^{-21}

3.2.3 Magnetic resonance imaging of non-magnetic particles

After treating the tumor with hyperthermia sessions, regular medical examinations are required for evaluating the treatment efficacy as well as to follow up the condition of the surrounding tissue. Since the particles remain fixed in the PMMA-based bone cement, and thus in the bone of the patient, these particles might disturb medical monitoring. It is therefore key to verify whether the artifacts caused by the particles in the medical imaging modality - magnetic resonance imaging (MRI) -

remain limited. In the case of bone metastases hyperthermia, we assume MRI artifacts bigger than 2 mm as unacceptable [74]. We experimentally analyze what the effect is of having PMMA mixed with non-magnetic particles on the MRI artifacts.

3.2.3.1 Physical principles of magnetic resonance imaging

The principles of magnetic resonance image (MRI) generation are based on the alignment within the body of the hydrogen protons (H^+) in water molecules, both parallel and antiparallel to the static magnetic field of the MRI magnet. A radiofrequency (RF) field is applied in the plane perpendicular to the field axis and as this field is matched to the natural (Larmour) precession frequency of the hydrogen protons in the water, they are knocked out of alignment with the field. Once the RF field is removed, the protons precess back into alignment with the static field. This return to alignment consists of two components that can be measured; (i) the growth of the signal along the field axis as the protons return to alignment with the field, and (ii) the decay of the signal in the plane perpendicular to the field axis as the proton spins lose phase coherence once the RF field is removed. These two signals are known as T_1 and T_2, respectively.
Introducing metallic particles into the body impedes obtaining optimal images, leading to misinterpretation of pathologies and the inability to conclude a diagnosis. Metal-related artefacts depend on the composition, size and orientation of the metallic object with regard to the direction of the external magnetic field [90]. Therefore, it is important to distinguish materials with exuberant artefacts on MRI to be eliminated in the case of hyperthermia for bone metastases.

3.2.3.2 PMMA samples preparation

For experimentally investigating the artifacts caused by non-magnetic particles, samples were prepared. The samples are made by mixing $VertaPlex^{TM}$ radiopaque bone cement (manufactured by $Stryker$) with non-magnetic particles. We consider 3 types of samples that each constitute of titanium, carbon and aluminium. The titanium and carbon powders have 2 different particles sizes with the radii mentioned in Table 3.1. First, the non-magnetic particles are mixed with the PMMA powder (Fig.3.2a) in a homogeneous manner (Fig.3.2b) after which the MMA liquid is added (Fig.3.2c). After stirring the mixture thoroughly in under three minutes, it is poured into cylindrical molds (Fig.3.2d) to have standerdized samples (length of 40 mm and diameter of 9 mm). After 20 min, samples are completely hardened (Fig.3.2e) which allows us to remove them from the molds. The samples are prepared in such a way that they consist in concentration (more specifically in weight percentage (wt%)) of 50% PMMA and 50% non-magnetic particles. This resulted in 5 samples consisting of non-magnetic material X, see Table 3.2.

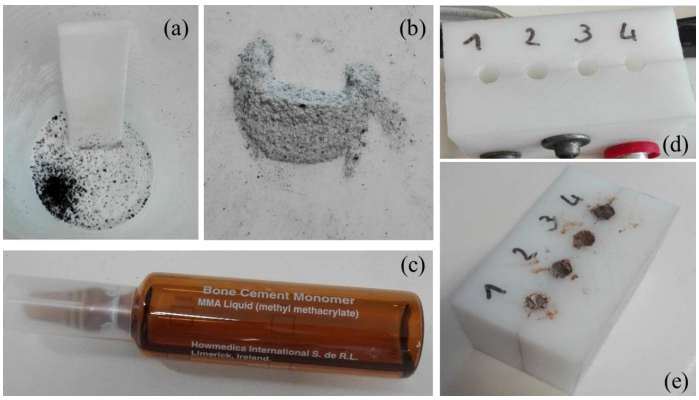

Figure 3.2: PMMA samples preparation: (a) Particles mixed with PMMA powder (b) Homogenization of the mixture (c) MMA liquid (d) Empty mold used to obtain standardized samples (e) Hardening of samples.

3.2.3.3 Magnetic resonance imaging disturbance of non-magnetic particles

To analyse the MRI artifact caused by the non-magnetic samples, each sample was placed in the center of an agar gel phantom. Imaging was performed in a Siemens Trio TIM 3.0T. T_1-weighted images were acquired from the phantoms using an MP-RAGE sequence (repetition time = 2250 ms, echo time = 4.2 ms, flip angle = 9 degrees, field of view 256×256×176 mm^3 and voxel size 1×1×1 mm^3). The prepared 5 samples consisting of material X (see Table3.2) are tested. The transversal slice obtained during MRI is shown in Fig.3.3. Results show that all samples cause a clear artifact when applying a magnetic field. The PMMA with aluminium sample gives rise to the lowest MRI artifacts compared to titanium and carbon samples. However, for all materials, having accurate MRI diagnosis is not possible with the resulting disturbance. We conclude that the concentration of 50% is not tolerable when using the materials mentioned in Table3.2. In that case, we should reduce the amount of the particles used in the PMMA mixture to limit the MRI artifact. However, decreasing concentration of particles directly lead to reduced heat production of the particles, i.e. less grams of non-magnetic particles having a certain specific loss power (3.26) lead to reduced power P(W). In fact, to obtain an efficient hyperthermia treatment a minimum temperature increase of 8°C should be reached. The 5 prepared samples were placed in the AMF of an inductor-capacitor magnetic hyperthermia device with helical coil (number of turns=8, length = 32 mm, diameter = 32 mm). The excitation current in the coil was $I = 100$ A [1] (calculated H=25 kA/m) and had a resonance frequency $f_r = 400$ kHz. The non-magnetic samples - even at a high concentration of 50

[1]The values of the AC current considered during the experiments described in this PhD are always RMS values, except otherwise mentioned.

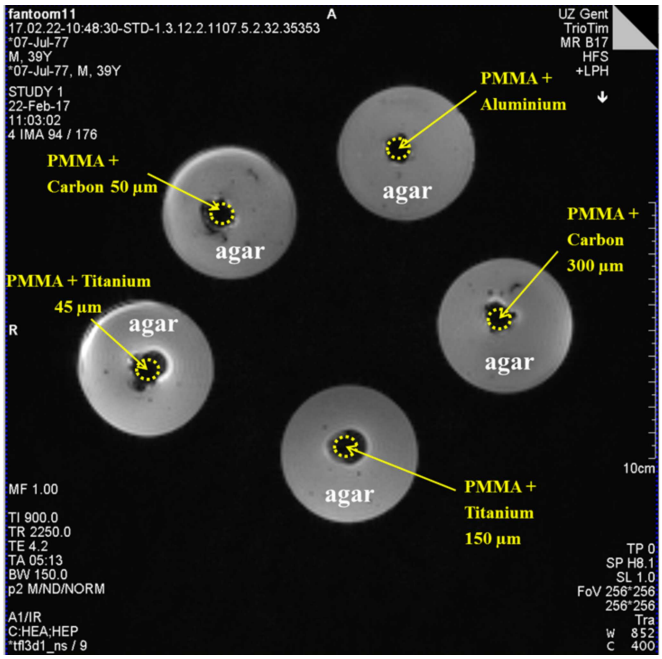

Figure 3.3: T_1- weighted sequence of 5 PMMA and non magnetic particles samples in 2,5% agar gel. The dotted yellow lines indicate the position of the PMMA with non-magnetic material sample.

Table 3.2: Considered sample types and the corresponding temperature increase ΔT after applying during one hour a magnetic field (I=100 A / H=25kA/m and f=400 kHz).

Material X	**conc (wt%)**	**Particles size**	**ΔT (°C)**
Titanium A	50%	45 μm	6.5
Titanium B	50%	150 μm	6.5
Carbon A	50%	50 μm	7
Carbon B	50%	300 μm	7.4
Aluminium	50%	-	5.6
MNP	50%	10 nm	65

percent - gave rise to a temperature increase of less than 8°C after one hour which is small in comparison to experimental results for multicore BNF MNPs. As a conclusion, non-magnetic particles are much less suitable for bone metastases hyperthermia as they cause artifacts on magnetic resonance images and because they produce less heat than the considered MNPs.

3.3 Heat generation of magnetic materials

In this section we present magnetic materials that when interacting with an AMF generate heat. We first introduce the types of magnetic materials (subsection 3.3.1) and their physical principles of magnetism (subsection 3.3.2). In subsection 3.3.3 we detail the magnetic nanoparticles' properties. The loss mechanisms that specifically result in heat are presented in subsection 3.3.4. We present a widely used theory - linear response theory - for calculating the heat generated by magnetic nanoparticles in 3.3.5; together with an analysis of the size dependence of MNP on the generated heat that corrects the linear response theory in subsection 3.3.6.

3.3.1 Types of magnetic materials

Magnetic materials can be classified depending on their response to an external AMF. Every material has paired electrons and thus a diamagnetic contribution. When applying a magnetic field, the electrons try to oppose the AMF. Consequently, diamagnets obtain a negative net magnetic moment when a positive magnetic field is applied. Unpaired electrons can align themselves with the AMF and thus have a positive paramagnetic response besides the diamagnetic response. Therefore paramagnets have a positive net magnetic moment when a positive magnetic field is applied. Materials are classified as magnetic when they have a net magnetic moment in the abscence of a magnetic field. In ferromagnetic materials a strong exchange interaction is present, dominating the diamagnetic response. Antiferromagnetism is like ferromagnetism a manifestation of ordered magnetism and occurs in materials where the magnetic moments of atoms or molecules align but have opposing directions. When there is no external magnetic field, the total magnetization vanishes. Ferrimagnets are another type of magnetic materials that are a special case of antiferromagnets. Their opposing magnetic moments are however unequal leading to a net magnetization when there is no magnetic field applied. Magnetite (Fe_3O_4) and maghemite (γFe_2O_3) are members of the family of iron oxides and are the most well known type of materials that exhibit ferrimagnetism. Magnetite has the strongest magnetic moment of all the naturally occuring minerals on earth. Magnetic particles often consist of iron oxides and are known to have a simple domain structure. Mainly because of their magnetic properties and high magnetic moment they are useful in biomedical engineering to interact with an AMF that is externally applied. Moreover, they have a low cytotoxic effect on biological tissue. On the one hand magnetic particles can be used to force them towards a certain region in the body, e.g. magnetic drug targeting. On the other hand they can generate heat when interacting with an AMF, also called magnetic hyperthermia, a property that is used within this dissertation. Below a critical size, magnetic particles obtain a single domain structure. The transition from multi-domain to single domain particles depends on their composition and crystalline

structure. The critical size for magnetic particles to obtain a single magnetic domain typically ranges between 50 and 100 nm, see e.g. [91] and [92]. Magnetite for instance has a critical limit of the order of 50 nm.
The collective behavior of the atomic magnetic moments is the result of the minimization of the total energy in the system. The balance between the different energy contributions is detailed further in 3.3.2.

3.3.2 Physical principles of magnetism

In order to magnetize a certain volume V of magnetic material, the different interactions between the magnetic moments need to be overcome. Indeed, magnetic materials can be magnetically described as a collection of magnetic dipoles or magnetic moments (per unit volume). Moreover, the magnetic behavior as a function of the applied magnetic field can be considered as the result of rearrangements of these magnetic moments. This is explained as follows: when a magnetic dipole, with magnetic moment $\boldsymbol{m}$ [A$\cdot$ m^2], is placed in a magnetic field $\mathbf{H}$, the magnetic moment aims at aligning with the magnetic field $\mathbf{H}$. This can be described by a minimization of a potential energy W_p [J], defined by:

$$W_p = -\mu_0 \boldsymbol{m} \cdot \boldsymbol{H}. \tag{3.27}$$

The macroscopic magnetization vector $\boldsymbol{M}$ in the material, averaged out over a volume V of the material and denoted by $\boldsymbol{M}$ [A/m], is obtained by the vectorial average of all magnetic moments $\boldsymbol{m}$ in the volume V:

$$\boldsymbol{M} = \frac{1}{VN_d} \sum_{i=1}^{N_d} \boldsymbol{m} \tag{3.28}$$

with N_d the number of dipoles present in the volume V for which the macroscopic magnetization vector is considered. Then, the question arises how the magnetic field $\mathbf{H}$, acting on the magnetic moments $\boldsymbol{m}$ in the material, is defined. Here, the principle of minimizing a potential energy is used for analyzing static conditions while the precessional rotation of $\boldsymbol{m}$ around $\mathbf{H}$ can be analyzed in order to study dynamic effects.

3.3.2.1 Gibb's free energy

In micromagnetic theory, the magnetic moments $\boldsymbol{m}$ of the atoms are homogenized to a continuum vector field $\boldsymbol{M}(\boldsymbol{r})$. This continuum vector field has a fixed, material dependent amplitude M_s, but a time and space varying orientation. This micromagnetic vector field describes the magnetic state of the magnetic material. In principle, this local magnetization represents the magnetic moment per unit volume.

The total potential energy of a magnetic material is given by the Gibbs free energy W_{Gibbs}. In particular, we are interested in all contributions to the Gibbs free energy, relevant for magnetic nanoparticles, which depends on the local magnetization $\boldsymbol{M}(\boldsymbol{r})$:

$$W_{Gibbs} = W_{exch} + W_{anis} + W_{ms} + W_{appl} + W_{th} \tag{3.29}$$

The different magnetic free energy contributions that can be found in (3.29) are treated here after separately in more detail. The Gibbs free energy has the following free independent (input) variables: the externally applied magnetic field $\boldsymbol{H}_{appl}(\boldsymbol{r})$, the elastic stress tensor $\boldsymbol{\epsilon}(\boldsymbol{r})$, and the temperature T. The basic problem in micromagnetism is then to find the local magnetization direction of $\boldsymbol{M}(\boldsymbol{r})$ as a function of position and time, that correspond to the lowest total free magnetic energy.

3.3.2.2 Exchange energy

The exchange energy contribution W_{exch} favors the parallel alignment of neighboring atomic magnetic dipole moments. This type of interaction is also called a short-range dipole-dipole interaction. When one takes into account only the exchange energy in (3.29), the complete parallel alignment of all atomic magnetic moments in the magnetic material sample should be favored when minimizing $W_{Gibbs} = W_{exch}$. However, a preferred direction for this uniform alignment is not defined. Indeed, this exchange energy term is isotropic, which means that it is independent of the spatial direction in which the material is magnetized. However, in reality, the magnetic crystal(s), present in the materials under consideration, are not isotropic. This is taken into account by the anisotropy energy term.

3.3.2.3 Anisotropy energy

The anisotropy energy contribution W_{anis} favors the alignment of all atomic magnetic moments along certain well defined anisotropic directions. In the case of crystallographic anisotropy, these anisotropic directions are fixed to the crystal lattice. The non zero anisotropy energy is caused by those magnetic moments having a different direction compared to the crystallographic easy directions and is called in the case of crystallographic anisotropy short-range dipole-lattice interactions.
In the case that one takes into account only the magnetocrystalline anisotropy energy, the complete alignment of all atomic moments parallel to a direction of easy magnetization is favored. The exchange interaction tends to align all magnetic moments parallel, no matter in which direction, whereas the actual direction of magnetization is determined by the magnetocrystalline anisotropy. Indeed, when one takes into account the exchange energy and the magnetocrystalline anisotropy energy in (3.29), the parallel alignment should lead to an uniform magnetization

of one crystal or grain along one of the preferable crystallographic directions of that grain. A region within a magnetic material which has an uniform magnetization is also called a *magnetic domain*. From experiments it is observed that for polycrystalline materials, a grain often contain multiple regions with uniform magnetizations, i.e. multiple domains. Therefore, an explanation is needed why a configuration with multiple domains arise. The driving term in (3.29) for multiple domain formation is the magnetostatic energy.

3.3.2.4 Magnetostatic energy

The magnetostatic energy contribution W_{ms} in (3.29) favors a change in the arrangement of the local magnetic moments into a structure of multiple magnetic domains. The regions separating neighboring magnetic domains are called *magnetic domain walls*, where the magnetization rotates coherently from the direction in one domain to that in the next domain.

The magnetostatic energy arises W_{ms} from the classical interaction of an individual magnetic moment with the magnetic field produced by all other magnetic dipole moments. The latter is called the magnetostatic field $\boldsymbol{H}_{ms}$. Therefore the magnetostatic energy is a long-range effect of dipole-dipole interactions, contrary to the anisotropy energy and the exchange energy, which are short-range effects. The magnetostatic field originates from the fictitious magnetic charge density, which arises wherever $\nabla \cdot \boldsymbol{M}$ is nonzero ($\boldsymbol{M}$ turns out to be varying in space).

The magnetostatic energy contribution favors a change in the arrangement of the local magnetic moments into a multiple domain structure with main magnetic domains and closure magnetic domains, in such a way that magnetic charges and the corresponding (stray) magnetostatic fields tend to be minimal. Nevertheless, a structure with multiple domains inherently leads to an increase of the anisotropy and exchange energy in the small interface regions between the domains (magnetic domain walls), but as long as this energy increase is smaller than the decrease in magnetostatic energy, the creation of additional domains is favored.

3.3.2.5 Externally applied field energy

The applied field energy W_{appl} is the energy that arises when a magnetic moment m_d or alternatively the local magnetization $\boldsymbol{M}_d(\boldsymbol{r})$ is placed in an externally imposed magnetic field. When taking into account only the applied field energy, this energy, resulting from the interaction between the local magnetization and the applied magnetic field, tends to align all magnetic moments parallel to the applied magnetic field.

3.3.2.6 Thermal energy

As described in [93], the effect of the thermal fluctuations field is included in nanomagnetic simulations by adding a stochastic thermal field to the local magnetic field. The thermal field is modeled as a Gaussian stochastic process with zero mean in each space direction. Thermal fluctuations add a stochastic energy term to the Gibbs free energy. Boltzmann statistics describes the average distribution of material particle having a certain energy state in thermal equilibrium. The probability of having a particle in energy state ΔE is typically characterized as being proportional to $\exp(\frac{\Delta E}{k_B T})$ with $k_B T$ being the thermal energy with k_B the Boltzmann constant and T the absolute temperature.

3.3.2.7 Minimization of total magnetic free energy

Magnetic systems are the result of having minimal Gibb's free energy. Considering the different energy terms in (3.29), it is clear that the equilibrium configuration that minimizes the total magnetic free energy is the result of a trade off between the various energy contributions. For instance, a magnetic system with additional domains and hence an increased domain wall surface inherently leads to an increase of the anisotropy energy, exchange energy in the magnetic domain walls, but as long as this energy increase is smaller than the corresponding decrease in magnetostatic energy, the creation of additional domains is favored.
These domain structures can be identified experimentally. Different measurement techniques are described in [5]. An example of a measured domain structure is given in Fig.3.4.

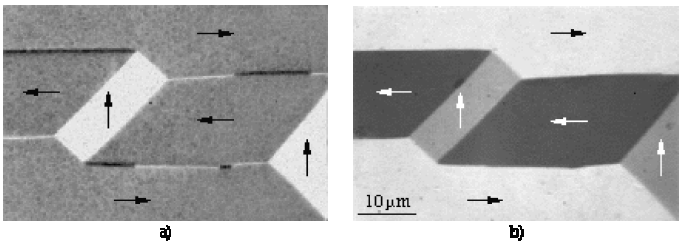

Figure 3.4: Domain and wall images from a (100)-oriented silicon-iron crystal [5].

It is clear that within the magnetic core of the magnetic nanoparticles, considered in this work, the exchange and the anisotropy interaction will be dominant with respect to the magnetostatic interactions between the magnetic dipoles within the considered nanoparticle. Consequently, the magnetic core of a magnetic nanoparticle is a magnetic mono domain or single domain, i.e. the complete alignment of all atomic moments in the magnetic nanoparticle parallel to a direction of easy magnetization is favored. Thus, one magnetic nanoparticle can be considered as

a magnetic macrospin, characterized by a magnetic macromoment. For simplicity this macromoment is henceforth called magnetic moment of the nanoparticle.

3.3.3 Magnetic nanoparticles

As mentioned in previous subsection 3.3.2, materials become magnetized when they are placed in a magnetic field. As before, we denote the magnetization as **M** and the magnetic field as **H**. The function relating the magnetization with the magnetic field is:

$$\mathbf{M} = \chi(\mathbf{H})\mathbf{H} \tag{3.30}$$

Based on the susceptibility χ, three major groups for magnetic materials are identified:
• Ferromagnetic ($\chi > 0$ and a large absolute value)
• Diamagnetic ($\chi < 0$)
• Paramagnetic ($\chi > 0$ and a low absolute value)
In oxides, like magnetite (Fe_3O_4) and maghemite (γ Fe_2O_3) more complex forms of magnetic ordering occur resulting in ferrimagnetic materials. Here the magnetic moments of the different sublattices are not equal resulting in a net magnetic moment. Ferrimagnetism is therefore similar to ferromagnetism. It shows the same properties of ferromagnetic behavior, like spontaneous magnetization, Curie temperature, hysteresis and remanence although ferro- en ferrimagnets have different magnetic ordering. Magnetic particles based on iron oxides may behave as ferromagnetic (detailed in 3.3.3.2) or as a superparamagnetic material (detailed in 3.3.3.1), depending on the size of the particle. Indeed, a single domain magnetic material (e.g. magnetic nanoparticles) due to the small size has no hysteresis loop and is said to be superparamagnetic.

The magnetic induction **B** (T) of the material is defined as:

$$\mathbf{B} = \mu_0(\mathbf{H} + \mathbf{M}) \tag{3.31}$$

Substituting (3.30) in the equation (3.31) above yields an alternative form:

$$\mathbf{B} = \mu_0(\mathbf{H} + \chi(\mathbf{H})\mathbf{H}) \tag{3.32}$$

In general, $\chi(\mathbf{H})$ is a function of **H**. In case of hysteresis phenomena (e.g. ferromagnetic materials) $\chi(\mathbf{H})$ may be undefined.

3.3.3.1 Superparamagnetism

For superparamagnetic materials, the magnetization can be described by the Langevin function $L(\cdot)$ with magnetization

$$M = M_s L(\xi(H)) = M_s[\coth(\xi(H)) - \frac{1}{\xi(H)}] \tag{3.33}$$

where M_s is the saturation magnetization. The variable ξ depends on the applied magnetic field H and is defined as

$$\xi(H) = \frac{\mu_0 \mu_m H}{k_B T}. \tag{3.34}$$

μ_0 is the permeability in free space, μ_m is the magnetic moment, k_B is the Boltzmann constant and T is the temperature. From (3.30) the susceptibility can be defined as:

$$\chi(H) = \frac{M}{H} = \frac{M_s}{H}[\coth(\xi(H)) - \frac{1}{\xi(H)}] \tag{3.35}$$

For high temperatures and small magnetic fields with magnetizations $M \leq 0.20 M_s$ that are here typically considered, $\xi \ll 1$ and the initial slope ($\xi = 0$) of the M(H) function is the initial susceptibility of the sample:

$$\chi_i = \frac{\mu_0 \mu_m M_s}{3 k_B T} \tag{3.36}$$

3.3.3.2 Ferromagnetism

In ferromagnetic materials the $M(H)$ curve shows what is called hysteresis. Having a different magnetizing path and de-magnetizing path defines hysteresis. When applying for instance a sinusoidal (can also be e.g. trapezoidal) magnetic field, this results in a loop of the $M(H)$ curve. The area inside the loop represents the energy that is transferred into the material, resulting in hysteresis loss (see 3.3.4.1). The magnetization can be seen as a loop and the area inside the loop represents the energy that is transferred into the material. Ferromagnetic materials for electrical machines are designed to keep these losses as low as possible. Magnetic nanoparticles do not exhibit hysteresis effects as they constitute of a single magnetic domain. However when they are placed in a high frequency magnetic field a phenomenon called magnetic relaxation occurs. This causes energy transfer from the magnetic field to the magnetic material and the shape of the $M(H)$ curve is then similar to the one of a ferromagnetic material with hysteresis.

3.3.4 Loss mechanisms in magnetic materials

The heat generated in magnetic materials under an alternating magnetic field can be generally ascribed to one of the three different mechanisms, i.e. hysteresis loss (further detailed in 3.3.4.1), eddy current loss (3.3.4.2) and Néel and Brownian relaxation loss (3.3.4.3).

3.3.4.1 Hysteresis loss

Hysteresis loss occurs in multidomain particles (ferromagnetic and ferrimagnetic materials). Magnetic domain walls can move in the presence of an applied magnetic field such that the magnetic domain structure changes. The irreversible processes corresponding with pinning and depinning phenomena of the moving magnetic domain walls result in a non single valued relation between the macroscopic magnetization and the applied magnetic field. If the magnetization is plotted for all strengths of applied magnetic field, the result is a hysteresis loop. The amount of heat generated is directly related to the area of this hysteresis loop. As we may assume that no magnetic domain walls are present in the magnetic core of a nanoparticle, hysteresis loss in the nanoparticle is not considered here.

3.3.4.2 Eddy current loss

Eddy currents are electrical currents that are induced in an electric conductor (metal) that is positioned in an AMF according to Faraday's law. Significant eddy current heating is observed only for bulk magnetic materials, i.e. materials having a radius $R \geq 1$ mm for magnetite. We detailed in Section 3.2 the heat generation in non-magnetic conducting materials and more specifically the eddy current loss in 3.2.1. We derived in that section the specific eddy current loss power of electrical conducting spherical particles located in an AMF, see (3.26). In Table 3.1, we calculated the theoretical SLP of a 1nm radius MNP and we can conclude that eddy current effects can be neglected for iron oxide nanoparticles having a diameter in the range of 10-100 nm.

3.3.4.3 Néel and Brownian relaxation loss

As detailed earlier, both hysteresis loss and eddy current heating are not considered as being large contributors to the heating of MNPs. We sketch here how relaxation phenomena can produce heat. As mentioned in 3.3.2.7 the MNPs having radii in the range of 10-100 nm consist of a single domain with a magnetic macrospin. We denote the magnetization of the MNP as being $\mathbf{M}$. Relaxation phenomena are characterized by their relaxation time τ by which the magnetization $\mathbf{M}$ approaches its equilibrium state $\mathbf{M}_0$:

$$\frac{d\mathbf{M}}{dt} = \frac{1}{\tau}(\mathbf{M}_0(t) - \mathbf{M}(t))$$

The MNPs rotate to align their moments with the equilibrian state producing Néel and Brown relaxation loss.

The heat generation through Néel relaxation is due to changes in the direction of magnetic moments e.g. when applying an external magnetic field the magnetization **M** is not aligning directly with that external field due to the anisotropy energy since the latter tends to align the magnetic domain of the MNP in a direction according to their crystal lattice structure. Figure 3.5 (A) shows that Néel relaxation is directly related to the internal movement (or fixation) of the magnetic moment within the MNP. This movement depends on the magnetic characteristics (anisotropy energy) of the MNP. Brown relaxation follows a different mechanism to produce heat since this corresponds with having the particles physically rotate in order to aline the magnetization with the applied magnetic field (contrary to the rotating or fixed internal magnetization of the particle in Néel) within the dispersed medium. The type of heating (Néel or Brown) also heavily depends on the environment wherein the MNP are located. For example, a MNP in PMMA will be unable to physically rotate thus removing any component of heat produced via Brownian motion. Figure 3.5 (B) depicts schematically the Brown relaxation of the particle itself where the magnetic moment of the MNP remains fixed (direction with respect to the crystal lattice) within the particle.

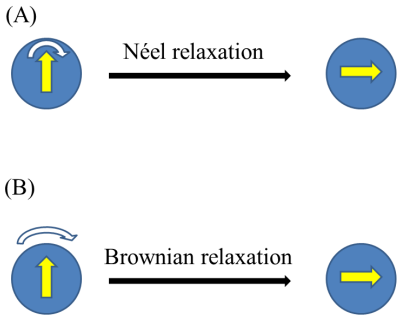

Figure 3.5: Comparison of Néel (A) and Brown (B) relaxation. In Néel relaxation, the particle remains stationary while the magnetic moment rotates within the particle. For Brownian relaxation, the particle itself rotates but the magnetic moment stays in the same direction with respect to the crystalline axes of the particle.

In Brownian relaxation, the magnetic nanoparticle will rotate in its entirety while

the magnetic moment will keep its direction with respect to the crystalline axes of the particle. This is illustrated in case B of Fig.3.5. The rotation of the MNP will cause heating due to shear stresses between particle and surrounding fluid. As a result, heat dissipation in Brownian relaxation is dependent on the hydrodynamic properties of the fluid and the volume of the particle. The relaxation time for Brownian motion is given by (3.37):

$$\tau_B = \frac{3\,\eta\,V_h}{k_B\,T} \tag{3.37}$$

where η is the viscosity of the fluid wherein the MNPs are dispersed, k_B the Boltzmann constant (k_B=1.38 10^{-23} J.K^{-1}), T the absolute temperature (T=300 K). The hydrodynamic volume V_h is mostly taken as being $V_h = (1 + \frac{\psi}{R})^3 V_c$ with $V_c = \frac{4}{3}\pi R^3$ being the core volume of the MNP. R and δ are respectively the radius of MNP and the thickness of a sorbet surfactant layer (ψ=0.01 nm).

For achieving hyperthermia of bone metastases we will use MNP that are completely bound in PMMA. Since the MNP are immobilized in the PMMA, only Néel relaxation is of importance in our studies [64]. As relaxation is characterized by constant τ (see (3.3.4.3)) we will specifically look into the relaxation time due to Néel relaxation τ_N. Néel relaxation can be seen as finding the Boltzmann statistic (see 3.3.2.6) which gives the probability of having relaxation time for given anisotropy energy barrier ΔE. The expression for the relaxation time τ_N can be found in (3.37) with the thermal energy $k_B T$ that can exceed the anisotropy energy barrier ΔE. The orientation states of the magnetic moments follow here a Boltzmann statistic where the thermal energy drives the magnetic moments to fluctuate continuously.

$$\tau_N \;=\; \tau_0\,\exp(\frac{\Delta E}{k_B\,T}) \tag{3.38}$$

τ_0 is the length of time characteristic of the material (its typical value is between 10^{-8} and 10^{-12} s) and is size dependent, ΔE is the required energy to change the direction of the particle's moment and depends on the anisotropy constant K and the magnetic core volume V_c, $\Delta E = K V_c$.This clearly shows that the Néel relaxation time constant (3.38) depends on the physical dimensions of the particle. Contrary to Brownian relaxation, Néel relaxation is not dependent on the local environment of the suspension (such as the viscosity) in which the MNPs are placed. As a result, magnetic particles that dissipate heat via the Néel principle are preferred for use in clinical trials as their results are consistent for *ex-vivo* and *in-vitro* experiments.

When having both Néel and Brown relaxation, the relaxation constant of both phenomena is expressed by (3.39). Note that both mechanisms cannot be fully decoupled. With a constant temperature, the energy barrier of anisotropy will stay the same. Variation of the magnetic field, to which the MNP are subjected, will cause

an imbalance in the total energy and, if the energy is high enough, the anisotropy barrier is surpassed, making the magnetization reverse.

$$\tau = \frac{\tau_B \cdot \tau_N}{\tau_B + \tau_N} \tag{3.39}$$

When comparing Brownian and Néel relaxation it is clear that Brownian relaxation dominates for particles with a larger diameter and in solutions with a lower viscosity. For Néel it is the other way around. Also the inability of the magnetic moment to follow the applied AMF results in heating effects. This heating is described by the imaginary part of the AC susceptibility and is a combination of Brownian and Néel relaxation.

3.3.5 Linear Response Theory

3.3.5.1 Theory

Linear response theory (LRT) is a theoretical model that describes the dynamic response of an ensemble of non-interacting single domain MNPs to a time-varying magnetic unidirectional external field [94]. We will present here the basic theory of the LRT based on [95]. A time-varying magnetic field $H(t) = H_0 \cos(\omega t)$ is applied with angular frequency ω and amplitude H_0. The time-varying magnetization response of the MNPs is given as follows:

$$M(t) = H_0 \chi^{'} \cos(\omega t) + H_0 \chi^{''} \sin(\omega t) \tag{3.40}$$

Here, $M(t)$ is the component of the magnetization vector $\mathbf{M}(t)$ along the direction of the external unidirectional magnetic field. The real part $\chi^{'}$ and the imaginary part $\chi^{''}$ of the complex susceptibility $\chi = \chi^{'} - j\chi^{''}$ is given by

$$\chi^{'} = \frac{1}{1 + (\omega\tau)^2} \chi_0 \tag{3.41}$$

and

$$\chi^{''} = \frac{\omega\tau}{1 + (\omega\tau)^2} \chi_0 \tag{3.42}$$

with χ_0 the equilibrium susceptibility. The susceptibility values (3.41) and (3.42) are directly related to the relaxation time constant τ.
The equilibrium susceptibility χ_0 , is based on the Langevin equation L:

$$\chi_0 = \chi_i \frac{3}{\xi} L(\xi);\ L(\xi) = \coth(\xi) - \frac{1}{\xi} \tag{3.43}$$

with

$$\xi = \frac{\mu_0 M_d H_0 V_c}{k_B T} \tag{3.44}$$

μ_0= $4\pi \times 10^{-7}$ $[m.kg.s^{-2}.A^{-2}]$ is the permeability of free space, M_d is domain magnetization of a suspended particle and V_c the volume of the magnetic core of the MNP.
The initial susceptibility χ_i equals

$$\chi_i = \frac{\mu_0 M_d^2 \Phi V_c}{3 k_B T} \tag{3.45}$$

with Φ the volume fraction, such that $M_s = \Phi M_d$ is the saturation magnetization of the ferrofluid. The domain of validity of the LRT is given by two conditions [96]:

$$\xi = \frac{\mu_0 M_d H_0 V_c}{k_B T} \ll 1 \tag{3.46}$$

and,

$$H_0 \ll \frac{2K}{\mu_0 M_d} \tag{3.47}$$

where K denotes the anisotropy constant of the magnetic core of the MNP. The first condition limits the amplitude of the applied magnetic field:,

$$H_0 \ll \frac{k_B T}{\mu_0 M_d} \frac{3}{4\pi R^3} \tag{3.48}$$

However, for magnetic fields and particles suitable for hyperthermia, the second condition is always fulfilled when the first one is (3.48). The first condition expresses that we are in the region where the response to an external field is linear.
Fig.3.6 shows a micromagnetic simulation on the basis of Vinamax [97] where a DC magnetic field is applied and the equilibrium magnetization is plotted as function of ξ in case of having randomly aligned particles (red curve). This is done for a magnetite particle (values of its characteristic material parametres are provided in Table 3.3) at a constant temperature of T=300 K and that is subject to a varying H_0 leading to a varying ξ.
The power loss per period of AMF, ΔU, is given by the following expression:

$$\Delta U = -\mu_0 \oint M dH = 2\mu_0 H_0^2 \chi'' \int_0^{\frac{\pi}{\omega}} \omega \sin^2(\omega t) dt \tag{3.49}$$

From (3.49), the power loss per unit time $P(W/m^3)$ is given as :

$$P = f\Delta U = \pi \mu_0 \chi_0 H_0^2 f \frac{2\pi f \tau}{(1 + (2\pi f \tau)^2)} \tag{3.50}$$

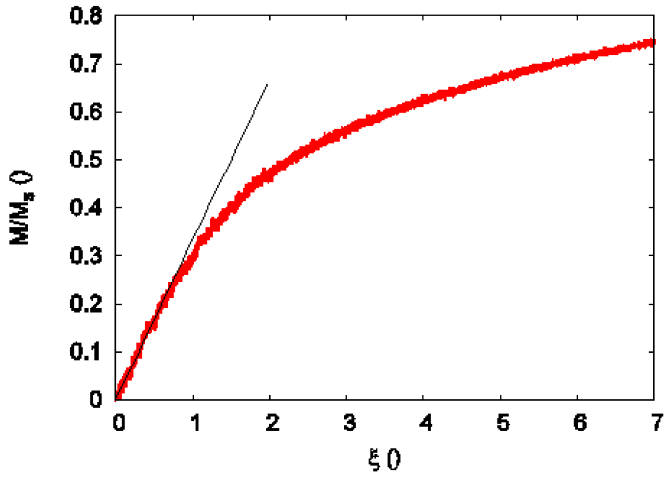

Figure 3.6: The equilibrium magnetization as function of ξ, the slope of this curve is the susceptibility and equals χ_0, denoted by the full black line, only when $\xi < 1$. The equilibrium magnetization is the magnetization obtained after a sufficient time when applying a DC field with value H_0, with $\xi = \frac{\mu_0 M_d V_c H_0}{k_b T}$.

The dissipated energy P depends on the characteristics of the AMF (amplitude H_0, frequency f) and the characteristics of the MNPs: radius R, anisotropy constant K and magnetization saturation M_d. Table 3.3 provides the values of the material characteristics of magnetite and maghemite. As we make the assumption that the MNPs are in the PMMA, we only consider the Néel relaxation $\tau = \tau_N$ from (3.37) within the power loss per unit time (3.49). As mentioned in 3.3.4.3 the length of time characteristic of the material τ_0 has a wide range (10^{-12} to 10^{-8} s) and is material and size dependent.

3.3.5.2 Size distribution of nanoparticles

Numerical simulations are performed to check the validity of the LRT. First, for different parameters (R, K, H_0 and f), then with fixed parameters of MNP (R=8 nm, K=10 kJ.m^{-1}, M=446 kA.m^{-1}). The specific loss power (SLP) as was defined for eddy current loss in (3.26), is here given by:

$$SLP[W/g_{\text{FeO}}] = \frac{P}{\rho_{FeO}} \tag{3.51}$$

where P is the power loss in [W.cm^{-3}] and $\rho_{FeO} = 5$ g.cm^{-3} is the mass density of the iron oxide.
The characteristics of the MNPs used in the simulations are presented in Table 3.3: For the numerical simulations, a lognormal radius r distribution for the MNPs is assumed, see (3.52).

MNP	M_d (kA.m^{-1})	K (kJ.m^{-3})	c_p (J.kg^{-1}.K^{-1})	ρ (kg.m^{-3})
γFe_2O_3	414	4.6	746	4600
Fe_3O_4	446	23-41	670	5180

Table 3.3: Physical properties of 2 types of magnetic nanoparticles; magnetite (Fe_3O_4) and maghemite ($\gamma - Fe_2O_3$)

$$p(r) = \frac{1}{\sqrt{2p}} \exp\left(-\frac{\ln^2(r/\mu)}{2\sigma^2}\right); \exp(x) = e^x \tag{3.52}$$

with μ and σ being the mean radius and standard deviation, respectively. Figure 3.7 depicts the lognormal distribution of particles (3.52) having different mean radii (μ = 6,7 and 8 nm) for a fixed standard deviation (σ=0.01).

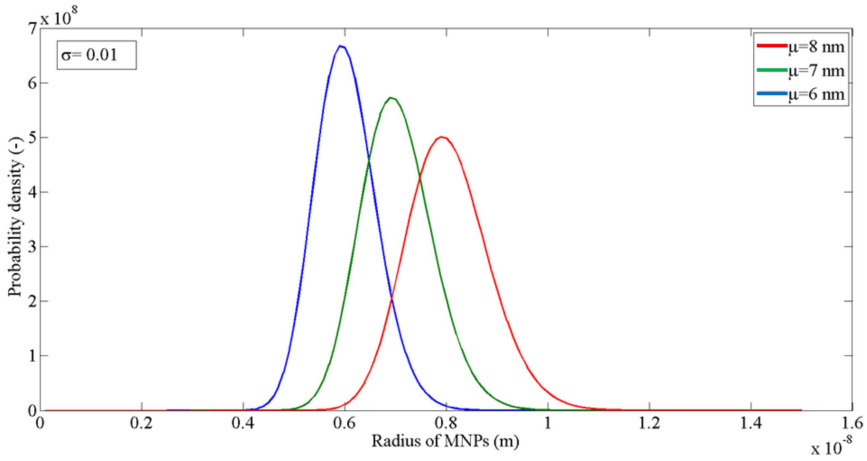

Figure 3.7: The MNPs distribution for standard deviation σ=0.01 and mean radius μ=6 nm (blue line), 7 nm (green line) and 8 nm (red line)

When considering a MNP sample with a wide size distribution, one thus has to be cautious whether LRT is suitable to predict the SLP or not; since the size of the particle affects through V_c the condition (3.45). However, such considerations are beyond the scope of this dissertation, as we focus on the impact of taking the size dependence of the length of time characteristic of the material τ_0 (from (3.37)) into account. As the value of τ_0 has an important effect on the SLP (3.50) and (3.49),

we will analyze its dependencies. When assuming that the LRT is valid, the SLP of a MNP sample following a lognormal size distribution can be expressed as follows:

$$SLP = \frac{\pi \mu_0 H_0^2 f}{\rho} \int \chi_0 \frac{\omega\tau(r)}{(1+(\omega\tau(r))^2)} p(r) dr \tag{3.53}$$

3.3.5.3 Magnetorelaxometry

Magnetorelaxometry is a method to characterize MNPs by measuring the decaying net magnetic moment of a MNP sample after it has been magnetized in an external field [98]. The decaying magnetic signal is described by

$$M(t) = M_0 \exp(-\frac{t}{\tau}); \exp(x) = e^x \tag{3.54}$$

where M_0 denotes the magnetization of the sample at t=0 and τ is the effective relaxation time constant given by (3.39). For immobilized MNPs only the Néel relaxation mechanism is relevant and consequently $\tau = \tau_N$. Since we wish to attain the effect of the typical relaxation time τ_0 used in the description of the Néel relaxation process, the Brownian relaxation phenomena is not considered.
As mentioned earlier, τ_0 is typically taken as a constant between 10^{-8} and 10^{-12} s. However, this quantity is size dependent (through V_c) as can be seen, derived by Brown, in the high barrier limit $KV_c \gg k_B T$ [97]:

$$\tau_0 = \frac{1+\alpha^2}{2\alpha\gamma} \sqrt{\frac{\pi k_B T {M_d}^2}{4K^3 V_c}} \tag{3.55}$$

where α is the Gilbert damping constant which accommodates for all loss mechanisms [99]. The damping constant α is related to τ_0. Using the macrospin simulation tool Vinamax, it is possible to simulate MRX experiments. Vinamax numerically solves the Landau–Lifshitz equation by adopting a dipole approximation method as described in Fig.3.8 where a collection of 10000 MNP is considered being either fixed in radius or MNP following a lognormal distribution.
The green symbols depict the relaxing signal of a sample consisting of MNPs with a fixed radius of 7 nm. The black curve shows a fit to this data with (3.54) allowing us to extract τ_N from these simulations. Because also the energy barrier and temperature are known, we can thus obtain τ_0 with the help of (3.38). Figure (3.7) also shows the effect that the lognormal distribution (collection of particles having mean value of 7 nm but with a certain standard deviation $\sigma = 0.1$) has on the relaxation signal compared to having MNP with fixed radius.
We first investigate the relation between τ_0 and α and their size dependence. With the help of Vinamax we simulated MRX signals for MNP samples with radius 5, 6, 7 and 8 nm for 17 different α values, logarithmically divided between 0.01 and 1. The results of these simulations are shown in Fig.3.9 as square dots.

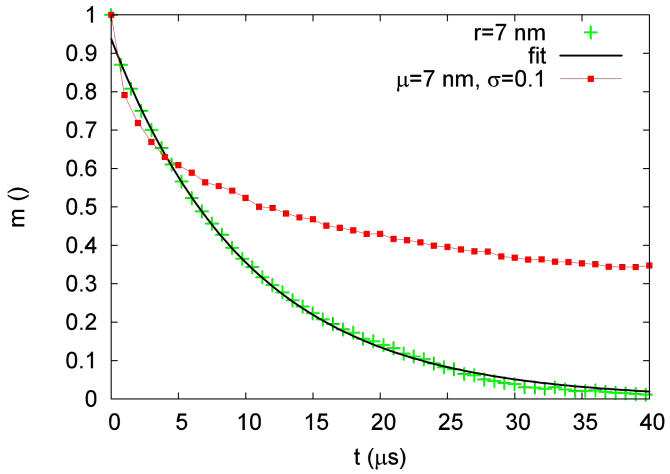

Figure 3.8: MRX simulation of 10000 MNPs with $\alpha = 0.01$ with fixed radius of 7 nm (green symbols) or lognormal size distribution (red line). The black line shows the closest fit of (3.54) to the data to extract τ_N from the simulation.

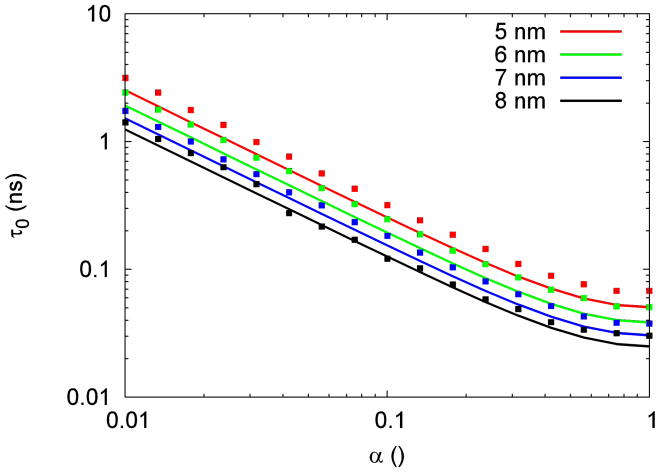

Figure 3.9: τ_0 as function of the damping parameter α using (3.55) and MRX simulations for different sizes.

The full lines depict the τ_0 expected from (3.55) and show that, although our data points lie 10 to 30% above the expected value, the dependence on α scales correctly. The differences between (3.55) and the numerical results originate in the fact that (3.55) has been derived specifically in the high barrier limit, corresponding to large MNPs. To verify that our results get increasingly closer to the theoretical expectation for larger particles, we performed additional simulations for

radii between 5 and 8 nm, in steps of 0.25 nm for α=0.01. The results of these simulations are shown in Fig.3.9 and indeed prove that the difference between the analytical and numerical results decreases for larger particles as the green line (that corresponds with (3.54)) comes closer to the red simulation points based on the Vinamax macrospin simulations. We incorporate this size-dependent deviation and fit the data points to an empirical correction function (blue line in Fig.3.9) resulting in the following corrected formulation for the τ_0:

$$\tau_0 = (1 + e^{-2.26.10^8 r}) \frac{1+\alpha^2}{2\alpha\gamma} \sqrt{\frac{p(r) k_B T {M_d}^2}{4K^3 V_c}} \tag{3.56}$$

We stress that the functional form of $(1 + \exp^{cr})$ with a constant c has no theoretical foundation but is found empirically to be close enough to our numerical data in the regime we are interested in to be a useful correction term such that we are able to use (3.55) outside of the high barrier limit. When considering MNPs having different magnetic material properties than those considered here, macrospin based simulations are again required to solve the correction. MRX measurements data acquired for a given MNPs ensemble can provide insights on the volume dependence of the τ_0.

Let us recall the MRX simulation of 10000 MNPs with α =0.01 with fixed radius of 7 nm (green symbols) or lognormal size distribution (red line). As can be observed, a sample following a lognormal size distribution has no longer an exponentially decaying signal (3.53) but needs to be described by the weighted sum of such functions:

$$M(t) = \int_0^\infty M_0 \exp(\frac{-t}{\tau_N(r)}) p\,(r)\, dr \tag{3.57}$$

Each lognormal distribution gives rise to a characteristic shape, which allows to experimentally recover the lognormal distribution of MNP samples from MRX data.

3.3.6 Size dependence of relaxation constant on SLP calculations

We now turn our attention to the effect on the SLP for a lognormal size distribution of MNP (3.53) where we incorporate the size dependance of τ_0 in the relaxation time constant in τ. To this end, we calculated the SLP, using LRT, for MNP ensembles with lognormal size distributions with μ ranging from 4 to 10 nm and σ ranging from 0.01 to 0.6 by means of (3.53) considering (3.56) and (3.38) with $\tau(r)$=$\tau_N(r)$. We consider 2 different α values (0.01 and 0.1) and we furthermore assume a magnetic field with $H_0 = 5$ kA/m and frequency $f = 200$ kHz. To allow an honest comparison between the results for a fixed τ_0 and the size dependent τ_0, we first performed our calculation with a size dependent τ_0 determined by (3.56),

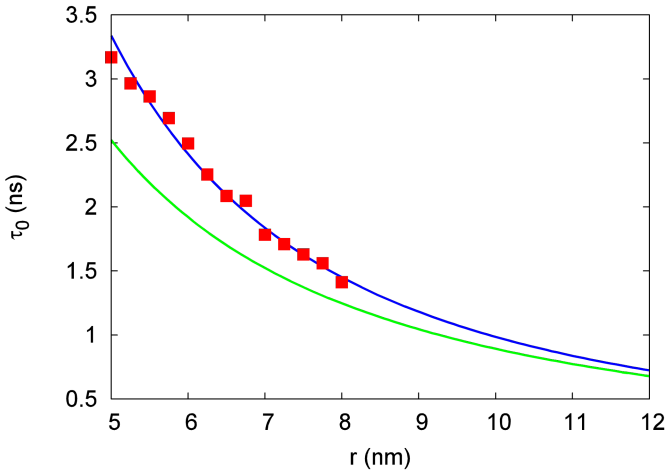

Figure 3.10: Dependence of τ_0 on the radius of the MNP for α=0.01 as extracted from micromagnetic simulations (red data points) and (3.55) (green line). The blue line is a closest fit to the data and corresponds to (3.55) multiplied with an empirical correction function, see (3.56).

and subsequently used τ_0 fixed to the value it had at the peak of the SLP, situated at $r \approx 6$ nm for α=0.01 and $r \approx 7$ nm for α=0.1. The results of these calculations are presented in Fig.3.11. We see that the SLP is higher for narrower size distributions and peaks at the sizes where the frequency and the relaxation time τ_N are each other's inverse. This also explains the shift of the peak towards smaller sizes for α=0.01 as compared to its location for α=0.1. A lower damping corresponds to slower relaxation mechanisms and thus a longer relaxation time. The optimal size corresponding to the ideal relaxation time, for the frequency we considered, is thus found at smaller particles.

When comparing the respective results with a fixed, or size dependent τ_0, we see no qualitative differences. Therefore we plotted the difference between both results (panels (c) and (f)). We notice a small tendency towards larger SLPs when we take the size dependence of τ_0 into account, which can amount to 10% of the SLP. However, as only MNPs with a size very close to the optimal volume contribute to the SLP, using a fixed τ_0 in one's calculations, provided that this value is well chosen, still gives a reliable estimate of the SLP in the light of other uncertainties involved in the MNP characteristics in hyperthermia experiments. Note however that in practice τ_0 is chosen between 10^{-8} and 10^{-12} s and using for example a value of 10^{-12} s in this case results in larger differences for the calculated SLP with this fixed τ_0 value and the calculated SLP taking the size dependency into account.

ΔSLP is the difference between the SLP calculated by means of (3.53) and the

SLP calculated by means of (3.51) with the assumed fixed τ_0 value. Results are depicted for three different σ values: 0.2, 0.1 and 0.01. Fig.3.12 shows for a fixed mean radius (in (a) for μ=6 nm, in (b) for μ=7 nm) the effect of assuming a certain fixed τ_0 on the corresponding SLP (i.e. SLP calculated by means of (3.51) with fixed τ_0) compared to the SLP calculated by means of (3.53) with the size dependent τ_0 determined by (3.56) for r=6 nm in (a) and r=7 nm in (b). This illustrates that there is a recommended value when using a fixed τ_0 depending on the magnetic material properties of the MNP and its size. One should use, depending on the sizes of the MNP, (3.55) or (3.56) to obtain a rough estimate of τ_0. This highlight the need for MRX measurements to extract the size dependency of τ_0.

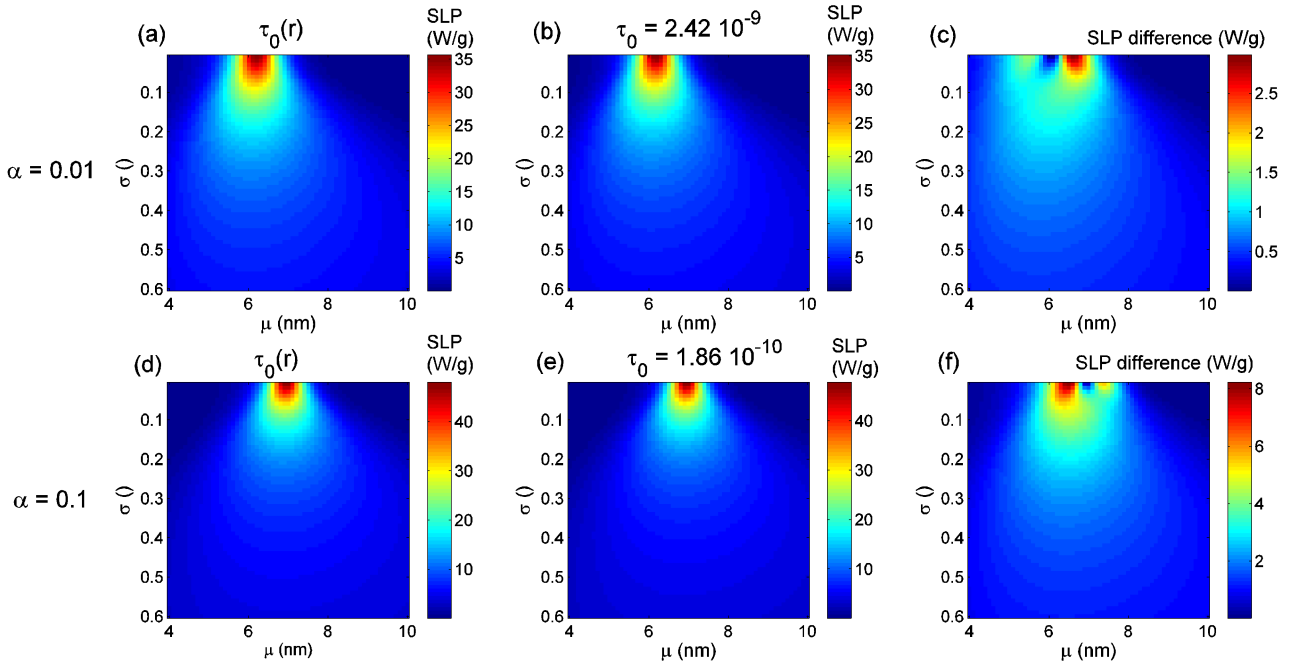

Figure 3.11: SLP as function of μ and α H_0=5 kA/m and f=200 kHz. (a) and (d) show the results for a size dependent τ_0 while (b) and (e) show the results for τ_0 fixed to the values indicated in the figure. (c) depicts the difference between (a) and (b) and (f) between (d) and (e). In panels (a)-(c) α equals 0.01 and in panels (d)-(f) α equals 0.1

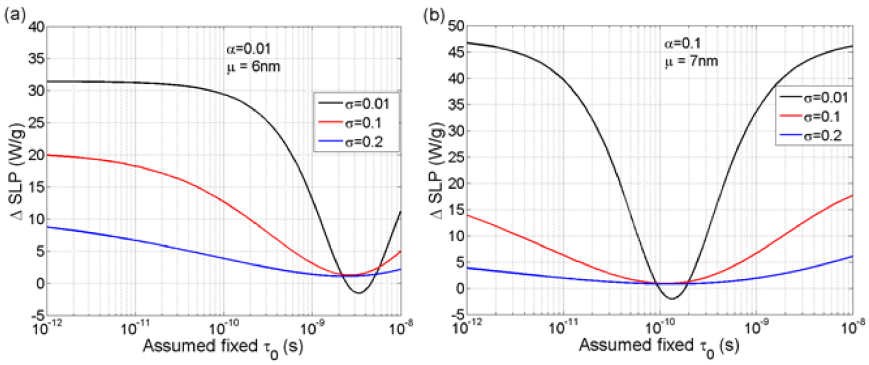

Figure 3.12: The effect of assuming a certain fixed τ_0 value on the corresponding SLP compared to the SLP calculated by means of size dependent τ_0 for H_0=5 kA/m and f=200 kHz. δ SLP is the difference between the SLP calculated by means of (3.56) with (3.53) and the SLP calculated by means of (3.56) with the assumed fixed τ_0 value. (a) is for the case of α=0.01 and μ=6 nm, while (b) is for α=0.1 and μ=7 nm.Results are depicted for three different α values.

3.4 Specific loss power measurements of PMMA+MNP and MRI compatibility

Since we need to maintain mechanical stability, the materials that give rise to heat need to be mixed with PMMA for the treatment of bone metastases. In this section we detail how the heating power of MNP can be experimentally assessed (subsection 3.4.1) and we discuss the MRI compatibility of PMMA+MNP mixtures (subsection 3.4.2).

3.4.1 Specific loss power measurements

3.4.1.1 Indicators for heating ability

In hyperthermia applications, the specific absorption rate (SAR) is a measure to indicate the heating power Q (W) generated per unit mass of MNPS when the magnetic nanoparticles are subjected to an AMF.

$$SAR = \frac{Q}{m_{\text{FeO}}} \tag{3.58}$$

Another name for the SAR is the Specific Loss Power SLP.
From practical point of use, the SLP may also be referred to the MNP mass. In that case the mass m_{FeO} in the equation above must be replaced by m_{MNP}. As the SAR is dependent on the properties of the MNP (material properties in Table 3.3 and the size as detailed in subsection 3.3.6) but also on the AMF (magnitude H_0 and frequency f), the intrinsic loss power (ILP) is introduced:

$$ILP = \frac{SLP}{f \cdot {H_0}^2} \tag{3.59}$$

which should be independent from the AMF according to the linear response theory in the case that χ" is not depending on the frequency ($Q \sim f{H_0}^2$). The SLP in (3.58) does not consider the concentration of particles themselves as these particles consist of iron oxide that give rise to heating but also of dextran and other types of coatings that do not result in the heating of the particles. SLP is the most accurate indication for heating of MNP since it is mass-normalized (specific) and denotes the magnitude that is being absorbed or released. SLP will be used in the next section to compare the heating of different samples: PMMA filled with powder or with fluid magnetic nanoparticles. As will be seen, the SLP is dependent on frequency, magnetic field strength, concentration and type of MNPs. A SLP of 100 W/g_{FeO} with typical iron concentration of $c_{Fe} = 5$ mg Fe / cm^3 corresponds thus with a total heating power of $Q_{\text{tot}} = 5 \cdot 10^5$ W/m^3. Experimentally measured SLP values for magnetic nanoparticles have been reported in literature [6] and was used in [100] to relate the SLP to the magnetic field amplitude H_0. A polynomial regression was made between measured SLP and applied magnetic fields, for instance for BNF-Starch particles (micromod Partikeltechnologie GmbH, Rostock, Germany) excited at a frequency of $f = 150$ kHz. This resulted in the following relationship, visually depicted in Fig.3.13:

$$\begin{aligned} SLP(H) = &-1.5207 \cdot 10^{-8}\, H^6 \,+\, 5.1705 \cdot 10^{-6}\, H^5 \,-\, 6.2314 \cdot 10^{-4}\, H^4 \\ &+\, 0.0299\, H^3 \,-\, 0.3746\, H^2 \,+\, 2.2897\, H \,-\, 4.0033 \end{aligned} \tag{3.60}$$

Because of the difficulties suffered in the modelling of the SLP using the linear response theory and micromagnetic Vinamax simulations, one can use experimentally measured SLP values that are close to the actual SLP generated by particles. SLP models as (3.60) are each time for a fixed frequency (i.e. fixed inductance and capacitor in the heating device) and including the frequency dependence is possible but requires extensive measurements.

3.4.1.2 Calorimetric method

The calorimetric approach is the most commonly used technique to evaluate the heat production of magnetic nanoparticles [101]. In this method, the MNPs are exposed to an alternating magnetic field and the temperature increase in the sample is recorded over a period of time. A fiber optic temperature probe is typically used in conjunction with a magnetic induction heating system consisting of a water cooled coil connected to a power supply. Samples are placed in a thermally

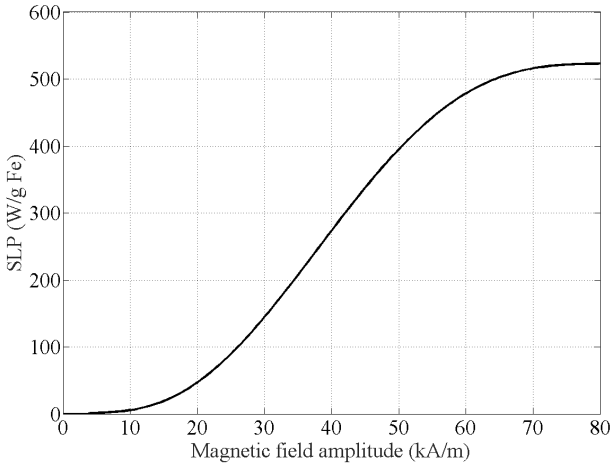

Figure 3.13: SLP as function of magnetic field amplitude for BNF Starch magnetic nanoparticles on the basis of experimental values [6] with polynomial regression (3.60).

insulated container to avoid heat loss to the environment to assert having an adiabatic measurement. Nevertheless, it is challenging to keep the sample in strict adiabatic conditions due to conduction and convection heat exchanges with the environment [102]. Therefore, most of the SLP experiments are considered as semi-adiabatic calorimeter setups, where heat exchange corrections must be made [103]. Figure 3.14 shows schematically the temperature increase as a function of time in a sample consisting of MNPs when having adiabatic and non-adiabatic conditions. In non-adiabatic conditions at a certain moment there could be equilibrium in the heat transfer (i.e. the $\frac{dT}{dt} \approx 0$), or equivalently the heat produced equals the heat going to the environment.

To perform non-adiabatic SLP experiments, first the sample needs to be put at room temperature before starting the experiment. The sample in the container is placed inside the excitation coil to perform the measurements. The room temperature value is kept in track throughout the entire measurement. We start the experiment by recording the temperature evolution from the initial point t_0 during X_0 minutes (e.g. $X_0 = t_1 - t_0 = 5$ min) to a stable temperature T_1 (see Fig.3.15). Then we switch on the inductor-capacitor circuit to have an AMF and we continue recording the temperature as function of time for a period $t_2 - t_1$ after which we reach temperature T_2. Finally, the AMF is switched off and the system cools down naturally to temperature T_1 during $X_1 = t_3 - t_2$. After recording temperature T_1 the temperature evolution is kept acquiring for X_2 (no less than 30 s) after which the experiment is stopped. The slope of the temperature versus time curve can be determined using several manners eg. initial slope method, corrected slope

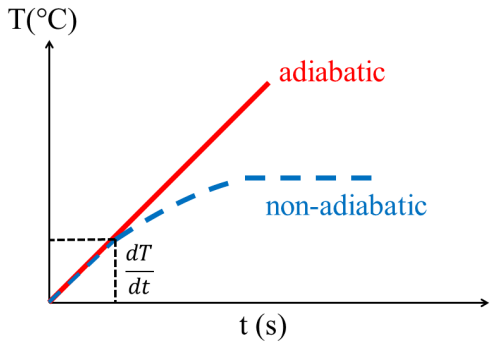

Figure 3.14: Temporature increase of samples temperature in adiabatic (red line) and non-adiabatic (blue dotted line) calorimeter setups

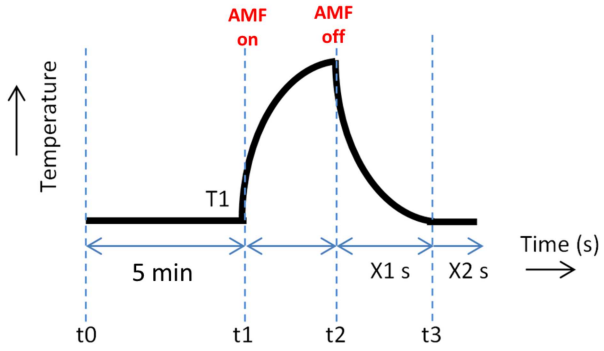

Figure 3.15: Scheme of experimental SLP measurement using the calorimetric method

method, Box-Lucas, etc [101].
The SLP is calculated from the temperature derivative over time at instant $t = t_1$ using (3.61):

$$SLP = \frac{C}{m_{\text{MNP}}} \frac{dT}{dt}|_{t=t_1} \tag{3.61}$$

where C is the heat capacity of the insulated container and its content, m_{MNP} is the mass of the magnetic material, and $\frac{dT}{dt}$ is the initial slope of the change in temperature versus time curve.

3.4.1.3 Heat generation of PMMA+MNP samples

Using a measurement setup, constructed at the department, we assess the SLP arising from a ferrofluid and from PMMA+MNP.
A ferrofluid consist of magnetic nanoparticles that are suspended in water. We performed experiments on a suspension having a concentration of 29 mg/ml. A glass vial containing a volume of 0.97 ml of the suspension is placed in the center of the 8-turns helical coil. The coil has a radius of 28 mm and is cooled with a closed circulating water system.

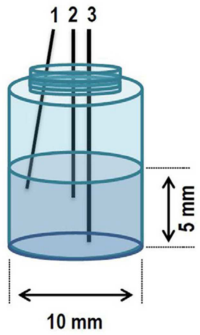

Figure 3.16: Schematic of the vial containing the ferrofluid. Sensor 1 and 2 are placed at the top of the sample while sensor 3 is positioned near the bottom of the vial.

The increase in temperature of the whole suspension is measured using 3 optical sensors: Sensor 1 and 2 are placed at the top of the sample while sensor 3 is positioned in the bottom of the vial as shown in Fig.3.16.
Figure 3.17 depicts the temperature increase in the ferrofluid sample at the top of the fluid (sensor 1 and 2) and at the bottom of the vial (sensor 3). Since the variation of temperature given by the 3 sensors is almost the same, we assume that the nanoparticles are spread homogeneously in the fluid and subjected to an uniform magnetic field giving rise to a uniform temperature increase in the vial.
Since we consider a suspension consisting of various components (water, MNP and container) having different specific heat capacity and mass, (3.62) needs to be adapted so that it weights the different components that give rise to the measured SLP:

$$SLP = \frac{c_{p,\text{fluid}} m_{\text{fluid}} + c_{p,\text{MNP}} m_{\text{MNP}} + c_{p,\text{container}} m_{\text{container}}}{m_{\text{MNP}}} \frac{dT}{dt}|_{t=t_1} \tag{3.62}$$

Since the temperature variation of the container at $t = t_1$ is negligible and the heat capacity of the MNP is very small compared to the heat capacity of the fluid, (3.62) can be written as follows:

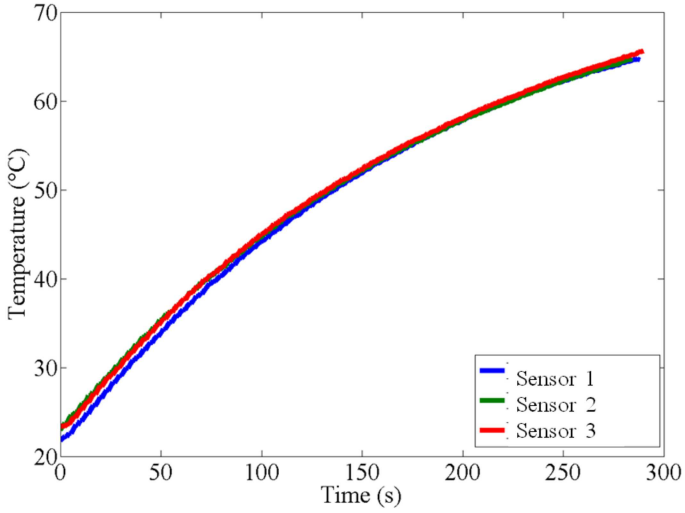

Figure 3.17: Temperature increase of ferrofluid sample under a magnetic field H=14,78 kA/m and a frequency f=321 kHz. The measurements are done in 3 different points: sensor 1 (red line) and sensor 2 (green line) are in the top of vial. Sensor 3 (blue line) is at the bottom of the vial.

Table 3.4: Specific loss power values (W/g_{FeO})

Sensor	**H (kA/m)**	**f (kHz)**	**SLP** W/g_{FeO}
1	14.78	321	43.29
2	14.78	321	40.43
3	14.78	321	41.33

$$SLP \approx \frac{c_{p_{\text{water}}} m_{\text{water}}}{m_{\text{MNP}}} \frac{dT}{dt}|_{t=t_1} \tag{3.63}$$

Notice that this approximation (equation (3.63)) is only valid for a homogeneous mixture of MNPs in the fluid. This approach is not valid any more for the case of a PMMA+MNPs sample in water. Some results on the ferrofluid measurements are given in Table (3.5).

PMMA+MNP samples are prepared by mixing VertaPlex^{TM} radiopaque bone cement (manufactured by $Stryker$) and 2 brands of magnetic nanoparticles: Ferrotec EMG (Serie 1500) and Micromod-Bionized NanoFerrite particles. Ferrotec EMG (Serie 1500) dry iron oxide nanoparticles have a nominal diameter of 10 nm.

Table 3.5: Considered sample types and iron oxide concentrations (conc).

N	**state**	**core type**	**conc (wt$\%$)**
1	Fluid	Multicore	0.068
2	Fluid	Multicore	0.034
3	Fluid	Multicore	0.007
4	Fluid	Multicore	0.003
5	Powder	Multicore	0.677
6	Powder	Multicore	0.068
7	Powder	Multicore	0.034
8	Powder	Multicore	0.007

The core material of these MNP is principally magnetite (Fe_3O_4). They are single domain and superparamagnetic nanoparticles with an initial magnetic susceptibility of χ_i= 0.2. The proportions by weight are 71.8 to 79.2% of iron oxide and 28.1 to 20.8% of surfactant. Micromod-Bionized NanoFerrite nanoparticles (BNF particles) have a particle diameter of 80 nm with a core of 75-80 (w/w) magnetite and a shell of dextran. It consists of 54.8% iron oxide, namely 13.7 mg iron oxide/25 mg powder. The above described MNPs brands will be referred to as single core and multicore particles, respectively. PMMA+MNP samples were considered as listed in Table 3.5. 4 samples contained multicore ferrofluid, 4 samples multicore powder with different iron oxide concentrations. Higher concentrations of the multicore fluid led to unstable PMMA-MNPs mixtures. We would like to stress that the purpose here is to investigate certain aspects of different properties of magnetic nanoparticles, rather than to show the superiority of one MNP brand compared to another. The tabulated concentrations in weight percentage (wt$\%$) are calculated as the mass fraction of iron in the complete solution. For example, sample type 2 is a mixture of *VertaPlexTM* radiopaque bone cement, consisting of 2000 mg powder and 1 ml liquid that vaporises during polymerization, with 0.05 ml multicore ferrofluid. This ferrofluid has a mass density of 25 mg/ml containing 13.7 mg/ml iron. Consequently, this results in an iron oxide concentration of $100 \times (13.7 \times 0.05)/(2000 + 25 \times 0.05)$ equal to 0.0340 wt$\%$.

The PMMA+MNP sample was immersed in a cylindrical water container and placed in the center of the helical 8-turns coil with I=100 A is applied with a resonance frequency f_r=400 kHz. The temperature increase is measured using 2 optical temperature sensors T_1 and T_2 to average the heat variation of the water. In order to obtain a standard measurement method that can provide reproducible results, we apply the AMF when having a constant temperature in water during 15 min before switching on the AMF. The AMF is switched off after $t_2 - t_1$=60 min whereas the temperature measurements are maintained until the water reaches

room temperature. The results in Fig.3.18 display the difference ΔT between the room temperature and the maximum temperature reached after one hour of AMF heating. Under a current I of 100 A and a frequency f=400 kHz, samples made of multicore fluid (red triangles) have a higher temperature increase than the powder samples (blue squares). The figure also shows the positive effect of the iron oxyde concentration on the temperature increase. Both for fluid and powder multicore samples, a temperature increase of at least 6°C is reached which is necessary for hyperthermia treatment as the tumor area is heated up starting from the body temperature 37°C to 43-45°C. Where the temperature increase exceeded the maximum desired 8°C, the applied high current and frequency can be lowered to fit into the 6-8°C interval.

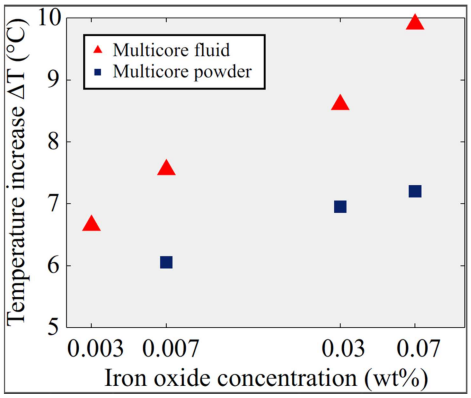

Figure 3.18: Temperature increase (ΔT) of multicore samples with different MNP (powder and ferrofluid) concentrations under AMF of $I = 100A$ and $f = 400kHz$ (calculated H=25 kA/m) after 60 min.

When considering the above SLP measurements, one should take into account the uncertainties related to materials and thermodynamic reasons ranging from non-adiabatic heat losses to inaccurate material concentrations. First, the use of non-adiabatic experimental set-up results in peripheral heating due to radiant heat flux from the heating coils. Also, materials inaccuracies such as the MNPs concentrations and the homogeneity of the PMMA mixture affect the temperature increase. Similarly, the spatial variation of the probe location leads to an uncertainty for stable samples in the cylindrical holder. All those reasons lead to errors in measurements which can explain an overestimation of the SLP values.

3.4.2 Magnetic resonance imaging disturbance of PMMA+MNP

In this subsection we analyze the disturbance of the magnetic nanoparticles on magnetic resonance images. For the same reasons as those mentioned in a similar study performed in section 3.2.3.

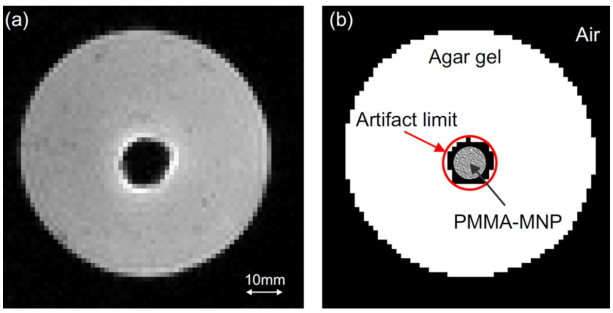

Figure 3.19: (a) Original MRI slice of the agar gel phantom containing a PMMA+MNP sample (Ferrotec-liquid 0.6 ml). (b) Masked image in which the different materials are indicated. The disturbed area is surrounded by a red ellipse defining the artifact limit.

3.4.2.1 Quantification of MRI artifacts

To quantify the MRI artifacts caused by the magnetic nanoparticles, we place PMMA+MNP samples in the middle of an agar gel phantom. The phantoms were cylindrical with a diameter of 55 mm is a state of use imaging modality for monitoring the response of bone metastases to treatments [104]. After cooling, the phantoms became solid. The next day they were measured with a Siemens Trio TIM 3T MR scanner 3T MR scanner. The cylindrical phantoms were turned on their side such that their length was aligned with the main magnetic DC field of the MR scanner. This way similar transversal slices, as shown in Fig.3.19 a, could be obtained. T_1-weighted images were acquired from the phantoms using an MP-RAGE sequence (repetition time = 2250 ms, echo time = 4.18 ms, flip angle = 9 degrees, field of view $256\times256\times176$ mm^3 and voxel size $1\times1\times1$ mm^3). This sequence was chosen, since T1-weighted MRI is a state of use imaging modality for monitoring the response of bone metastases to treatments [105]. For every MRI session, between 17 and 21 slices were selected centralized around the half length of the sample. As illustrated in Fig.3.19 b, the artifact caused by the magnetic nanoparticles was measured in each slice by fitting an ellipse to the disturbed area and subtracting the radius of the sample (4.5 mm) from the average of the major and minor ellipse radii. As a tool for the fitting, the images were masked with a threshold of 30% of their maximal value. Since each phantom was measured twice, this procedure led to a total of 34-42 values, indicating the spread of the artifact, for each MNP concentration.

Table 3.6: Considered sample types and iron oxide concentrations (conc). used in MRI

no	state	core type	conc (wt%)
1	Fluid	Multicore	0.340
2	Fluid	Multicore	0.068
3	Fluid	Multicore	0.034
4	Fluid	Multicore	0.007
5	Fluid	Multicore	0.003
6	Powder	Multicore	0.677
7	Powder	Multicore	0.340
8	Powder	Multicore	0.068
9	Powder	Multicore	0.034
10	Powder	Multicore	0.007
11	Powder	Single core	1.829
12	Powder	Single core	0.926
13	Powder	Single core	0.466
14	Powder	Single core	0.224
15	Powder*	Single core	0.595
16	Powder*	Single core	0.299
17	Powder*	Single core	0.156
18	Powder*	Single core	0.078
19	Powder*	Single core	0.039

In total 19 different PMMA+MNP samples were considered as listed in Table 3.6. 5 samples contained multicore ferrofluid, 5 samples multicore powder and 9 samples single core powder, all with different iron oxide concentrations. Since we noticed the arising of clusters in the single core powder, 5/9 of the samples were made with the clustered powder (indicated with * in the table) and 4/9 of the samples were mixed with the same powder that was moulded fine.

Even though we aspired high accuracy by using micro pipettes and a micro-balance for selecting the small amounts of particles, we are aware of the fact that the listed concentrations (Table 3.5) are subject to fluctuations. Throughout the length of the cylindrical PMMA+MNP sample a variation in iron concentration is possible, certainly for the clustered multicore powder. To account for this, we have chosen to display the distribution of MRI artifacts as boxplots. Despite the careful preparation of homogeneous agar gels, small air bubble were present in a few agar gel phantoms, complicating the measurement of MRI artifacts due to the MNP.

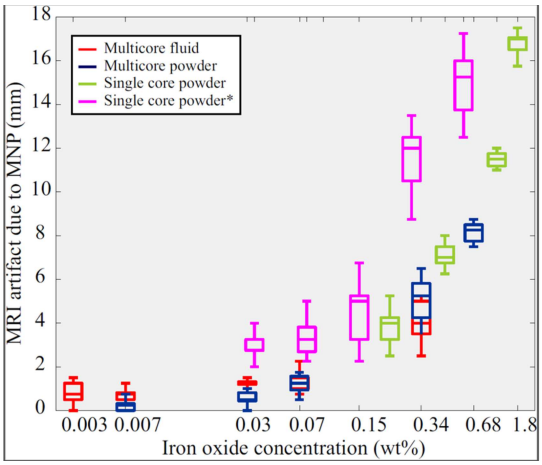

Figure 3.20: Magnetic nanoparticles are causing artifacts in MRI with increasing concentration. The measurements of artifact spread are visualized using boxplots. The central line is the median, the edges of the box are the lower (Q1) and upper quartile (Q3) and the whiskers extend to extreme data points not considered outliers. The outliers are defined to be smaller than Q1 - 1.5(Q3-Q1) or larger than Q3 + 1.5(Q3-Q1) and not plotted here. The MNP concentrations are plotted on a logarithmic scale (log10).

Figure 3.20 depicts boxplots of the measured artifact as function of iron oxide concentrations for the four types of samples. The relation between both is approximately linear. The multicore samples give rise to lower MRI artifacts compared to single core samples containing similar iron oxide concentrations. For example, single core clustered powder with concentrations of 0.039 and 0.078 wt% disturb the MRI with 4 and 7 mm on average, while for both multicore fluid and powder with concentrations 0.034 and 0.068 wt% this is only 0.5 and 1.25 mm, respectively. Even the minimum artifacts caused by single core clustered powder are equal or higher than the maximum caused by multicore samples. There is no significant difference in MRI quality for different states of matter. Both the multicore samples prepared with ferrofluid and with powder disturbed the images equally. By pounding the clustered single core MNP, they could be more homogeneously mixed with the PMMA. This led to a lower variation in the artifact values between the slices as can be seen by smaller interquartile ranges. These results demonstrate that both concentration and type of MNP affect the MRI compatibility of PMMA+MNP samples.The samples prepared with multicore MNP up to an iron concentration of 0.07 wt% gave rise to smaller artifact values.

This study investigated the artifacts MNP caused in the MP-RAGE sequence. The effect on other sequences besides this T1-weighted gradient echo sequence are still unknown. T2-weighted, diffusion-weighted and short τ inversion recovery (STIR) sequences or T1-weighted spin echo sequences are advised for imaging

bone metastases as well [105] and could be studied in the future.

3.5 Conclusion

This chapter detailed the heat generation in materials that are subject to an alternating magnetic field. We considered two types of materials: non-magnetic and magnetic materials. In Section 3.2 we detailed the eddy current loss that non-magnetic conducting materials generate when they are placed in an AMF. We ultimately derived a specific loss power (W per gram non-magnetic conducting material) due to eddy currents that is function of the properties (electrical conductivity, radius, mass density) of the non-magnetic material and the applied field (amplitude and frequency). For Titanium and Carbon non-magnetic materials, that are also used in other implant applications, limited specific loss power values were obtained. We also analyzed the effect that these particles have on the quality of magnetic resonance images where we concluded that the non-magnetic particles' concentration needs to be low to have limited artifacts. Moreover we also observed experimentally, in accordance to the theory of eddy current loss, that the temperature increase with samples consisting of a mixture of PMMA with MNP remains limited and not sufficient for bone metastases hyperthermia treatment.
We subsequently addressed in Section 3.3 the physical mechanisms that give rise to heat when having magnetic materials subject to an AMF. We detailed the various physical principles of magnetism and namely that the magnetization state of a magnetic material depends on the minimization of the Gibb's free energy. We also addressed the loss mechanisms in magnetic materials and specifically for magnetic nanoparticles the main source of loss is due to Néel and Brownian relaxation loss since hysteresis loss and eddy current loss are limited when having particles smaller than 100 nm. Néel and Brownian relaxation can be characterized by the relaxation constant that characterizes the time constant at which the magnetization of a magnetic nanoparticle approaches an equilibrium state. We sketched the linear response theory to address the dependency of the specific loss power due to Néel and Brownian relaxation of magnetic nanoparticles on the properties of the MNP (saturation magnetization, anisotropy constant, specific heat capacity, mass density) and the AMF (amplitude and frequency). We stressed the domain of validity of the LRT as well as the size dependence of the relaxation constant. Since a collection of MNP always follow a certain distribution, mostly that is a lognormal distribution, this has an effect on relaxation time constant. By making comparison of the linear response theory with micromagnetic simulations that are based on macrospin approximations, we concluded that a correction of the length of time characteristic of the material is required. We also concluded that using magnetorelaxometry measurement data it is possible to recover this characteristic length of time and include this together with the correction factor to predict the specific loss

power due to Néel and Brownian relaxation. This work allowed us to get insights into the heat generation in magnetic nanoparticles but since assumptions are made for the simulation of the specific loss power due to Néel and Brownian relaxation, experimental characterization is key.
Experimental work in the form of specific loss power measurements and MRI compatibility was performed in Section 3.4 specifically for PMMA mixed with MNP as we aim at treating bone metastases (PMMA provides the mechanical stability of the spine). Specific loss power measurements were performed using the calorimetric method that also contains uncertainties with respect to correct assessment of the specific loss power since the measurements are difficult to achieve in adiabatic conditions. We showed the temperature increase that can be achieved with PMMA mixed with MNP (only Néel relaxation because of fixed MNP in the PMMA) and compared this with ferrofluids (Néel and Brownian relaxation). Since PMMA+MNP only has Néel relaxation the specific loss power was relatively lower but nevertheless we could achieve even with relatively low concentration of MNP a temperature increase of at least 6-8 °C that is needed for hyperthermia treatment. We also experimentally investigated the effect of MNP on the quality of magnetic resonance images. Both the concentration and type of MNP affect the MRI compatibility of PMMA mixed with MNP. Single core clustered powder resulted, for similar concentrations, in higher artifacts compared to multicore MNP. We showed that having multicore powder having an iron oxide concentration of 0.07 wt% in the PMMA+MNP, resulted in artifacts that are less than 2mm and that gave rise to a temperature increase of 7°C which is sufficient for hyperthermia treatment of bone metastases. This resulted in a proper protocol for the material preparation (PMMA+MNP) of magnetic hyperthermia.

4

Thermal and damage analysis of biological tissue

‘Those diseases that medicines do not cure are cured by the knife. Those that the knife does not cure are cured by fire. Those that fire does not cure must be considered incurable’

Hippocrates
Aphorism 87

4.1 Introduction

An optimized magnetic hyperthermia treatment should selectively destroy the tumor cells without damaging the surrounding healthy tissue. When comparing the results of clinical trials, the need for a proper thermal dose parameter is evident. But to decide what is the most appropriate thermal dose is less obvious. Therefore, the development of thermal models for the prediction of the heat diffusion in biological tissue is necessary to define the required thermal dose. This chapter explains methods used to quantify the thermal injury and models to study the heat diffusion in the surrounding of vertebrae starting from the Pennes bio-heat equation.

4.2 Heat transfer in biological tissues

In this section we provide the fundamentals of heat transfer and how heat transfer in biological tissue can be mathematically modelled. By means of these models, it is possible to perform simulations of the temperature both spatially and temporally for a given heat source arising from the interaction of the particles in the PMMA with the AMF. The heat source was extensively studied in Chapter 3.

4.2.1 Heat transfer

4.2.1.1 Heat transfer principles

Heat transfer is the energy that transits due to temperature differences in the form of conduction, convection, and/or radiation. These principles can be used to model the temperature behavior in hyperthermia:

- Conduction is heat transfer resulting from the diffusion of energy where energy is transferred from the more energetic to the less energetic particles of a substance or material. In its core, conduction is related to molecular activity where interactions between molecules make diffusion of heat possible. In general, good conductors of electricity e.g. metals like copper, aluminum, gold are also good heat conductors.

- Convection is due to the bulk or macroscopic motion of convective medium, such as gas or fluid, e.g. the heat transfer when cooling a plate due to moving cold air on the surface of the plate. The energy transfer is a superposition of energy transfer due to random motion of particles as well as due to bulk motion of the fluid. In the modeling of convection, distinction can be made between forced convective heat transfer where a fluid is forced to flow along a solid surface by a pump (related to the bulk motion of a fluid); and natural or free convection where heat transfer occurs even if the fluid is not forced (related to the random motion of particles).

- Radiation is the transfer of energy that is emitted by a matter having a certain temperature such as the transport of heat from the sun to the earth. Heat transfer results from the emission of energy via electromagnetic waves or photons. This type of energy transfer is only relevant for high temperature values.

We consider heat transfer modelling related to conduction and convection without radiation as only moderate temperature values are present.

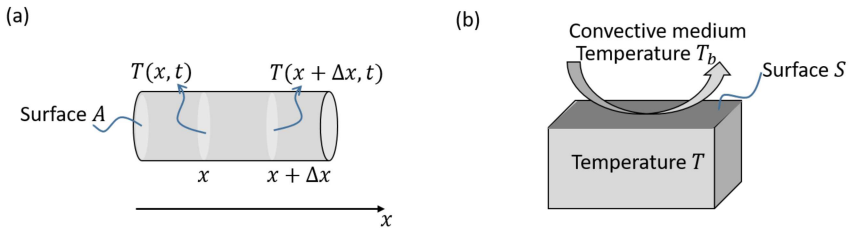

Figure 4.1: (a) Fourier's law of heat conduction in 1D, (b) Newton's law of cooling through convection.

4.2.1.2 Heat transfer modelling of conduction and convection

Let $T(\mathbf{r}, t)$ denote the temperature at a certain position $\mathbf{r}$ and at a given time t. For clarity, we omit using the $\mathbf{r}$ and t in the forthcoming notations. The amount of heat or thermal energy E expressed in Joules in a volume V is proportional to both the mass m and the temperature T:

$$E = c_p m T \tag{4.1}$$

where c_p is the specific heat capacity expressed in $\frac{J}{kgK}$. The local thermal energy density expressed in $\frac{J}{m^3}$ is defined as:

$$e = E/V = c_p \rho T \tag{4.2}$$

with ρ being the mass density in $[\frac{kg}{m^3}]$. This equation is based on considering the rate of heat transfer Q expressed in $W = \frac{J}{s}$

$$Q = \frac{dE}{dt} \tag{4.3}$$

When considering in Fig.4.1 the following one-dimensional example where we have a material at two different points x and $x+\Delta x$ (with Δx the distance between the two points) being at a temperature of $T(x, t)$ and $T(x + \Delta x, t)$ respectively, the rate of heat transfer Q equals

$$Q = kA\frac{T(x, t) – T(x + \Delta x, t)}{\Delta x} \tag{4.4}$$

A is the cross-sectional area normal to the direction of the heat flow (in m^2). k is the thermal conductivity in $\frac{W}{mK}$. The law in (4.4) is based on experimental observations by Fourier. This law expresses that the rate of heat transfer across a surface should be proportional to the surface area A and the temperature difference (T(x,t) – T(x + Δx, t)) per distance Δx. In the limit for Δx going to zero, (4.4) can be written as

$$Q = -kA\frac{dT}{dx} \tag{4.5}$$

with the minus sign indicating that heat will flow from regions of high temperature to regions of low temperature. The thermal conductivity k in Fourier's law of heat conduction (4.5) is a measure of the material's ability to transfer or "conduct" heat. Note that often heat flux density q is used to express the rate of heat transfer per unit surface across A : $q = Q/A$. The conductive heat flux density vector becomes:

$$\mathbf{q} = -k\frac{dT}{dx}\mathbf{1}_x \tag{4.6}$$

and is expressed in $[\frac{W}{m^2}]$. In case of Fourier's law of a 3D heat flux density (4.6) becomes:

$$\mathbf{q} = -k\nabla(T) \tag{4.7}$$

As mentioned in 4.2.1.1, next to conduction, convection needs to be considered as basic principle in the heat transfer modelling. Newton's cooling law expresses the rate of heat transfer due to temperature differences between the convective medium at a temperature T_b and the surface of the solid material at a temperature T, see Fig.4.1(b):

$$Q = c_{\text{conv}}S(T - T_b) \tag{4.8}$$

with c_{conv} the convective heat transfer coefficient in $\frac{W}{m^2K}$ and S is the surface of the material with the convective medium. Newton's law of cooling (4.8) is as Fourier's law based on experimental observations where c_{conv} depends on characteristics of the convective medium such as the flow velocity, fluid properties, etc. Note that the convective heat flux density vector is expressed as

$$\mathbf{q} = c_{\text{conv}}(T - T_b)\mathbf{n} \tag{4.9}$$

also in $\frac{W}{m^2}$ as the conductive heat flux density vector and $\mathbf{n}$ is unit vector ortogonal to the surface S of the volume.

4.2.2 Pennes' bioheat equation

Pennes' bioheat equation can be derived by considering the conservation of energy: changes of thermal energy in a volume V of biological tissue are due to heat sources and heat sinks within the biological tissue as well as heat flux coming in or leaving the surface S of the volume [106]. The energy balance can be considered in e.g. an arbitrary volume as in Fig.4.1(a) and results in the following equation:

$$\frac{d}{dt}\int_V edV = -\oint_S \mathbf{q}\cdot\mathbf{n}dS + \int_V fdV \tag{4.10}$$

with e the thermal energy density (4.2), $\mathbf{q}$ the heat flux (cfr. the conductive heat flux in (4.6)), the outward normal vector perpendicular to the surface S and f representing the heat sources ($f > 0$) and heat sinks ($f < 0$) in $\frac{W}{m^3}$. For now, we do not consider convective heat flux (4.9) as no convection at the surface is

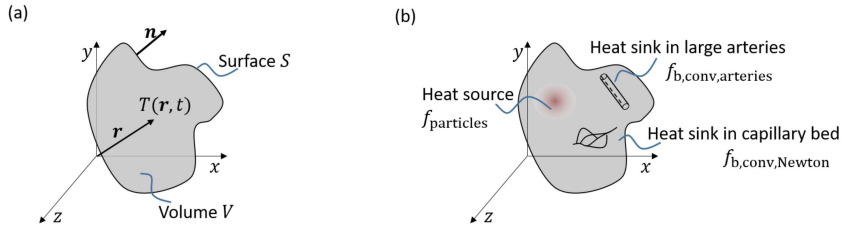

Figure 4.2: (a) Arbitrary volume V with surface S where the energy balance can be described leading to a temperature distribution $T(\mathbf{r}, t)$. The normal vector $\mathbf{n}$ on the surface is also depicted. (b) Conceptual representation of convection heat sinks in the capillary bed due to Newton's cooling law, convection heat sinks in large arteries and heat sources due to the use of heat particles.

assumed in the Pennes' bioheat equation but where convection occurs within the volume as heat sink, e.g the blood perfusion within the volume that draws heat from the considered biological tissue.
Inserting the thermal energy density (4.2) and the heat flux expressions we can rewrite (4.10) as

$$\int_V c_p \rho \frac{dT}{dt} dV = \oint_S k \nabla T \cdot \mathbf{n} dS + \int_V f dV \tag{4.11}$$

assuming that c_p and ρ are constant in time. By using the divergence theorem, (4.11) can be rewritten as

$$\int_V c_p \rho \frac{dT}{dt} dV = \int_V \nabla \cdot (k \nabla T) dV + \int_V f dV \tag{4.12}$$

As mentioned earlier, convection is generally included in the Pennes' bioheat equation as a heat sink proportional to $-(T - T_b)$. Specifically for convection due to blood perfusion, the heat sink can be represented by

$$f_{\text{b,conv,Newton}} = -\omega_b \rho_b c_b (T - T_b) \tag{4.13}$$

with ω_b the blood perfusion rate, ρ_b the blood mass density and c_b is the specific heat capacity of blood. Convection (4.13) typically occurs in the capillary bed of biological tissue. Large arteries can however not be modelled by Newton's cooling law as in (4.13) and require a different heat sink formulation:

$$f_{\text{b,conv,arteries}} = -\rho_b c_b \mathbf{v} \cdot \nabla T \tag{4.14}$$

with $\mathbf{v}$ being the blood velocity vector. From this equation it is clear that heat sink occurs where the blood velocity vector has a component parallel to the temperature gradient. Heat sources f can be due to metabolic mechanisms, but that can

be neglected when considering a sufficiently large heat source stemming from particles interacting with an AMF. The specific loss power SLP of particles ($\frac{W}{g_{FeO}}$), see equation (3.61), is related to the source f in $\frac{W}{m^3}$ by the mean mass density of particles ρ_{FeO} (in $\frac{kg}{m^3}$) :

$$f_{\text{particles}} = \rho_{FeO} \cdot SLP \tag{4.15}$$

In Fig.4.2(b), the previously described heat sources and heat sinks in a certain volume V are schematically depicted. Let us now include in the conservation of energy equation (4.12) the conduction, the heat sinks due to convection of heat in the capillary bed of the biological tissue (4.13), the convection of heat at large arteries (4.14) as well as the heat source due to particles interacting with the AMF (4.15):

$$\int_V c_p \rho \frac{dT}{dt} dV = \int_V \nabla \cdot (k \nabla T) dV + \int_V (f_{\text{b,conv,Newton}} + f_{\text{b,conv,arteries}} + f_{\text{particles}}) dV \tag{4.16}$$

Since (4.16) is valid for each volume V, we can rewrite this as the following equation where we need to solve towards the temperature T:

$$c_p \rho \frac{dT}{dt} = \nabla \cdot (k \nabla T) + (f_{\text{b,conv,Newton}} + f_{\text{b,conv,arteries}} + f_{\text{particles}}) \tag{4.17}$$

or

$$c_p \rho \frac{dT}{dt} = \nabla \cdot (k \nabla T) - \omega_b \rho_b c_b (T - T_b) - \rho_b c_b \mathbf{v} \cdot \nabla T + f_{\text{particles}} \tag{4.18}$$

The latter equation is the general Pennes' bioheat equation that mathematically models the heat transfer in biological tissue when having hyperthermia with heat sources $f_{\text{particles}}$. Solving this equation allows to find the temperature at a certain position $\mathbf{r}$ and time t within a given volume. The temperature behavior depends on the heat source, the geometry of the volume, but also on the thermal properties of the biological tissue within the volume such as specific heat capacity c_p, conduction coefficient k, convective properties of blood in the capillary bed $\omega_b \rho_b c_b$ and along large arteries with specifically the velocity $\mathbf{v}$. For solving (4.18), initial values of the temperature such as the temperature in the volume at a certain starting point ($t = 0$) is the body temperature $T(\mathbf{r} \in V, t = 0) = 37°C$ (Dirichlet boundary condition) and boundary conditions such as Neumann boundary conditions $\nabla T(\mathbf{r} \in S, t) \cdot \mathbf{n} = 0$. The latter stems with letting the temperature free at a perfect thermal isolating the surface S contrary to the Dirichlet boundary condition that fixes the temperature value.

4.3 Damage models of elevated temperature to biological tissues

As mentioned in section 1.3.1, elevated temperatures in biological tissues cause cytotoxic effects in the cells. The thermal damage depends upon both temperature and exposure time at temperature. Several damage models have been introduced in scientific literature: the Arrhenius damage model and the CEM43 damage model detailed in the following subsection 4.3.1 and the CEM43 damage model, detailed in 4.3.2.

4.3.1 Arrhenius damage model

In-vitro studies of mammalian cells in culture that were exposed to elevated temperatures have demonstrated that the cytotoxic effect follow an Arrhenius relationship [107] [108]. The Arrhenius damage model assumes that the survival fraction follows a kinetic model including a state energy barrier with an irreversible molecular flux, as in the Arrhenius model used to model kinetic transitions in chemical transitions. Fig.4.3 depicts the transition from healthy cell to damaged cell where an energy barrier needs to be overcome. It also shows that the transition is irreversible. The Arrhenius damage index $\Omega(\mathbf{r}, t)$ ($0 \leq \Omega < +\infty$) that is space ($\mathbf{r}$) and time (t) dependent due to exposing the biological tissue to elevated temperatures, is mathematically modelled by the following differential equation [108], [107]:

$$\frac{\partial \Omega(\mathbf{r}, t)}{\partial t} = 0, T \leq 43^{\circ}C$$

$$\frac{\partial \Omega(\mathbf{r}, t)}{\partial t} = A \exp(-\frac{\Delta E_a}{R\,(T(\mathbf{r}, t) + 273)}), T > 43^{\circ}C \tag{4.19}$$

A is the frequency factor that can be associated to how many cells per second cross the energy barrier. ΔE_a is the activation energy barrier that is related to the energy barrier that needs to be overcome to have a transition from healthy to damaged cell. $R = 8.314\ \frac{J}{\text{mol}\,C}$ is the universal gas constant. In Table 4.1, literature values for the frequency factor A and the activation energy barrier ΔE_a are reported. Note that in (4.19) the Arrhenius damage index Ω does not vary when having temperature values lower than 43°C, i.e. in this damage model it is assumed that having no sufficient temperature elevations does not result in biological damage. When having temperatures that rise higher than 43°C results in a change of the Arrhenius damage index as this damage model allows to cross the energy barrier more easier to move from living cells to damaged cells.

Table 4.1: Constants A, ΔE_a from literature for calculating the damage index with the Arrhenius damage model (4.19).

	Tumor [109]	**Tumor [110]**	**Healthy tissue [110]**
$A(s^{-1})$	$2.984\,10^{80}$	$1.8\,10^{36}$	$1.03\,10^{38}$
ΔE_a (J/mol)	$5.064\,10^{5}$	$2.38\,10^{5}$	$2.49\,10^{5}$

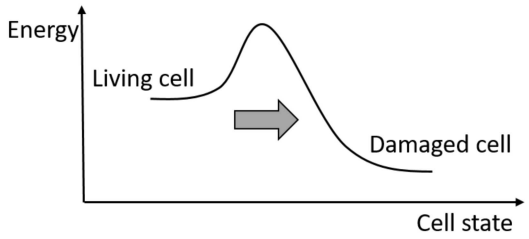

Figure 4.3: Schematic representation of the Arrhenius model used to capture thermal damage where a certain energy barrier needs to be overcome so to damage healthy cell and have an irreversible change of the cell.

Based on the damage index $\Omega(\mathbf{r}, t)$ the survival fraction of cells ($0 < \alpha \leq 1$) undergoing elevated temperatures can be calculated as [111]:

$$\alpha(\mathbf{r}, t) = \exp(-\Omega(\mathbf{r}, t)) \tag{4.20}$$

The survival fraction (4.20) can be interpreted as the ratio of the concentration of living cells at the chosen end-point and the initial concentration of living cells (e.g. start of the hyperthermia). The initial concentration of living cells is $\alpha(\mathbf{r}, t = 0) = 1$ when the hyperthermia starts (at t=0) and gradually decreases when having temperatures larger than 43°C where the rate of decrease in survival fraction is driven by (4.19). Based on the above, the damaged fraction of cells δ ($0 \leq \delta < 1$) can then be calculated as

$$\delta(\mathbf{r}, t) = 1 - \alpha(\mathbf{r}, t) \tag{4.21}$$

The damage index (4.19) and survival fraction (4.20) have been intensively used to assess the efficacy of hyperthermia and thermotherapy in general: e.g. in [109] for assessing the efficacy of radiofrequency ablation of liver, in e.g. [111], [108] for evaluating hyperthermia. In Fig.4.4, the damage index Ω from (4.19) is calculated for the Arrhenius damage model parameters reported in Table 4.1 for a constant temperature of 46°C. The corresponding survival fraction of cells α calculated with (4.20) is shown in Fig.4.5. It is clear from these figures that the values for the frequency factor A and activation energy barrier Δ_{E_a} in the Arrhenius model have an important impact on the damage index and survival fraction. As can be

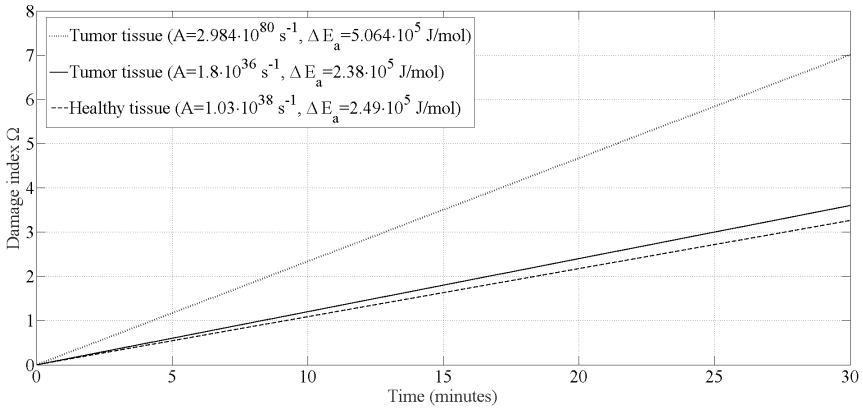

Figure 4.4: Evolution of the damage index when having biological tissue exposed to a constant temperature of $46°C$ for frequency factor and activation energy barrier values as given in Table 4.19.

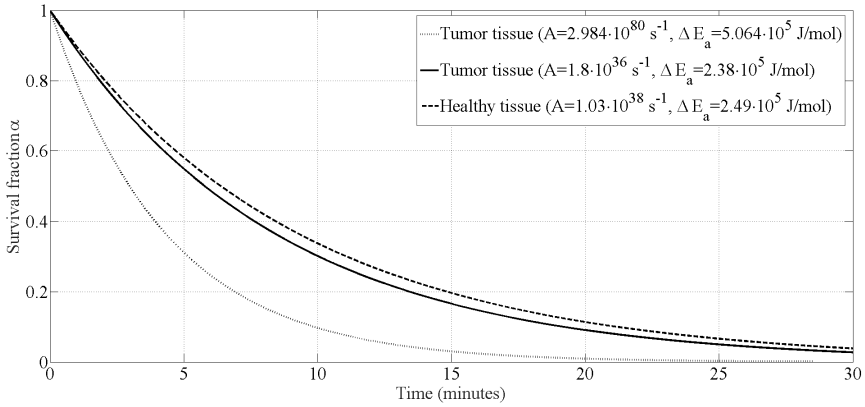

Figure 4.5: Evolution of the survival fraction when having biological tissue exposed to a constant temperature of $46°C$ for frequency factor and activation energy barrier values as given in Table 4.19.

observed from Fig.4.5, a survival fraction of living cells being 0.1 is achieved after 10 minutes using the values from [109] whereas approximately 20 minutes are needed when using the values from [110]. The difference between the tumor and the healthy tissue remains however limited when using the values from [110].

4.3.2 CEM43 damage model

The cumulative equivalent minutes at $43°C$, shortly CEM43, is defined based on the total isoeffect thermal dose achieved when inflicting a certain elevated temper-

ature to tissue. The CEM43 thermal dose is mathematically expressed as [112]:

$$CEM43(\mathbf{r},t) = \int_0^{t_\mathrm{f}} K^{\frac{43^\circ C - T(\mathbf{r},\mathbf{t})}{1^\circ C}} dt \tag{4.22}$$

with K being a constant of proportionality with value 0.5 for $T > 43^\circ C$ and value 0.25 for $T \leq 43^\circ C$. t_f is the total exposure time. Expression (4.22) is mainly used in preclinical studies as metric for assessing the thermal dosage inflicted to tumors when having the tissue at a certain temperature and exposure time. It was shown in [113] that achieving a $CEM43 \geq 60$ minutes resulted in an effective hyperthermia treatment. Note that in this damage model, there is damage when having temperature lower than 43°C but that the associated damage remains limited because of the lower constant of proportionality K. When inspecting (4.22) it is clear that when having a constant temperature of 43°C and a total exposure time $t_f = 60$ minutes that this results in a $CEM43 = 60$ minutes. When having a temperature of 44°C for 60 minutes, then this results in a $CEM43 = 120$ minutes.

4.3.3 Limitations of damage models

CEM43 and Arrhenius model are widely used to predict cell death during hyperthermia procedure. However, both models hold a number of weaknesses and have considerable limitations. As enlightened in [108], CEM43 and Arrhenius models predict the decay of the survival fraction by describing only a single constant irreversible reaction of the total thermal damage. Nonetheless, the cell death process is more complex including thermotolerance and cell recovery phenomena [114]. In addition, the models are based on *in vitro* observations of idealized cell culture experiments where cells are growing in uniform Petri dishes with constant and appropriate conditions e.g. low cell density and enough nutrients in the medium, whereas the tumor environment is characterized by heterogeneous conditions.
Table 4.2 gives the required duration t_f of the hyperthermia treatment at a constant temperature T_r in order to be effective, i.e. $CEM43$=3600 s. On the other hand, the damage index Ω, defined in the Arrhenius damage model, during t_f seconds heating at a constant temperature T_r is given by

$$\Omega = t_f A e^{-\frac{\Delta E}{R(T_r+273)}} \tag{4.23}$$

Taking into account (4.23), Table 4.2 shows the corresponding Ω values after the duration of t_f seconds required for an effective hyperthermia treatment according to the $CEM43$ model and considering the Arrhenius constants from Table (4.1). Notice that the obtained values for the damage index Ω are in the range of 0.23 to 2.94, which corresponds with a survival fraction α between 0.795 and 0.053. Consequently, there is a non negligable discrepancy between the two damage models.

Table 4.2: Required heating duration t_f at constant temperature T_r in order to obtain a CEM43 value of 60 minutes and corresponding Ω values

T_r (C)	t_f (s)	Ω, Tumor [109]	Ω, Tumor [110]	Ω, Healty tissue [110]
43	3600	2.09	2.94	2.56
44	1800	1.92	1.96	1.72
45	900	1.76	1.30	1.16
46	450	1.60	0.86	0.78
47	225	1.45	0.57	0.53
48	112.5	1.31	0.38	0.35
49	56.25	1.19	0.25	0.23

4.4 Thermal and damage 3D simulation model

Based on the theoretical framework of heat transfer from section 4.2 we describe in this section a specific model to evaluate three-dimensionally the thermal distribution in a vertebra subject to magnetic nanoparticle hyperthermia. Based on the damage models from section 4.3 we will furthermore analyse the damage inflicted to the tissue. The objective of simulations is to judge the effectiveness of different scenarios before the MNH session to aid in selection of the specific power needed and clinical outcome prediction. In addition, simulations are helpful for assessing treatment risks to the patient, e.g. avoiding the spinal cord damage or analysing treatment quality. In our study, we follow the following three distinct steps::

- Generation of the model detailed in section 4.4.1.
- Calculation of the temperature distribution due to power deposited in the tissue, section 4.4.2.
- Calculation of the resulting damage distribution in the tissue, section 4.4.3.

4.4.1 3D modeling of the biological tissue

The complex shape of a vertebra is simplified to a cylindrical geometry as shown in Fig.4.6. An inner cylinder of PMMA-MNP mixture is surrounded by the tumor volume placed in the center of the vertebral body. Potential heat drain by the aorta and the inferior vena cava is simulated with use of the two cylinders, on the left and right of the vertebral body (see Fig.4.6). The blood flow is simulated by enforcing a temperature of 37°C at the boundary of the aorta and vena. The complete geometry with spinal cord, aorta and vena is placed in a cylinder with the same properties as muscles tissue. In section 4.4.1 and 4.4.2, the tumor radius is considered to be 8 mm and the muscle tissue has a radius of 40 mm, which is large enough to avoid influence of the border temperature on the tumor temperature. Dimensions and

properties of vertebra, spinal cord, aorta and vena were found in literature [9] and given in Tables 4.3 and 4.4. Once the simulation conditions and parameters are defined, the temperature distribution and damage can be analyzed by solving the equations presented in Section 4.2.2 using the finite element method. By discretizing the geometry in finite elements using meshing, it is possible to numerically calculate the heat transfer within the presented geometry. To each finite element material properties are associated depending on their geometrical location (being bone, tumor, muscle, spinal cord, blood, PMMA).

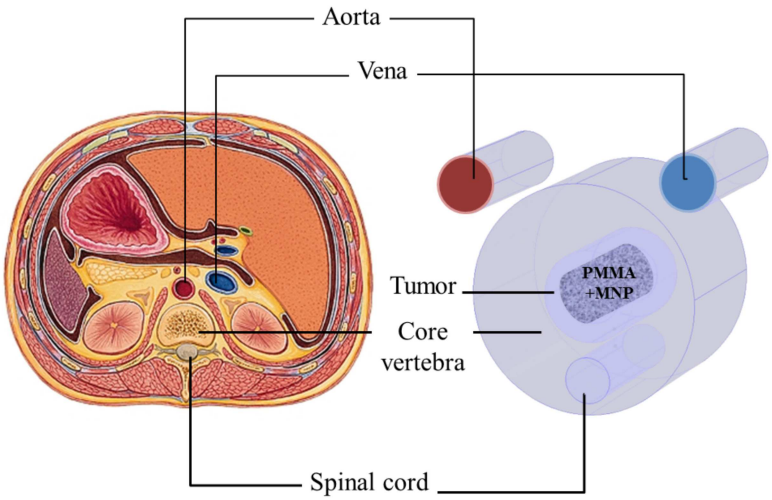

Figure 4.6: Cross section of the body showing the shape of a vertebra (left). The vertebra is simplified to a cylindrical geometry including an inner cylinder of PMMA-MNP mixture surrounded by the tumor volume placed in the center of vertebral body (right).

Tissue parameters like density, specific heat capacity and thermal conductivity are reported in Table 4.3 and have been assumed constant which is an approximation keeping in mind the very small temperature variation from 37°C till 47°C [115]. In actual practice, human physiology is so complex that even relatively small increases in the tissue temperature may lead to effects such as altered production of hormones, suppressed immune response, and protein denaturization.

4.4.2 Temperature distribution during MNH

Temperature predictions during MNH is a defying task. This is due to large uncertainties in the thermal properties of tissue, which vary between patients, within

Table 4.3: Parameters of the considered biological tissues [9]

Tissue	c_p (J/kg.K)	ρ (kg/m^3)	k (W/m.K)
Bone	1313	1908	0.32
Tumor	3760	1045	0.51
Muscle	3421	1090	0.49
Spinal cord	3630	1075	0.51
Blood	3770	1060	0.51
PMMA	1420	1180	0.19

the patient and within each tissue (see Table 4.3). Thus, an accurate 3D prediction of the thermal tissue properties is a challenge. Therefore thermal simulations are performed in order to obtain a qualitative insight in the different phenomena.

Table 4.4: Dimensions and positions of the considered biological tissues. All tissues are modeled with cylindrical shape having the axial direction along the z-axis.

Tissue	r (m)	l (m)	Point of gravity (x,y,z)
PMMA+MNP	0.005	0.02	(0,0,0)
Tumor	0.008	0.024	(0,0,0)
Bone	0.02	0.03	(0,0,0)
Muscle	0.04	0.03	(0,0,0)
Spinal cord	0.03	0.03	(0,- 0.014,0)
Aorta/Vena	0.005	0.03	(-/+ 0.02,0.02,0)

4.4.2.1 Spatial variation of temperature

In our model, the heating source is implemented as a PMMA cylinder in the center of the tumor region. Dimensions and positions of the different regions forming the 3D model are presented in Table 4.4. The heat transfer characteristics were obtained by varying the magnetic heat generation term Q(W) while keeping other parameters constant. The idea is to consider the PMMA volume as a heat source assuming a uniform nanoparticle distribution and homogeneous thermal properties throughout the region. We initially apply a constant heat source in order to increase the temperature at the outer boundary of the tumor from 37 °C to 47 °C. Then a cyclic heat generation is applied by switching on and off the power source in order to keep a temperature average between T=45°C and T=47°C, again at the outer boundary of the tumor, during the whole MNH procedure. The total calculation time was set to 3600 seconds. In Fig.4.7, the 3D and 2D distribution of the tem-

perature is shown for heating power equal to Q=3 W. Additionally, the variation of the temperature is depicted in 2 particular points in the xy-plane (Fig.4.7): the first point ('Tumor' point, henceforth denoted as T_{tumor}) at the outer radius of the tumor and nearest to the spinal cord, and the second point ('Spinal cord' point, denoted as $T_{\text{spinal cord}}$) at the boundary of the spinal cord and nearest to the heat source.

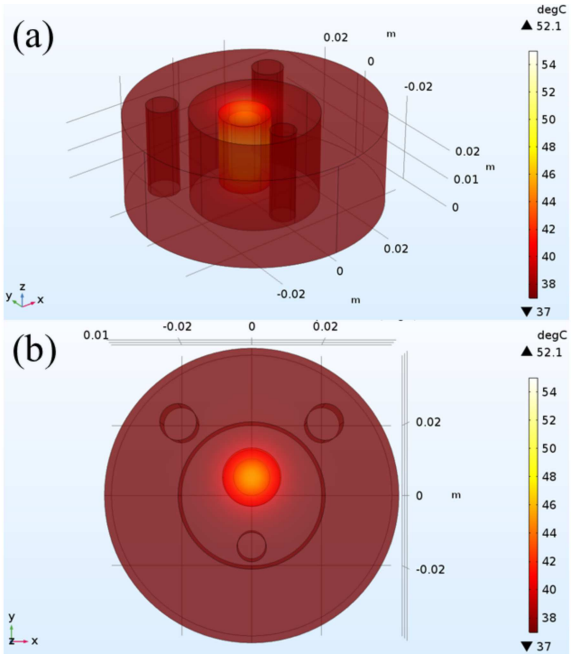

Figure 4.7: Temperature distribution in vertebra when applying heat source Q=3 W in (a) 3D view of the complete geometry (b) 2D view in the xy-plane

Fig.4.8 shows that it is possible to keep the temperature of the spinal cord under 38°C while heating the tumor region at 47°C during one hour which avoid the risk of damage in the spinal cord. We can observe here the cyclic nature of the temperature at the outer surface of the tumor due to switching on and off the power. We would like to stress that in our model we consider the worst case with respect to the heating of the spinal cord as the Cerebrospinal Fluid (CSF) is not included in the geometry. In fact, the cerebrospinal fluid has three main functions: CSF protects brain and spinal cord from trauma, supplies nutrients to nervous system tissue and removes waste products from cerebral metabolism [116]. In the case of hyperthermia for bone metastases, the CSF acts as temperature barrier by moving away the heat and keeping the spinal cord safe.

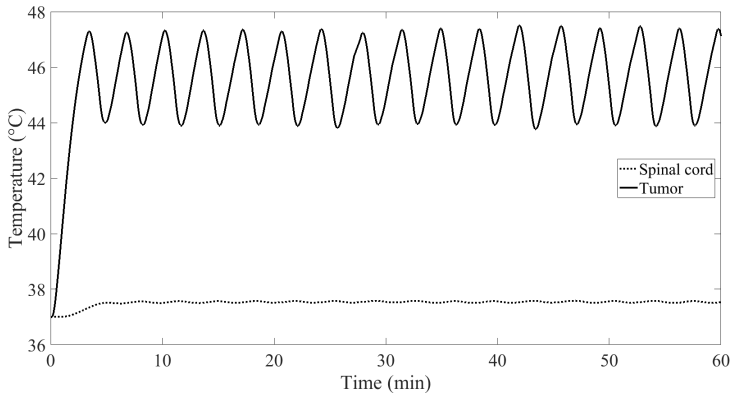

Figure 4.8: Time variation of the temperature at the outer surface of the tumor and the nearest surface of the spinal cord after 1 hour under heat source Q=3 W.

4.4.2.2 Temperature distribution as function of heat power

The minimum amount of heat needed to reach 47°C in the tumor region is estimated by applying various values of heat sources Q. For that we noticed that a minimum heat power Q=3 W is needed to reach temperature of 47°C in the outer radius of the tumor region. Fig.4.9 shows the time variation of the temperature during 100 s for power sources from 3 to 10 W. The level of applied heat power affects the temperature variation of the tissue. Higher applied power to the tissue leads to a shorter time needed to reach 47 °C. The highest temperatures reached after 100 s vary from 42.9°C to 51.8°C (see Fig.4.9). The difference of temperature has been 2°C even with only 1 W difference for heat sources below 6 W. The difference of temperature between each two neighboring power levels decreases from lower power to higher power.

Another interesting feature is the fact that, during the first seconds, the heating rate is faster in the tumor than outside eg. the spinal cord. Indeed, this is due to the time required for heat diffusion through the neighboring tissues. This is illustrated in Fig. 4.10 and Fig. 4.11 for 3 and 6 W respectively. The spatial temperature distribution at 100 s is for instance larger in the tumor than for 300 s and the opposite can be observed within the spinal cord. Both for the Q=3 W and Q=6 W case. Having the ratio $T_{\text{tumor}}/T_{\text{spinal cord}}$ larger after 100 s of treatment than in the switching on and off regime may be advantageous with respect to cancer treatment. If a large amount of nanoparticles is administered (larger value for the power Q), the temperature rises very fast inside the tumor during the first seconds and the exposure time may be adjusted in such a way that the surrounding tissue remains at moderate temperatures. However, as a consequence of the high initial heating rate, the exposure time has to be adjusted very carefully. Therefore,

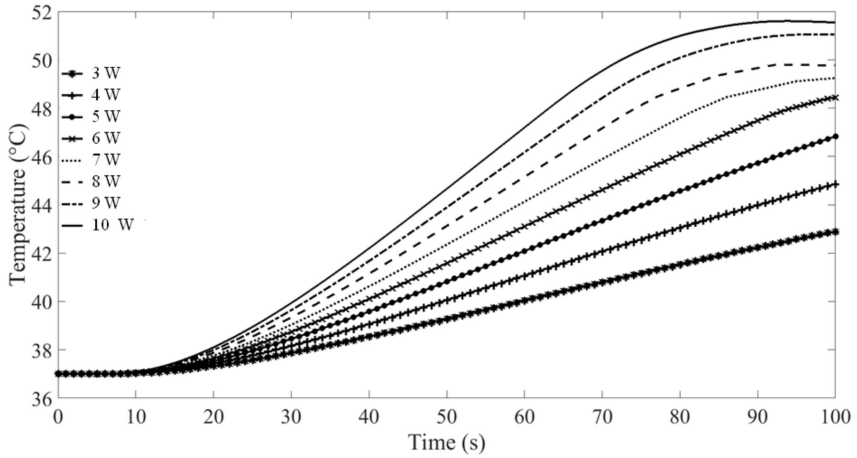

Figure 4.9: Time variation of the temperature at the outer surface of the tumor for various values of the heat source Q during the first 100 seconds of continous heating.

another strategy may consist in an accurate choice of administered MNP mass using a rather long exposure time. This mode offers the possibility of a large time tolerance but accepts a less pronounced temperature difference between tumor and environment.

4.4.3 Damage during MNH

Based on the damage models from Section 4.3 and the spatio-temporal temperature distributions, we calculate the damage of the biological tissue and discuss its implications with respect to MNH for bone metastases.

4.4.3.1 Damage distribution as function of heat power

The measure of tissue damage accumulated over hyperthermia procedure is computed using the same model described in 4.4.1, particulary the values in Tables 4.3 and 4.4. The Arrhenius model, presented previously, is used to predict the resulting thermal damage of the tissue. The Arrhenius fraction of necrotic tissue can be interpreted as the ratio of damaged cells to total cells inside a region of space, cfr. (4.21). Initially, the fraction of necrotic tissue is equal to 0, the tissue is considered completely viable. Fig.4.12 depicts the temporal variation of the necrotic fraction

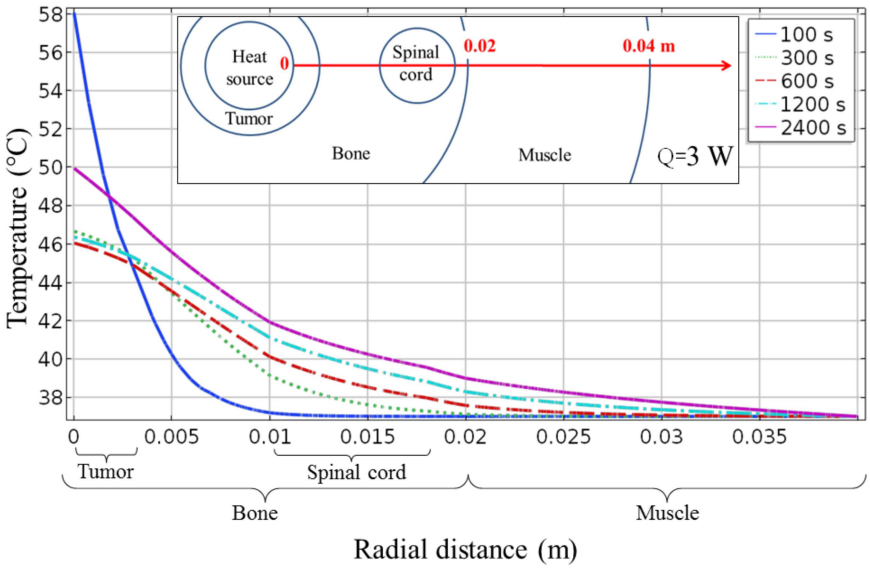

Figure 4.10: Temperature variation after exposure times t=100, 300, 600, 1200 and 2400 s, along the radial axis in the xy plane and z=0.015 m starting from the outer surface of heat sources equal to Q=3 W, throughout the whole tumor region then the bone and the spinal cord ending with the muscle.

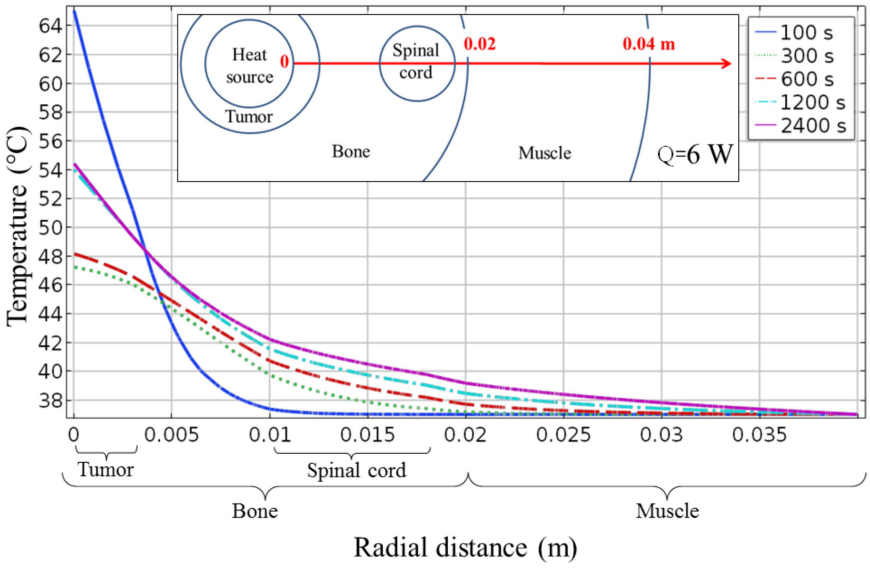

Figure 4.11: Temperature variation after exposure times t=100, 300, 600, 1200 and 2400 s, along the radial axis in the xy plane and z=0.015 m starting from the outer surface of heat sources equal to Q=6 W, throughout the whole tumor region then the bone and the spinal cord ending with the muscle.

at the outer surface of the tumor (previously denoted as T_{tumor}) having frequency factor A=1.8 10^{36} 1/s and activation energy barrier ΔE_a=2.38 10^5 J/mol (see expression 4.19) when applying a heat source Q=3 W during t_f=60 minutes. Notice that we switch on and off the heat source when reaching a temperature of 45°C respectively, 47°C at the outer region of the tumor. It is shown that after applying this heat source, the value of δ approachs 1 (i.e. biological tissues are damaged) can be reached within 1 hour. For Q=3 W, 80% of tumor cells are damaged after 15 minutes and the remaining 20% of tumor cells require a heating of 45 minutes. The small ripple that can be noticed on the time evolution of the necrotic fraction is due to the cyclic nature of the temperature (Fig. 4.8) due to the on and off switching of the power. .

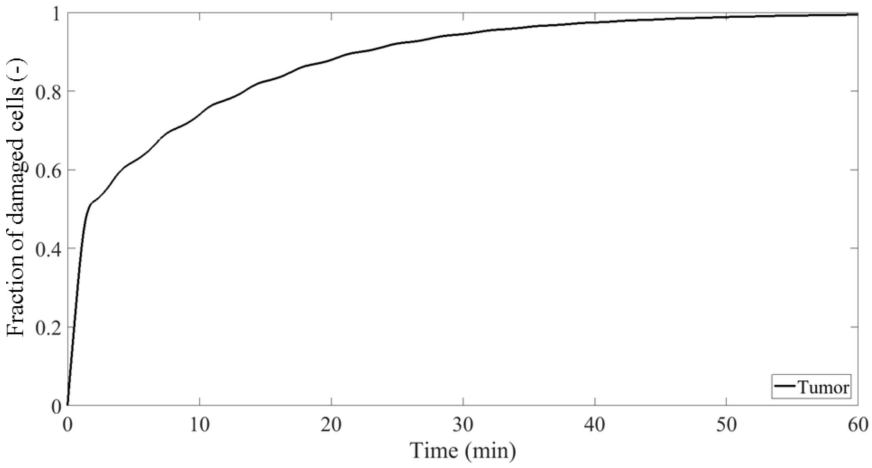

Figure 4.12: Time variation of the necrotic fraction in tumor having frequency factor A=1.8 10^{36} 1/s and activation energy barrier ΔE_a=2.38 10^5 J/mol when applying a heat source Q=3 W during 60 minutes

4.4.3.2 Effect of the spatial variation of the tumor region on the damage

In this section we investigate the effect of the tumor volume on the efficacy of the hyperthermia treatment. We therefore perform a numerical analysis starting from the thermal model of section 4.4.1 taking into account the values of Tables 4.3 and 4.4, however modifying the radii of the tumor and the PMMA regions. Again

we apply the switch on and off strategy in order to obtain temperature variation at the outer boundary of the tumor region between 45 and 47 °C. Figures 4.13, 4.14 and 4.15 show the fraction of damaged cells in tumors having frequency factor A=1.8 10^{36} 1/s and activation energy barrier ΔE_a=2.38 10^5 J/mol as function of the time when applying for 60 minutes heat sources between 1 and 12 W. The radii of the tumors tested are R_{tumor}=4, 6 and 8 mm and the radii of the PMMA are correspondingly R_{PMMA}=R_{tumor}-2 mm. We notice that more power is needed for bigger tumor volume. In the case of R_{tumor}=6 mm, the fraction of damaged cells when applying a heat source equal to 1 W is almost 0.4 after 10 min of heating whereas we have no damage for R_{tumor}=8 mm. However, for powers higher than 3 W the most important part of the damage is obtained in the first 20 minutes.

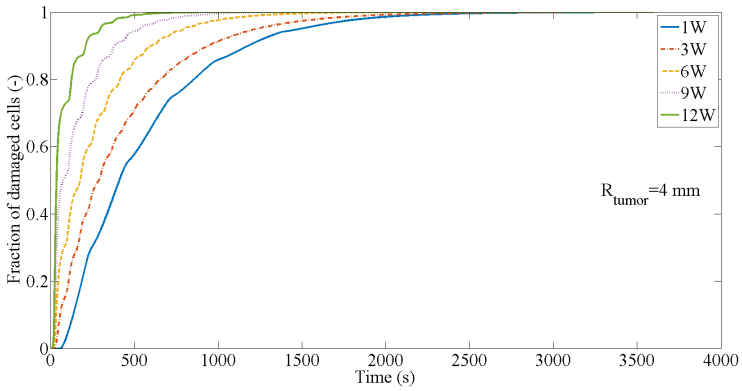

Figure 4.13: Fraction of damaged cells in tumor (R_{tumor}=4 mm) having frequency factor A=1.8 10^{36} 1/s and activation energy barrier ΔE_a=2.38 10^5 J/mol as function of the time when applying for 60 minutes heat sources between 1 and 12 W.

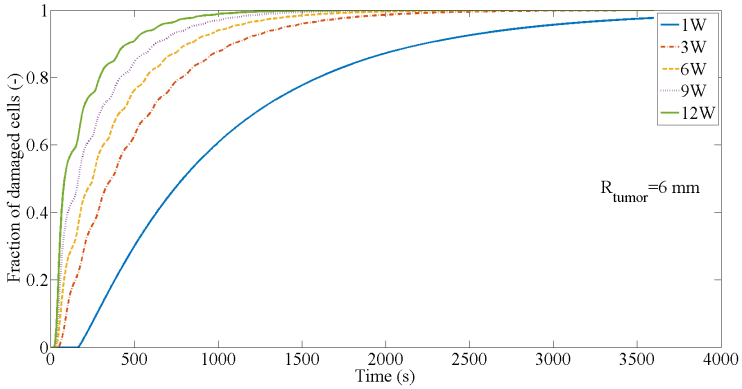

Figure 4.14: Fraction of damaged cells in tumor (R_{tumor}=6 mm) having frequency factor A=1.8 10^{36} 1/s and activation energy barrier ΔE_a=2.38 10^5 J/mol as function of the time when applying for 60 minutes heat sources between 1 W and 12 W.

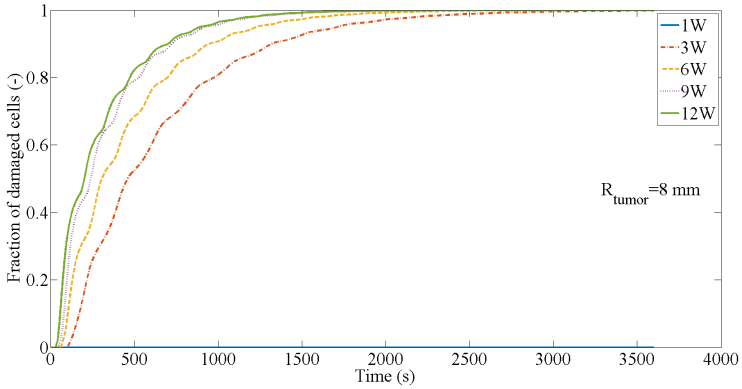

Figure 4.15: Fraction of damaged cells in tumor (R_{tumor}=8 mm) having frequency factor A=1.8 10^{36} 1/s and activation energy barrier ΔE_a=2.38 10^5 J/mol as function of the time when applying for 60 minutes heat sources between 1 W and 12 W.

Notice that Fig.4.15 shows that for larger tumor volumes i.e. 8 mm the low power of 1 W is not sufficient to have a successfull treatment. The temperature remained here below the 43°C, cfr. (4.19).
Table 4.5 shows the frequency (Hz) of the periodic switching ON/OFF procedure in order to keep the temperature at the outer boundary of the tumor region between 45 and 47°C for the considered powers and dimensions of the tumor region. It is clear that this frequency decreases by an increase of power and an increase of the volume.
Tables 4.6 and 4.7 gives the needed duration (seconds) in order to have an efficient hyperthermia treatment according to the Arrhenius model and CEM43, respectively. The efficient treatment is defined when obtaining a fraction of damaged cells equal to 0.95 (Arrhenius) or a value of CEM43 equal to 60 minutes. When comparing the results of the two damage models, the required durations are not corresponding, although the two damage models show the same tendencies. Both damages models result in an increase of the needed heating time when applying a lower power and considering a larger volume. Moreover, the larger the volume the higher the minimum power needed to have an efficient treatment. Indeed, for the case of R_{tumor}=8 mm, a power of 1 W is not sufficient. On the other hand, there may be an upper limit for the applied power. In particular, when the tumor region is near the spine. Indeed, we see for the case R_{tumor}=8 mm that the temperature at the position of the spine increases above 43 °C when applying a switching On/Off strategy in order to obtain a temperature variation at the outer boundary of the tumor between 45 and 47°C which may result in damaging the spine. Fig. 4.16 reveals damage in the spinal cord after 1000 s when applying a heat source equal to Q=9 W.

Table 4.5: Oscillations frequency (1/s) of the temperature profile

	3 W	6 W	9 W	12 W
4 mm	0.01577	0.01315	0.01160	0.01162
6 mm	0.00624	0.00968	0.009314	0.00853
8 mm	0.00433	0.00624	0.00632	0.00758

Table 4.6: Required duration (s) for the hyperthermia treatment in order to obtain fraction of damaged cells equal to 0.95 according to the Arrhenius model

	1 W	3 W	6 W	9 W	12 W
4 mm	1487	1233	796	534	296
6 mm	2871	1403	1077	836	638
8 mm	> 3600	1715	1230	925	895

Table 4.7: Required duration (s) for the hyperthermia treatment in order to obtain value of 60 minutes for the CEM43 parameter

	1 W	3 W	6 W	9 W	12 W
4 mm	420	173	34	24	20
6 mm	1812	304	75	48	38
8 mm	> 3600	523	200	93	65

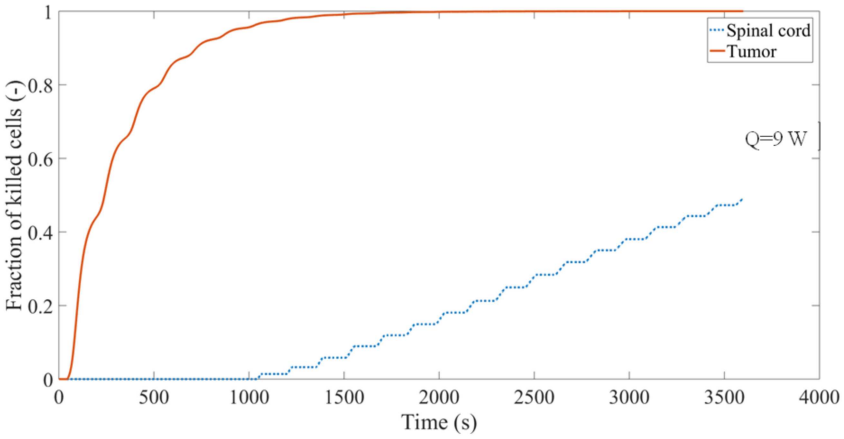

Figure 4.16: Fraction of damaged cells in tumor having frequency factor A=1.8 10^{36} 1/s and activation energy barrier ΔE_a=2.38 10^5 J/mol and the spinal cord when applying for 60 minutes heat source Q=9 W.

4.5 Conclusion

Starting from the fundamentals of heat transfer we detailed the Pennes' bioheat equations and proposed the damage models based on Arrhenius theory and the CEM43 model. We compared both damage models where we analyzed the required heating duration at a certain constant temperature to obtain a CEM43 value of 60 minutes. We furthermore discussed their limitations. Based on this we performed a computational study of temperature and damage distributions within the biological tissue when having a certain power generated via a PMMA-MNP implant for bone metastases MNH therapy. This was done using the finite element method that discretizes the geometry where the Pennes' bioheat equation was solved. Based on the simulations we have the following conclusions:

It is possible to define a switching On/Off strategy in order to increase the temperature in tumor region up to the required level of 45-47°C.

The two considered damage models frequently used in literature result in different values for the required duration to obtain an efficient hyperthermia treatment and consequently they should be used in a very critical way and rather for only qualitative purpuses.

The larger the tumor volume, the higher minimum value for the required power. Depending on the dimensions and the position of the tumor relative to the spinal cord, the applied power should be limited in order to avoid the damage in the spinal cord.

5

Experimental validation and general conclusions

'It always seems impossible until it is done.'

Nelson Mandela

5.1 Introduction

The effectiveness of hyperthermia largely depends on having sufficient temperature increase in the tumor region and minimizing the heating of normal tissue elsewhere, particularly in the spinal cord. In this chapter, single cycle and multi-cycles heating procedures of PMMA-MNP are experimentally verified, validating the technical feasibility of having PMMA-MNP as basic component for percutaneous vertebroplasty combined with hyperthermia treatment of metastatic bone tumors.

The second part of this chapter draws general conclusions of this dissertation where additionally future research directions are sketched.

5.2 *Ex-vivo* experimental realization of the heating with PMMA-particles

5.2.1 Overview of the complete setup

In this section, a dedicated pancake coil is designed to generate an efficient AMF able to heat up beef vertebra containing PMMA-MNP. The beef vertebra is placed in a water basin at 10 cm from the AMF generating circuit. The temperature increase is appraised using optical temperatures sensors. These sensors are not altered by the magnetic field contrary to e.g. resistance thermometers (such as PT-100) and thermocouples. The temperature is recorded continuously so that the temperature dynamics can be appraised. We measure the temperature at two locations: in the center of the PMMA-MNP bone cement T_1, which is located in the vicinity of metastatic bone tumors in clinical applications; and the temperature in the spine T_2, which needs to be safeguarded to high temperature exposures. An important prerequisite for having magnetic nanoparticle based heating of bone metastases is that the temperature in T_2 remains limited. This temperature will be closely monitored during the experiments. The temperature is controlled by means of on/off switching strategy, see also Section 4.3, on the basis of T_1 measurements. This will result in so-called multi-cycles heating.

5.2.1.1 Magnetic excitation

The AMF generator in our experimental setup comprises 3 main components: a power supply, a heating station including the coil that generates the AMF and a closed-circulating water cooling system (see Fig.5.1).
The power supply is a 10 kW induction heating system able to provide an alternating current to a resonant circuit with resonance frequency f_r between 150 kHz and 400 kHz. The minimal total capacity of the capacitors in the circuit is restricted to C=0.1 μF. The theoretical maximum current I allowed to flow through these capacitors is 450 A. In view of stability and safety, the current I used in practical application is limited to 200 A.

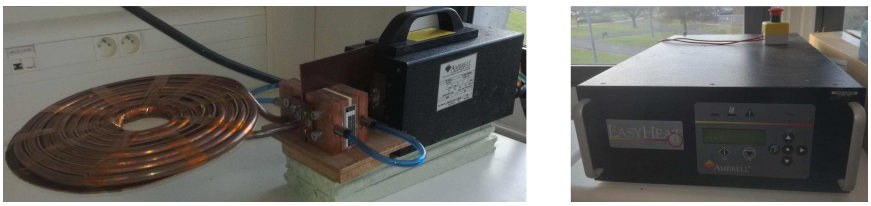

Figure 5.1: Experimental setup including the power supply (right) and the heating station with a closed-circulating water cooling system (left).

The 8 turns pancake coil with an outer radius of 13 cm is compatible with the

heating station with respect to stability and also gives rise to a maximum AMF amplitude of H_{max}= 1711 A/m at 10 cm above the coil. The inductor is put in series with C=0.1 μF capacitors. Inductance measurements showed that the inductance was approximately L=10 μH resulting in a LC-circuit having a resonance frequency of about 160 kHz. The decrease in AMF along the center line (z-axis) of that specific coil is reported in Fig. 5.2(a) as well as the decay of AMF along the radial axis d at a distance of z=10 cm in Fig. 5.2(b). These calculations are done on the basis of (2.37) detailed in Chapter 2. The gap between 2 turns is taken as 1,2 cm for practical reasons when manufacturing the coil.

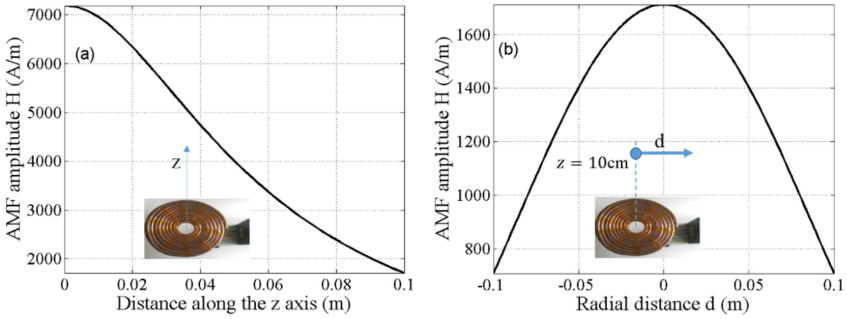

Figure 5.2: Magnetic field calculations of an 8-turns pancake coil with R_{max}=13 cm and a gap between 2 turns of 12 mm. The magnetic field variations are shown (a) along the center line of the coil (z-axis) and (b) for radial distance d from the center line at a distance of z=10 cm. The manufactured coil with z and d directions is shown in the insets

5.2.1.2 PMMA-MNP mixture

The PMMA-MNP samples are made by mixing VertaPlexTM radiopaque bone cement (manufactured by Stryker®) and Ferrotec EMG (Serie 1500) dry iron oxide nanoparticles. The core material of these MNPs is principally magnetite (Fe_3O_4) with a nominal diameter of 10 nm. We refer to Chapter 3 for further details on the magnetic nanoparticles and their characteristics when interacting with an AMF. They are single domain and superparamagnetic nanoparticles with an initial magnetic susceptibility of 0.2. The proportions by weight are 71.8 to 79.2 of iron oxide and 28.1 to 20.8 of surfactant. Having 22 wt.% of the total amount of PMMA does not significantly alter the mechanical properties of the cement [72]. During the polymerization, the PMMA-MNP mixtures are placed in cylindrical molds to have a standardized shape with a diameter D=1 cm and a length l=3 cm. A cylindrical hole is drilled in the core of the vertebra where the PMMA-MNP sample is placed.

5.2.1.3 Optocon temperature sensor

Due to the strong alternating AMF, many types of temperature sensors cannot be used. Temperature sensors containing metal are not compatible with the measurement environment. On the one hand, the temperature sensor could be damaged by the AMF or measurements could be wrong. Secondly, the presence of a metallic temperature sensor such as resistance thermometers or thermocouples could influence the measurement itself. Eddy currents for example can be induced, resulting in an unwanted heating of the sensor and the measurement environment. As a result, the choice of temperature sensor is limited to optical fibre temperature sensors. The Optocon®temperature sensor is connected to a PC to store the measured data. Measurements are performed with a sampling frequency of 1 second.

5.2.1.4 Beef vertebra

A beef vertebra is used to mimic a human one. By making a cavity in the vertebra, the PMMA mixture loaded with MNP can be inserted. The first temperature sensor T_1 is placed in the middle of the PMMA-MNP sample as shown in Fig. 5.3. A second hole, at a distance of about 5 cm from the sample, is made in the spinal cord for the second temperature sensor T_2. The entire bone is placed 10 cm above the AMF generating circuit and is immersed in distilled water to mimic the biological medium, see Fig. 5.4.

5.2.1.5 Heater

A heater is placed in the water basin to mimic the body temperature. A temperature sensor, connected to a controller, is placed in the water basin. Via the controller, the temperature can be set to the desired value 37 °C. The range in which the temperature is allowed to vary can be controlled by defining levels of temperatures at which the heating is switched on and off. In our case this system makes sure that the temperature remains between 36°C and 38°C.

5.2.2 Heat generation by PMMA-MNP in beef bone

Temperature measurement results in Fig.5.5(a) show the time dependence of the heat increase in the beef vertebra where the PMMA-MNP sample is placed at 10 cm above the center of the pancake coil. A temperature increase in T_1 is attained of approximately T_{max}=7 °C above the initial temperature T_0 (the first measurement are done at room temperature T_0=20 °C) when having an AMF applied during 14 min using the pancake coil with excitation current having amplitude I=200 A, whereas the increase of the temperature in the spine T_2 does not exceed 1 °C. Furthermore, experiments at T_0=37 °C were performed by keeping the temperature of

Figure 5.3: Beef vertebra with PMMA-MNP sample (grey)

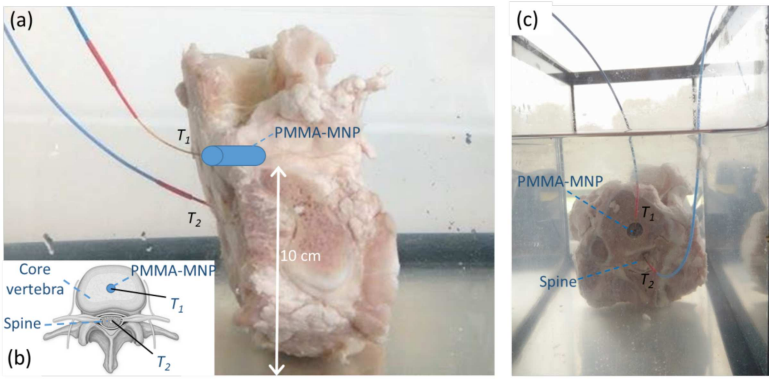

Figure 5.4: (a) Beef bone immersed in distilled water with the PMMA-MNP sample placed at 10 cm above the AMF generating circuit (b) Illustration of the temperatures measurements in the vertebra (T1) and in the spine (T2) (c) Frontal view of the sample.

the water container around 37 °C using the 500 Watt Titanium heater and the temperature controller. Since the thermal characteristics of the materials are not significantly affected by the considered temperature ranges (20-50 °C), no significant differences in heat increase were observed in 5.5(a). These *ex-vivo* experiments demonstrate the feasibility of heating tumor cells. Note that in our experiments there are important heat losses due to convection processes of the vertebra and PMMA-MNP in the water. One may expect higher temperature rise *in-vivo* because of the biological tissue surrounding the bone.

Fig. 5.5(b) displays the temperature variations during a multicycles heating process. The AMF is switched off when T_1 reaches a temperature of T_{max}=T_0+8 °C then switched on again after a temperature decrease of 2 °C. This mimics a possible clinical procedure of MNH when having a multicycles heating process where

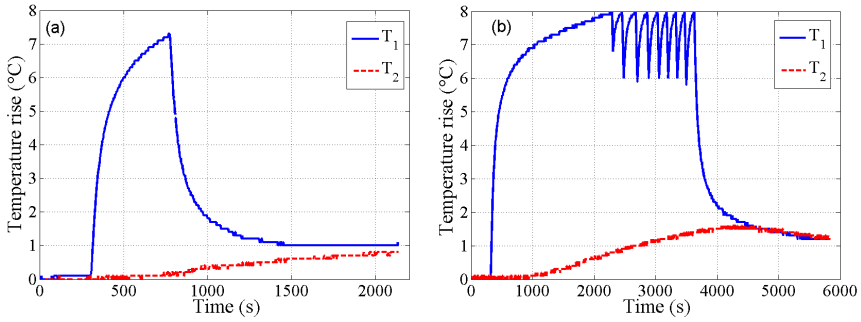

Figure 5.5: (a) The temperature rise in the core vertebra T_1 and in the spine T_2 due to the heating of the PMMA-MNP sample placed at 10 cm above the center of the pancake coil ($I = 200$ A, $f_R = 160$ kHz, calculated H_max=1711 A/m). (b) The temperature rise in the core vertebra (T_1) and in the spine (T_2) due to the multicycles heating of the PMMA-MNP sample placed at 10 cm above the center of the pancake coil.

the temperature rise is limited in the range of 6 to 8 °C during approximately half an hour (time exposure in MNH treatment) so to control the thermal elevations inflicted to healthy tissue and spine. The graph shows that after 1 hour of applying the AMF, the temperature increase in the spine (T_2) is less than 2 °C. These experimental results validate the feasibility of achieving magnetic nanoparticle hyperthermia in a vertebra that is located 10 cm above the inductor-capacitor circuit generating the AMF. We furthermore observed that the heating in the spinal cord remains limited.

5.2.3 Discussion and conclusion

The feasibility of having hyperthermia on the basis of PMMA-MNP samples containing 22 wt.% iron oxide nanoparticles was tested ex-vivo in beef vertebra. A coil was designed so to enable future animal and clinical tests; that satisfy technological constraints, i.e. the minimally allowed capacitance of the capacitors in the resonant inductor-capacitor circuit of the AMF generator; and that generates maximum alternating magnetic fields at a distance of 10 cm above the inductor. The *ex-vivo* experiments show that the PMMA-MNP sample, which is in clinical application in the vicinity of the metastatic bone tumors, heats up to 7°C with a negligible temperature increase in the spinal cord. We moreover experimentally verified the temperate rise in the PMMA-MNP sample and in the spine when applying on-off switched AMF, mimicking a possible clinical procedure that enables the control of temperature elevations in healthy tissue as well as in the spine. The temperature rise in the spine was limited to 2°C whereas in the PMMA-MNP a temperature rise in the range of 6-8 °C was established.

However, to determine the heating power of the PMMA-MNP sample in realistic conditions it is necessity to use a tissue mimic in the *ex-vivo* setup to include heat loss to the tissue without overestimating it. This can only be done if the properties really do match with acutal conditions. For the *ex-vivo* measurements, a beef vertebra is used to simulate a human one, so these thermal properties of the vertebra are already in accordance. However, in the human body, biological tissue is present surrounding the wide area around the vertebra. To implement the thermal properties of this tissue in the experimental model, a gel should be used with similar properties as the actual tissue. Finally, the heat drain by the aorta and inferior vena cava should be included as well. This can be done with use of a pump delivering a constant flow of water through a set of tubes.

5.3 General conclusions and future research directions

5.3.1 General conclusions

Spinal metastases are common complications of many cancers. In a clinical approach, they induce fractures, hypercalcemia and pain that are life threatening. They also increase morbidity of patients and alter their quality of life. The objective of this dissertation is to find solutions that enable treat spinal metastases and guarantee the stability of the vertebra. In this work, we load the PMMA with particles that in presence of an AMF become heat sources able to enable hyperthermia of spinal metastases and establish the mechanical stabilization of the spine.

Technical realization of the above mentioned overall objective comes with a large number of constraints. Firstly, to attain higher magnitudes of heat sources and thus elevated temperatures we aimed at increasing the AMF amplitude and frequency which however faces difficulties in the electrical circuits and power supply. On the one hand, a maximum AMF should be generated at a distance of 10 cm above the inductor respecting the minimally allowed capacitance of the capacitors in the resonant inductor-capacitor. On the other hand, AMF induces eddy currents in the biological tissue and can become painful for the patient leading to the unwanted heating of the healthy tissue and can moreover at certain levels of frequencies and magnetic fields result in nerve and cardiac stimulation. Therefore it is crucial to control the temperature increase specially in the vicinity of the spinal cord.

Another way of increasing the heat source is to increase the concentration of particles in the PMMA-particles mixture. Nevertheless having too high concentration of particles may result in the weakening of the mechanical stability of the PMMA

mixture leading to fractures. Next to mechanical weakening, inserting particles in the body need to be biocompatible and also MRI compatible so that it remains possible to adequately image the tumor region after treatment.

Chapter 1 started with a brief introduction to cancer, hyperthermia and the several modalities used clinically to treat spinal metastases. An overview of biological and thenical limitations that lead to a set of magnetic parameters for spinal metastases hyperthermia were explained.

In chapter 2 we presented analytical descriptions for the magnetic field and self-inductance for short cylindrical, helical and pancake coil topologies. Results showed that the design of the coil affects the magnetic field amplitude (H) and specifically the magnetic field decay at a certain distance from the inductor. We opted for the pancake coil topology as being the most appropriate design for generating a maximal magnetic field strength at a certain distance from the coil for performing magnetic hyperthermia.

In chapter 3 we detailed the different heating losses that particles can realize when subjected to an AMF. Two types of particles were considered. Non-magnetic particles generated heat due to eddy currect loss whereas the heating efficacy of magnetic particles is mainly due to Néel and Brownian relaxation. We sketched the linear response theory to address the dependency of the specific loss power due to Néel and Brownian relaxation of magnetic nanoparticles on the properties of the MNP and the AMF (amplitude and frequency). We stressed the domain of validity of the LRT as well as the size dependence of the relaxation constant. By making comparison of the linear response theory with micromagnetic simulations that are based on macrospin approximations, we concluded that a correction of the length of time characteristic of the material is required. We also concluded that using magnetorelaxometry measurement data it is possible to recover this characteristic length of time and include this together with the correction factor to predict the specific loss where heating can occur due to eddy currents dissipated in the particles.

Furthermore specific loss power measurements were performed using the calorimetric method that also contains uncertainties with respect to correct assessment of the specific loss power since the measurements are difficult to achieve in adiabatic conditions. We could achieve even with relatively low concentration of MNP a temperature increase of at least 6°C that is needed for hyperthermia treatment. We also experimentally investigated the effect of particles on the quality of magnetic resonance images. Both the concentration and type of MNP affect the MRI compatibility of PMMA mixed with MNP. Single core clustered powder resulted, for

similar concentrations, in higher artifacts compared to multicore MNP. We showed that having multicore powder having an iron oxide concentration of 0.07 wt% in the PMMA+MNP, resulted in artifacts that are less than 2 mm and that gave rise to a temperature increase of 7°C which is sufficient for hyperthermia treatment of bone metastases.

When the particles act as heat sources because of their presence in the AMF, the temperature diffuse throughout the biological tissue. Thus to avoid the risk of damaging healthy tissue it is important to evaluate the increase of temperature and its distribution in space and time. Chapter 4 provided a behavioral model based on Pennes' bioheat equation that allows to calculate temperature distributions in space and time within biological tissues for given heating power and thermal properties of biological tissues. For a simplified geometry of the spine we perform extensive thermal analyses on the effect of the heating power of particles in PMMA on the temperature. A 3D finite element method was implemented to solve the Pennes bioheat equation, describing macroscopic heat transfer in biological tissues. Results showed that it is possible to define a switching On/Off strategy in order to increase the temperature in tumor region up to the required level of 45-47°C.

In chapter 5 we investigated the heating capacity of the magnetic nanoparticle in an *ex-vivo* experiment for an inductor-capacitor circuit located at a certain distance from PMMA+MNP. Experiments revealed that the temperature rise in the spine was limited to 2°C whereas in the PMMA+MNP a temperature rise in the range of 6-8 °C was established.

In Fig.5.6 we integrate all aspects treated in previous chapters schematically presented by the functions f_{AMF}, f_{HEAT}, f_{TEMP} and f_{DAMAGE}. It shows explicitly the dependencies between the various chapters. This toolchain can be used to assess the effect of the parameters that are input to the functions f_{AMF}, f_{HEAT}, f_{TEMP}, f_{DAMAGE}, and their importance in the frame of hyperthermia for treating spinal metastases.

5.4 Future research directions

Multiple future research directions can be followed starting from this work that can be synthesized in two major research tracks. A first major research direction is on further optimizing magnetic nanoparticle hyperthermia. More work is necessary to better understand the kinetics of the heat produced by PMMA+MNP mixture under an AMF. Other mixtures of bone cements and particles types can be investigated to maximize the heat generated at lower magnetic field amplitudes which are clinically relevant. A lower concentration of MNP may permit the use of MRI

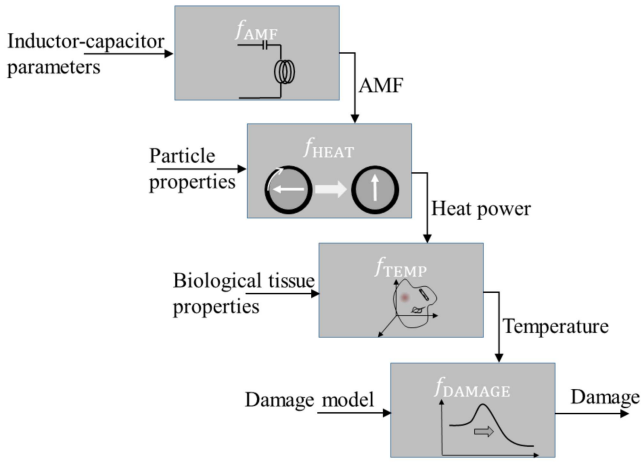

Figure 5.6: Integration of magnetic, heat power, thermal and damage analyses for hyperthermia using PMMA-particles for spinal metastases.

for the follow-up of larger tumor regions. Also a high heating efficacy at lower field strengths may give the opportunety to patients having the vertebral grafts and implants prior to MNH to take advantage of the treatment without removing the metallic part.

A second major future research direction is related to pre-clinical researchs of magnetic nanoparticle hyperthermia for bone metastases. Studies involving animal models and various types of tumor cells are needed for a deeper understanding of heat diffusion phenomena of MNP and their interaction in the biological environment. Moreover *in-vivo* studies may highlight potential future clinical benefits of magnetic nanoparticle hyperthermia as an adjuvant therapy with radiation or chemotherapeutic agents.

It is my hope that this dissertation will inspire researchers to explore new challenging avenues in this dynamic and rapidly evolving field.

A

Optimum magnetic field estimation based on experimental SLP data

In this work, a custom equation is used to fit experimenal SLP data of four different aqueous nanoparticle suspensions: BNF-dextran, JHU, Nanomag-D-spio and $MnFe_2O_4$ (see Table A.1).

BNF-dextran nanoparticles consist of a dense core of multiple parallelepiped iron oxide crystallites, synthesized by a high temperature and pressure homogenization process, coated by dextran. JHU nanoparticles are also forming a dense core of multiple spherical iron oxide crystallites by a high gravity controlled precipitation after which they are coated with citric acid. Nanomag-D-spio's are formed by co-precipitation of iron salts in the presence of dextran, resulting in a diffuse core with spherical crystallites dispersed in a dextran matrix. Finally, $MnFe_2O_4$ nanoparticles are synthesized by the co-precipitation method and surface-coated with citric acid.

Table A.1: Parameters of studied nanoparticles [10]

Name	Iron concentration (mg/ml)	Surface
BNF-Dextran	15 ± 2	Dextran/H_2O
JHU	90 ± 10	Citrate/H_2O
Nanomag-D-spio	5 ± 0.8	Dextran/H_2O
$MnFe_2O_4$	11.3 ± 1.5	Citrate/H_2O

Amplitude and frequency dependence of the SLP results is shown in [10]. SLP data obtained are in the frequency range of 150 to 375 kHz and magnetic fields of 4-44 kA/m. In order to determine the optimal magnetic field for the different type of nanoparticles, the experimental SLP values are plotted as function of H and f. Values used for estimating SLP was automated and repeated for the four magnetic nanoparticles types. For every combination of H and f, a fitted value of SLP is assigned using the following equation:

$$SLP(f,H) = (f + p_1 f^2)[p_2 H + \frac{p_3}{H}$$

$$+p_4.tanh(p_5(H - p_6)) + p_7.tanh(p_8(H - p_9))] \quad \text{(A.1)}$$

where p_1, p_2, p_3, p_4, p_5, p_6, p_7, p_8 and p_9 are constants in Table A.2. f and H depict the frequency f and the amplitude of the magnetic field strength H. In Fig.A.1, the SLP variation is shown as function of the magnetic field strength H and the frequency f. The red dotted line presents the limit of Hxf=5 10^9. BNF-Dextran nanoparticles show low SLP at lower field amplitudes, whereas the heating efficiency rises quickly at amplitude between 20-40 kA/m (Fig.A.1(a)). Below the red line, the maximum value of SLP is around 650 W/g_{FeO} and appears at H=28 kA/m and f=175 kHz. JUH nanoparticles, on the other hand demonstrate higher heating efficiency at lower amplitudes than BNF nanoparticles (Fig.A.1(b)). Concidering the frequency of 300 kHz, the highest SLP value within the biological limit is obtained at 17 kA/m : SLP=707 $W/gFeO$. Nanomag-D-spoi nanoparticles display lower thermal dissipation than all other nanoparticles (Fig.A.1(c)). By respecting the biological limit, the maximum SLP value of 78 W/g_{FeO} is achieved at $f > 350$ kHz and $H < 15$ kA/m. $MnFe_2O_4$ nanoparticles (Fig.A.1(d)) display SLP similar to Nanomag-D-spio with SLP values higher than 70 W/g_{FeO} when having magnetic field $H < 15$ kA/m and frequency $f > 350$ kHz.

In conclusion, the field strength H and frequency f needed to have the maximum SLP value are deeply related to the type of magnetic nanoparticles considered. Thus, the electrical supply for the coil used for hyperthermia should be adapted to the type of nanoparticles.

Table A.2: Parameters of the SLP fit

	p_1	p_2	p_3	p_4	p_5	p_6	p_7	p_8	p_9
Nanomag-D-spio	0.5423	24.22	0.003364	-0.4995	0.004266	-18.71	-24.16	-18.78	0.1439
BNF-Dextran	-1.235	-1.836	0.01104	-0.2318	-0.0004788	-27.71	-1.883	20.32	-0.1437
JHU	143.6	0.005314	0.008285	4.772	-0.0005092	10.17	-3.088	7.504	-0.1056
$MnFe_2O_4$	-2.589	-0.01983	0.004036	-0.08567	0.00466	-8.648	-0.001037	16.14	5.47

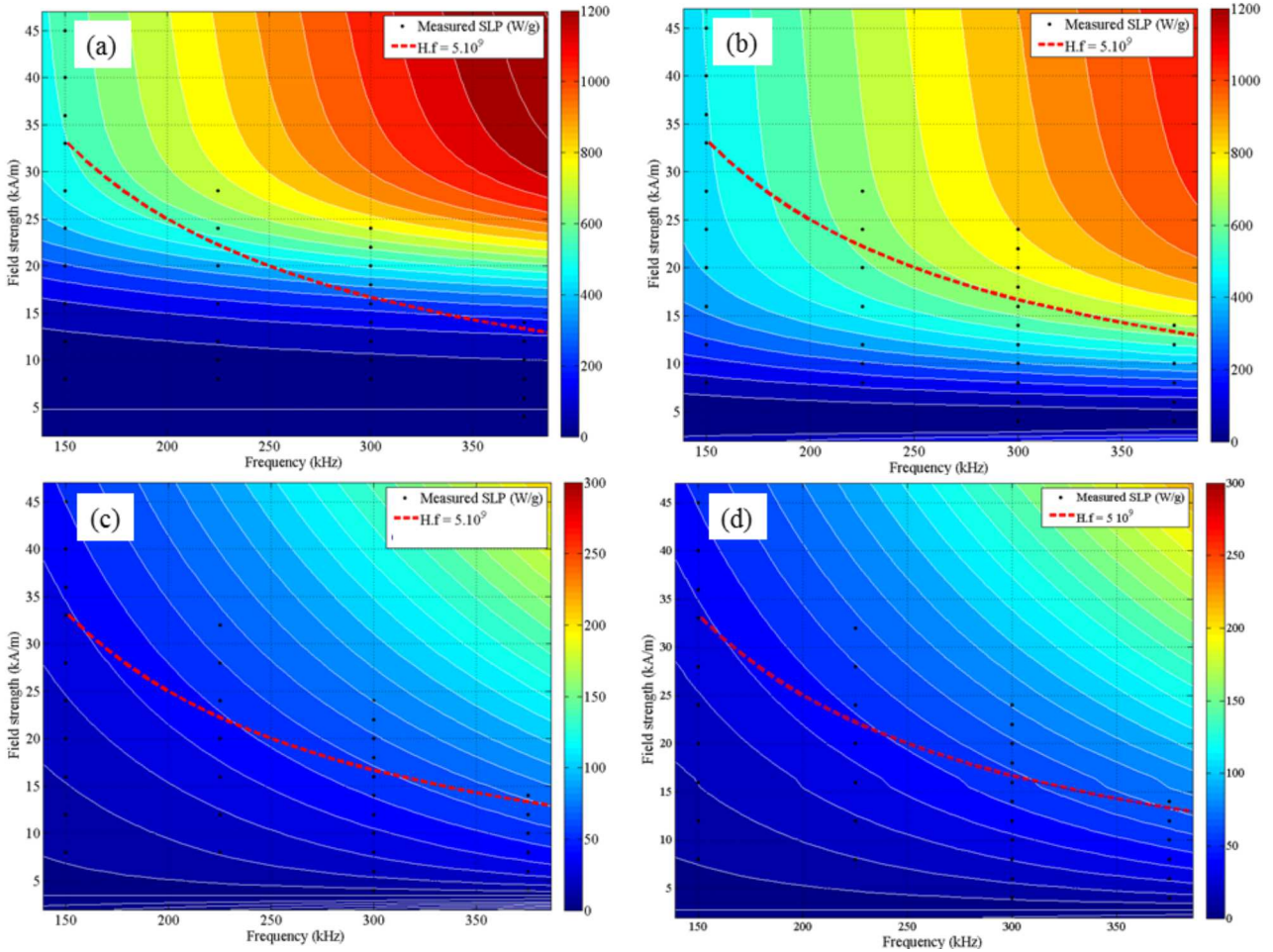

Figure A.1: The fitted SLP values as function of the magnetic field strength H and the frequency f for four types of magnetic nanoparticles (a) $BNF - dextran$, (b) JHU, (c) $Nanomag - D - spio$ and (d) $MnFe_2O_4$. The red dotted line presents the limit of Hxf=5 10^9

B

Bioheat transfer equation for bone metastases hyperthermia

B.1 Introduction

In hyperthermia procedure, the temperature distribution in the biological tissue should be controlled to achieve a safe and effective treatment. Therefore, studies are performed to obtain an estimation of the desired temperature distribution. Here, the steady state bioheat equation is solved analytically in cylindrical and spherical coordinates for simplified geometries. These geometries include the following regions: heat source, tumor, healty bone, and muscles (see Fig.B.1). The heat source required at steady state is calculated by considering as boundary conditions the temperature at the outer radius of the tumor T_{in}=47°C and the outer radius of the muscles T_{out}=37°C. The materials thermal properties and dimensions are reported in Table B.1

Tissue i	Heat source (i=1)	Tumor (i=2)	Bone (i=3)	Muscle (i=4)
R_i (m)	0.005	0.008	0.02	0.04
k_i (W/m.K)	0.19	0.51	0.32	0.49

Table B.1: Thermal conductivities and radii of the considered biological tissues

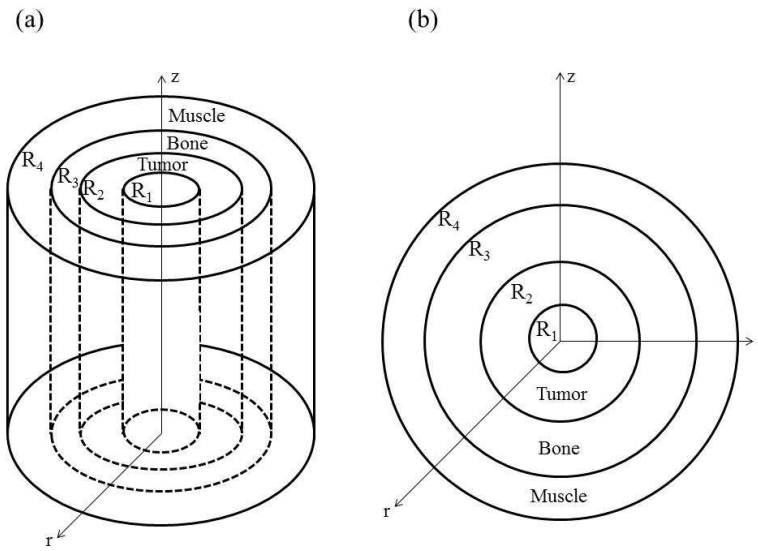

Figure B.1: Scheme of the heat source, tumor, healty bone, and muscles tissues in (a) cylindrical geometry (b) spherical geometry

B.2 Bioheat equation in cylindrical coordinate system

The cylindrical geometry consists of 4 coaxial cylinders, having the same axial length. Each cylinder is numbered starting from the cylinder with smallest radius: $R_1 < R_2 < R_3 < R_4$, see Fig.B.1(a).
The heat equation in cylindrical coordinates (r,ϕ,z) is given by:

$$\rho C_p \frac{\partial T}{\partial t} = \frac{1}{r}\frac{\partial}{\partial r}\left(kr\frac{\partial T}{\partial r}\right) + \frac{1}{r^2}\frac{\partial}{\partial \phi}\left(k\frac{\partial T}{\partial \phi}\right) + \frac{1}{r^2\sin^2\theta}\frac{\partial}{\partial z}\left(k\frac{\partial T}{\partial z}\right) + g_{cyl} \tag{B.1}$$

with ρ, c_p and k being mass density, specific heat capacity and thermal conductivity respectively, while $g_{cyl}[W/m^3]$ is the heat produced by the total number of particles in cylinder 1. In steady state and by considering only the radial dependence of the temperature (no ϕ and z variations), the heat equation (B.1) becomes:

$$\frac{1}{r}\frac{\partial}{\partial r}\left(kr\frac{\partial T}{\partial r}\right) + g_{cyl} = 0 \tag{B.2}$$

The general solution of equation (B.2) is:

$$T(r) = \frac{-g_{cyl}r^2}{4k} + \frac{A}{k}\ln r + B \tag{B.3}$$

We adapt equation (B.3) to the 4 regions (cylinders 1, 2, 3 and 4):

$$T_1(r) = \frac{-g_{cyl} r^2}{4k_1} + \frac{C_1}{k_1} \ln r + C_2 \tag{B.4}$$

$$T_2(r) = \frac{C_3}{k_2} \ln r + C_4 \tag{B.5}$$

$$T_3(r) = \frac{C_5}{k_3} \ln r + C_6 \tag{B.6}$$

$$T_4(r) = \frac{C_7}{k_4} \ln r + C_8 \tag{B.7}$$

The parameters C_1, C_2,C_3,...,C_8 are determined by the boundary conditions at $r = R_2$ and $r = R_4$: $T_2(R_2)$=T_{in} and $T_4(R_4)$=T_{out} and the continuity conditions for the temperature and the thermal flux on the surfaces between neighbouring tissues.

If we consider the surface between the tumor and the healthy bone, the continuity conditions results in:

$$T_2(R_2) = T_3(R_2);\ -k_2 \frac{\partial T_2(R_2)}{\partial r} = -k_3 \frac{\partial T_3(R_2)}{\partial r} \tag{B.8}$$

If we consider the surface between the bone and the muscles, the continuity conditions become:

$$T_3(R_3) = T_4(R_4);\ -k_3 \frac{\partial T_3(R_3)}{\partial r} = -k_4 \frac{\partial T_4(R_3)}{\partial r} \tag{B.9}$$

Using the equations (B.5), (B.6) and (B.7) we obtain from the continuity conditions for the thermal flux:

$$C_3 = C_5 = C_7$$

As a numerical example we take the temperature at the surface between the PMMA and the tumor $T_2(R_1)$ equal to 47°C :

$$T_{in} = T_2(R_2) = \frac{C_3}{k_2} \ln(R_2) + C_4 = 47°C$$

and the temperature of the outer radius of the muscle is equal to body temperature :

$$T_{out} = T_4(R_4) = \frac{C_7}{k_4} \ln(R_4) + C_8 = 37°C$$

The continuity conditions for the temperature result in:

$$\frac{C_3}{k_2}\ln(R_2) + C_4 = \frac{C_3}{k_3}\ln(R_2) + C_6$$

$$\frac{C_3}{k_3}\ln(R_3) + C_6 = \frac{C_3}{k_4}\ln(R_3) + C_8$$

Using the constants given in Table B.1, we calculate the C_3 value:

$$C_3 = C_5 = C_7 = \frac{T_{out} - T_{in}}{\frac{1}{k_3}\ln(\frac{R_3}{R_2}) + \frac{1}{k_4}\ln(\frac{R_4}{R_3})} = -2.3375 \tag{B.10}$$

Thus,

$$C_4 = T_{in} - \frac{C_3}{k_2}\ln(R_2) = 24.8702$$

and

$$C_8 = T_{out} - \frac{C_7}{k_4}\ln(R_4) = 21.6446$$

$$C_6 = C_8 + \frac{C_7}{k_4}\ln(R_3) - \frac{C_5}{k_3}\ln(R_3) = 11.7304$$

Finally, the heat needed Q_{sph}(W)=g_{cyl}(W/m^3) V_{source} is equal to:

$$g_{cyl}V_{source} = -k_2\frac{\partial T_2(R_1)}{\partial r}S_{source}$$

$$g_{cyl}\pi R_1^2 h = -k_2\frac{C_3}{k_2 R_1}2\pi R_1 h$$

$$g_{cyl} = -\frac{2C_3}{R_1^2} = 187024 W/m^3 \tag{B.11}$$

and Q=0.23 W when considering the the height of the cylinder h=R_1=0.005 m.

B.3 Bioheat equation in spherical coordinate system

The spherical geometry contains 4 concentric spheres. Each sphere is numbered starting with the smallest radius: $R_1 < R_2 < R_3 < R_4$ as shown in Fig.B.1(b). The heat equation in spherical coordinates can be written as follow:

$$\rho C_p\frac{\partial T}{\partial t} = \frac{1}{r^2}\frac{\partial}{\partial r}\left(kr^2\frac{\partial T}{\partial r}\right) + \frac{1}{r^2\sin\theta}\frac{\partial}{\partial\theta}\left(k\sin\theta\frac{\partial T}{\partial\theta}\right)$$

$$+\frac{1}{r^2\sin^2\theta}\frac{\partial}{\partial\phi}\left(k\frac{\partial T}{\partial\phi}\right) + g_{sph} \tag{B.12}$$

with g_{sph}[W/m^3] is the heat produced by the total number of particles in sphere 1. In steady state and by considering only the radial dependency of the temperature (no θ and ϕ variations), the heat equation (B.12) becomes:

$$\frac{1}{r^2}\frac{\partial}{\partial r}\left(kr^2\frac{\partial T}{\partial r}\right) + g_{sph} = 0 \tag{B.13}$$

The general solution of equation (B.13) is:

$$T(r) = \frac{-g_{sph}r^2}{6k} + \frac{A}{kr} + B \tag{B.14}$$

We adapt equation (B.14) to the 4 regions (Spheres 1, 2, 3 and 4):

$$T_1(r) = \frac{-g_{sph}r^2}{6k_1} - \frac{C_1}{k_1 r} + C_2 \tag{B.15}$$

$$T_2(r) = \frac{-C_3}{k_2 r} + C_4 \tag{B.16}$$

$$T_3(r) = \frac{-C_5}{k_3 r} + C_6 \tag{B.17}$$

$$T_4(r) = \frac{-C_7}{k_4 r} + C_8 \tag{B.18}$$

If we consider the surface between the tumor and the healthy bone, the continuity conditions results in:

$$T_2(R_2) = T_3(R_2);\ -k_2\frac{\partial T_2(R_2)}{\partial r} = -k_3\frac{\partial T_3(R_2)}{\partial r} \tag{B.19}$$

If we consider the surface between the bone and the muscles, the continuity conditions become:

$$T_3(R_3) = T_4(R_4);\ -k_3\frac{\partial T_3(R_3)}{\partial r} = -k_4\frac{\partial T_4(R_3)}{\partial r} \tag{B.20}$$

Using the equations (B.16), (B.17) and (B.18) we obtain from the continuity conditions for the thermal flux:

$$C_3 = C_5 = C_7$$

As mentioned in the previous example, the temperature at the surface between the PMMA and the tumor $T_2(R_2)$ is equal to 47 °C :

$$T_{in} = T_2(R_2) = \frac{-C_3}{k_2 R_2} + C_4 = 47°C$$

and the temperature of the outer radius of the muscle should be equal to the body temperature :

$$T_{out} = T_4(R_4) = \frac{-C_7}{k_4 R_4} + C_8 = 37°C$$

The continuity conditions for the temperature result in:

$$\frac{-C_3}{k_2 R_2} + C_4 = \frac{-C_3}{k_3 R_2} + C_6$$

$$\frac{-C_3}{k_3 R_3} + C_6 = \frac{-C_3}{k_4 R_3} + C_8$$

Using the constants given in Table B.1, the C_3 value becomes:

$$C_3 = C_5 = C_7 = \frac{T_{out} - T_{in}}{\frac{1}{k_3}(\frac{1}{R_2} - \frac{1}{R_3}) + \frac{1}{k_4}(\frac{1}{R_3} - \frac{1}{R_4})} = -0.03504 \tag{B.21}$$

Thus,

$$C_4 = T_{in} + \frac{C_3}{k_2 R_2}$$

and

$$C_8 = T_{out} + \frac{C_7}{k_4 R_4}$$

Thus, the heat needed Q(W)=g_{sph}(W/m^3)V_{source} is equal to:

$$g_{sph} V_{source} = -k_2 \frac{\partial T_2(R_1)}{\partial r} S_{source}$$

$$g_{sph} \frac{4\pi R_1^3}{3} = -k_2 \frac{C_3}{k_2 R_1^2} 4\pi R_1^2$$

$$g_{sph} = -\frac{3C_3}{R_1^3} = 840960 W/m^3 \tag{B.22}$$

and Q_{sph}=0.44 W

Notice that - in the cylindrical as well as in the spherical model - the power (Q_{cyl} or Q_{sph}) obtained above is the power required to maintain the temperature at $r = R_2$ at T_{in}=47 °C, once the system reached the steady state. However a higher power is needed in order to obtain this steady state regime. This is discussed in more detail in Chapter 4.
Finally, it is clear from (B.10), (B.11) (B.21) and (B.22) that in case the tumor is located in more conductive tissues with higher k values, higher values for Q_{cyl} or Q_{sph} are needed.

References

[1] J. van der Zee, Z. Vujaskovic, M. Kondo, and T. Sugahara, "The kadota fund international forum 2004–clinical group consensus," *International Journal of Hyperthermia*, vol. 24, no. 2, pp. 111–122, 2008.

[2] F. H. Shen, D. Samartzis, and R. G. Fessler, *Textbook of the Cervical Spine E-Book*. Elsevier Health Sciences, 2014.

[3] D. R. Fourney, D. F. Schomer, R. Nader, J. Chlan-Fourney, D. Suki, K. Ahrar, L. D. Rhines, and Z. L. Gokaslan, "Percutaneous vertebroplasty and kyphoplasty for painful vertebral body fractures in cancer patients," *Journal of Neurosurgery: Spine*, vol. 98, no. 1, pp. 21–30, 2003.

[4] P. F. Heini and R. Orler, "Kyphoplasty for treatment of osteoporotic vertebral fractures," *European Spine Journal*, vol. 13, no. 3, pp. 184–192, 2004.

[5] A. Hubert and R. Schäfer, *Magnetic domains: the analysis of magnetic microstructures*. Springer Science & Business Media, 2008.

[6] D. E. Bordelon, C. Cornejo, C. Grüttner, F. Westphal, T. L. DeWeese, and R. Ivkov, "Magnetic nanoparticle heating efficiency reveals magneto-structural differences when characterized with wide ranging and high amplitude alternating magnetic fields," *Journal of Applied Physics*, vol. 109, no. 12, p. 124904, 2011.

[7] F. Cardarelli, *Materials handbook*. Springer, 2000.

[8] M. Ohring, *Engineering materials science*. Elsevier, 1995.

[9] I. Busscher, J. J. Ploegmakers, G. J. Verkerke, and A. G. Veldhuizen, "Comparative anatomical dimensions of the complete human and porcine spine," *European Spine Journal*, vol. 19, no. 7, pp. 1104–1114, 2010.

[10] F. Soetaert, S. K. Kandala, A. Bakuzis, and R. Ivkov, "Experimental estimation and analysis of variance of the measured loss power of magnetic nanoparticles," *Scientific reports*, vol. 7, no. 1, p. 6661, 2017.

[11] S. Heim and F. Mitelman, *Cancer cytogenetics: chromosomal and molecular genetic aberrations of tumor cells*. John Wiley & Sons, 2015.

[12] H. Lodish, A. Berk, S. L. Zipursky, P. Matsudaira, D. Baltimore, and J. Darnell, "Molecular cell biology 4th edition," *National Center for Biotechnology Information, Bookshelf*, 2000.

[13] G. Kroemer, L. Galluzzi, P. Vandenabeele, J. Abrams, E. S. Alnemri, E. Baehrecke, M. Blagosklonny, W. El-Deiry, P. Golstein, D. Green, *et al.*, "Classification of cell death: recommendations of the nomenclature committee on cell death 2009," *Cell death and differentiation*, vol. 16, no. 1, p. 3, 2009.

[14] A. Chow, "Cell cycle control by oncogenes and tumor suppressors: driving the transformation of normal cells into cancerous cells," *Nature Education*, vol. 3, no. 9, p. 7, 2010.

[15] A. M. A. Velez and M. S. Howard, "Tumor-suppressor genes, cell cycle regulatory checkpoints, and the skin," *North American Journal of Medical Sciences*, vol. 7, no. 5, p. 176, 2015.

[16] R. L. Siegel, K. D. Miller, and A. Jemal, "Cancer statistics, 2016," *CA: a cancer journal for clinicians*, vol. 66, no. 1, pp. 7–30, 2016.

[17] R. Weinberg, *The biology of cancer*. Garland science, 2013.

[18] T. Reya, S. J. Morrison, M. F. Clarke, and I. L. Weissman, "Stem cells, cancer, and cancer stem cells," *nature*, vol. 414, no. 6859, p. 105, 2001.

[19] B. J. Huntly and D. G. Gilliland, "Leukaemia stem cells and the evolution of cancer-stem-cell research," *Nature Reviews Cancer*, vol. 5, no. 4, p. 311, 2005.

[20] R. A. Kyle, M. A. Gertz, T. E. Witzig, J. A. Lust, M. Q. Lacy, A. Dispenzieri, R. Fonseca, S. V. Rajkumar, J. R. Offord, D. R. Larson, *et al.*, "Review of 1027 patients with newly diagnosed multiple myeloma," vol. 78, no. 1, pp. 21–33, 2003.

[21] K. A. Hoadley, C. Yau, D. M. Wolf, A. D. Cherniack, D. Tamborero, S. Ng, M. D. Leiserson, B. Niu, M. D. McLellan, V. Uzunangelov, *et al.*, "Multiplatform analysis of 12 cancer types reveals molecular classification within and across tissues of origin," *Cell*, vol. 158, no. 4, pp. 929–944, 2014.

[22] V. Labi and M. Erlacher, "How cell death shapes cancer," *Cell death & disease*, vol. 6, no. 3, p. e1675, 2016.

[23] R. Gerl and D. L. Vaux, "Apoptosis in the development and treatment of cancer," *Carcinogenesis*, vol. 26, no. 2, pp. 263–270, 2005.

[24] K. D. Miller, R. L. Siegel, C. C. Lin, A. B. Mariotto, J. L. Kramer, J. H. Rowland, K. D. Stein, R. Alteri, and A. Jemal, "Cancer treatment and survivorship statistics, 2016," *CA: a cancer journal for clinicians*, vol. 66, no. 4, pp. 271–289, 2016.

[25] E. Winer, J. Gralow, L. Diller, B. Karlan, P. Loehrer, L. Pierce, G. Demetri, P. Ganz, B. Kramer, M. Kris, *et al.*, "Clinical cancer advances 2008: major research advances in cancer treatment, prevention, and screening—a report from the american society of clinical oncology," *Journal of clinical oncology*, vol. 27, no. 5, p. 812, 2009.

[26] E. M. Knavel and C. L. Brace, "Tumor ablation: common modalities and general practices," *Techniques in Vascular & Interventional Radiology*, vol. 16, no. 4, pp. 192–200, 2013.

[27] G. Delaney, S. Jacob, C. Featherstone, and M. Barton, "The role of radiotherapy in cancer treatment," *Cancer*, vol. 104, no. 6, pp. 1129–1137, 2005.

[28] B. Zachariah, L. Balducci, G. Venkattaramanabalaji, L. Casey, H. M. Greenberg, and J. A. DelRegato, "Radiotherapy for cancer patients aged 80 and older: a study of effectiveness and side effects," *International Journal of Radiation Oncology* Biology* Physics*, vol. 39, no. 5, pp. 1125–1129, 1997.

[29] T. Boulikas and M. Vougiouka, "Recent clinical trials using cisplatin, carboplatin and their combination chemotherapy drugs," *Oncology reports*, vol. 11, no. 3, pp. 559–595, 2004.

[30] S. H. Kaufmann and W. C. Earnshaw, "Induction of apoptosis by cancer chemotherapy," *Experimental cell research*, vol. 256, no. 1, pp. 42–49, 2000.

[31] H. J. Burstein, "Side effects of chemotherapy," *Journal of Clinical Oncology*, vol. 18, no. 3, pp. 693–693, 2000.

[32] G. M. Hahn, *Hyperthermia and cancer*. Springer Science & Business Media, 2012.

[33] K. F. Chu and D. E. Dupuy, "Thermal ablation of tumours: biological mechanisms and advances in therapy," *Nature reviews. Cancer*, vol. 14, no. 3, p. 199, 2014.

[34] N. Datta, S. G. Ordóñez, U. Gaipl, M. Paulides, H. Crezee, J. Gellermann, D. Marder, E. Puric, and S. Bodis, "Local hyperthermia combined with

radiotherapy and-/or chemotherapy: Recent advances and promises for the future," *Cancer treatment reviews*, vol. 41, no. 9, pp. 742–753, 2015.

[35] M. R. Horsman and J. Overgaard, "Hyperthermia: a potent enhancer of radiotherapy," *Clinical Oncology*, vol. 19, no. 6, pp. 418–426, 2007.

[36] G. E. Kim, S.-w. Lee, S. K. Chang, H. C. Park, H. R. Pyo, J. H. Kim, S. R. Moon, H. S. Lee, E. C. Choi, and K. M. Kim, "Combined chemotherapy and radiation versus radiation alone in the management of localized angiocentric lymphoma of the head and neck," *Radiotherapy and Oncology*, vol. 61, no. 3, pp. 261–269, 2001.

[37] K. G. Riedel, P. P. Svitra, J. M. Seddon, D. M. Albert, E. S. Gragoudas, A. M. Koehler, D. J. Coleman, J. Torpey, F. L. Lizzi, and J. Driller, "Proton beam irradiation and hyperthermia: Effects on experimental choroidal melanoma," *Archives of Ophthalmology*, vol. 103, no. 12, pp. 1862–1869, 1985.

[38] C. Coughlin, E. Douple, J. Strohbehn, W. Eaton Jr, B. Trembly, and T. Wong, "Interstitial hyperthermia in combination with brachytherapy.," *Radiology*, vol. 148, no. 1, pp. 285–288, 1983.

[39] H. H. Kampinga, "Cell biological effects of hyperthermia alone or combined with radiation or drugs: a short introduction to newcomers in the field," *International journal of hyperthermia*, vol. 22, no. 3, pp. 191–196, 2006.

[40] A. Bettaieb, P. K. Wrzal, and D. A. Averill-Bates, "Hyperthermia: Cancer treatment and beyond," in *Cancer Treatment-Conventional and Innovative Approaches*, InTech, 2013.

[41] C. Schroeder, C. Gani, U. Lamprecht, C. H. von Weyhern, M. Weinmann, M. Bamberg, and B. Berger, "Pathological complete response and sphincter-sparing surgery after neoadjuvant radiochemotherapy with regional hyperthermia for locally advanced rectal cancer compared with radiochemotherapy alone," *International Journal of Hyperthermia*, vol. 28, no. 8, pp. 707–714, 2012.

[42] B. Rau, P. Wust, W. Tilly, J. Gellermann, C. Harder, H. Riess, V. Budach, R. Felix, and P. Schlag, "Preoperative radiochemotherapy in locally advanced or recurrent rectal cancer: regional radiofrequency hyperthermia correlates with clinical parameters," *International Journal of Radiation Oncology• Biology• Physics*, vol. 48, no. 2, pp. 381–391, 2000.

[43] J. L. Roti Roti, "Cellular responses to hyperthermia (40–46 c): Cell killing and molecular events," *International Journal of hyperthermia*, vol. 24, no. 1, pp. 3–15, 2008.

[44] N. van den Tempel, M. R. Horsman, and R. Kanaar, "Improving efficacy of hyperthermia in oncology by exploiting biological mechanisms," *International journal of hyperthermia*, vol. 32, no. 4, pp. 446–454, 2016.

[45] R. A. Vertrees, A. Leeth, M. Girouard, J. D. Roach, and J. B. Zwischenberger, "Whole-body hyperthermia: a review of theory, design and application," *Perfusion*, vol. 17, no. 4, pp. 279–290, 2002.

[46] H. Kok, P. Wust, P. R. Stauffer, F. Bardati, G. Van Rhoon, and J. Crezee, "Current state of the art of regional hyperthermia treatment planning: a review," *Radiation Oncology*, vol. 10, no. 1, p. 196, 2015.

[47] D. Cranston, "A review of high intensity focused ultrasound in relation to the treatment of renal tumours and other malignancies," *Ultrasonics sonochemistry*, vol. 27, pp. 654–658, 2015.

[48] M. Grandolfo, "Worldwide standards on exposure to electromagnetic fields: an overview," *The Environmentalist*, vol. 29, no. 2, pp. 109–117, 2009.

[49] Y. Ni, S. Mulier, Y. Miao, L. Michel, and G. Marchal, "A review of the general aspects of radiofrequency ablation," *Abdominal imaging*, vol. 30, no. 4, pp. 381–400, 2005.

[50] W. Hurter and F. Reinbold, "Microwave hyperthermia applicator," Oct. 25 1994. US Patent 5,358,515.

[51] K. T. Noell, K. T. Woodward, B. T. Worde, R. I. Fishburn, L. S. Miller, *et al.*, "Microwave-induced local hyperthermia in combination with radiotherapy of human malignant tumors," *Cancer*, vol. 45, no. 4, pp. 638–646, 1980.

[52] Q. A. Pankhurst, J. Connolly, S. Jones, and J. Dobson, "Applications of magnetic nanoparticles in biomedicine," *Journal of physics D: Applied physics*, vol. 36, no. 13, p. R167, 2003.

[53] R. Gilchrist, R. Medal, W. D. Shorey, R. C. Hanselman, J. C. Parrott, and C. B. Taylor, "Selective inductive heating of lymph nodes," *Annals of surgery*, vol. 146, no. 4, p. 596, 1957.

[54] L. H. Reddy, J. L. Arias, J. Nicolas, and P. Couvreur, "Magnetic nanoparticles: design and characterization, toxicity and biocompatibility, pharmaceutical and biomedical applications," *Chemical reviews*, vol. 112, no. 11, pp. 5818–5878, 2012.

[55] A. K. Gupta and M. Gupta, "Synthesis and surface engineering of iron oxide nanoparticles for biomedical applications," *Biomaterials*, vol. 26, no. 18, pp. 3995–4021, 2005.

[56] W. J. Atkinson, I. A. Brezovich, and D. P. Chakraborty, "Usable frequencies in hyperthermia with thermal seeds," *IEEE Transactions on Biomedical Engineering*, no. 1, pp. 70–75, 1984.

[57] A. Jordan, R. Scholz, K. Maier-Hauff, M. Johannsen, P. Wust, J. Nadobny, H. Schirra, H. Schmidt, S. Deger, S. Loening, *et al.*, "Presentation of a new magnetic field therapy system for the treatment of human solid tumors with magnetic fluid hyperthermia," *Journal of magnetism and magnetic materials*, vol. 225, no. 1-2, pp. 118–126, 2001.

[58] U. Gneveckow, A. Jordan, R. Scholz, V. Brüß, N. Waldöfner, J. Ricke, A. Feussner, B. Hildebrandt, B. Rau, and P. Wust, "Description and characterization of the novel hyperthermia-and thermoablation-system mfh® 300f for clinical magnetic fluid hyperthermia," *Medical physics*, vol. 31, no. 6, pp. 1444–1451, 2004.

[59] K. Maier-Hauff, F. Ulrich, D. Nestler, H. Niehoff, P. Wust, B. Thiesen, H. Orawa, V. Budach, and A. Jordan, "Efficacy and safety of intratumoral thermotherapy using magnetic iron-oxide nanoparticles combined with external beam radiotherapy on patients with recurrent glioblastoma multiforme," *Journal of neuro-oncology*, vol. 103, no. 2, pp. 317–324, 2011.

[60] R. Coleman, "Metastatic bone disease: clinical features, pathophysiology and treatment strategies," *Cancer treatment reviews*, vol. 27, no. 3, pp. 165–176, 2001.

[61] R. Coleman and R. Rubens, "The clinical course of bone metastases from breast cancer," *British journal of cancer*, vol. 55, no. 1, p. 61, 1987.

[62] S. Helweg-Larsen and P. S. Sørensen, "Symptoms and signs in metastatic spinal cord compression: a study of progression from first symptom until diagnosis in 153 patients," *European Journal of Cancer*, vol. 30, no. 3, pp. 396–398, 1994.

[63] B. Weigel, M. Maghsudi, C. Neumann, R. Kretschmer, F. J. Müller, and M. Nerlich, "Surgical management of symptomatic spinal metastases: postoperative outcome and quality of life," *Spine*, vol. 24, no. 21, p. 2240, 1999.

[64] M. Harabech, J. Leliaert, A. Coene, G. Crevecoeur, D. Van Roost, and L. Dupré, "The effect of the magnetic nanoparticle's size dependence of the

relaxation time constant on the specific loss power of magnetic nanoparticle hyperthermia," *Journal of Magnetism and Magnetic Materials*, vol. 426, pp. 206–210, 2017.

[65] M. Sadeghi, L. Janani, S. Aarabi, F. Shokraneh, and V. Rahimi-Movaghar, "Vertebroplasty and kyphoplasty for metastatic spinal lesions: A systematic review," *Global Spine Journal*, vol. 6, no. 1_suppl, pp. s–0036, 2016.

[66] M. Niculescu, B. L. Solomon, G. Viscopoleanu, and I. Antoniac, "Evolution of cementation techniques and bone cements in hip arthroplasty," *Handbook of Bioceramics and Biocomposites*, pp. 1–41, 2014.

[67] J.-S. Wang, S. Toksvig-Larsen, P. Müller-Wille, and H. Franzén, "Is there any difference between vacuum mixing systems in reducing bone cement porosity?," *Journal of Biomedical Materials Research: An Official Journal of The Society for Biomaterials and The Japanese Society for Biomaterials*, vol. 33, no. 2, pp. 115–119, 1996.

[68] J. J.-S. Stone, J. A. Rand, E. K. Chiu, J. J. Grabowski, and K.-N. An, "Cement viscosity affects the bone-cement interface in total hip arthroplasty," *Journal of orthopaedic research*, vol. 14, no. 5, pp. 834–837, 1996.

[69] S. Saha and S. Pal, "Mechanical properties of bone cement: a review," *Journal of Biomedical Materials Research Part A*, vol. 18, no. 4, pp. 435–462, 1984.

[70] M. Harabech, N. R. Kiselovs, W. Maenhoudt, G. Crevecoeur, D. Van Roost, and L. Dupré, "Experimental ex-vivo validation of pmma-based bone cements loaded with magnetic nanoparticles enabling hyperthermia of metastatic bone tumors," *AIP advances*, vol. 7, no. 5, p. 056704, 2017.

[71] Z. H. Tang, X. W. Wang, L. Pan, Y. W. Hu, Y. Wu, J. Y. Zhang, S. Cui, J. Y. Kang, and J. T. Tang, "Preparation and characterization of pmma-based cements containing magnetic nanoparticles for the magnetic hyperthermia," in *Advanced Materials Research*, vol. 647, pp. 155–159, Trans Tech Publ, 2013.

[72] M. Kawashita, K. Kawamura, and Z. Li, "Pmma-based bone cements containing magnetite particles for the hyperthermia of cancer," *Acta Biomaterialia*, vol. 6, no. 8, pp. 3187–3192, 2010.

[73] H.-L. Yang, T. Liu, X.-M. Wang, Y. Xu, and S.-M. Deng, "Diagnosis of bone metastases: a meta-analysis comparing 18fdg pet, ct, mri and bone scintigraphy," *European radiology*, vol. 21, no. 12, pp. 2604–2617, 2011.

[74] K. Krupa and M. Bekiesińska-Figatowska, "Artifacts in magnetic resonance imaging," *Polish journal of radiology*, vol. 80, p. 93, 2015.

[75] B. A. Hargreaves, P. W. Worters, K. B. Pauly, J. M. Pauly, K. M. Koch, and G. E. Gold, "Metal-induced artifacts in mri," *American Journal of Roentgenology*, vol. 197, no. 3, pp. 547–555, 2011.

[76] P. Stradiotti, A. Curti, G. Castellazzi, and A. Zerbi, "Metal-related artifacts in instrumented spine. techniques for reducing artifacts in ct and mri: state of the art," *European Spine Journal*, vol. 18, no. 1, pp. 102–108, 2009.

[77] P. Sminia, J. J. Hendriks, A. H. Van der Kracht, H. M. Rodermond, J. Haveman, W. Jansen, K. Koedooder, and N. A. Franken, "Neurological observations after local irradiation and hyperthermia of rat lumbosacral spinal cord," *International Journal of Radiation Oncology• Biology• Physics*, vol. 32, no. 1, pp. 165–174, 1995.

[78] N. Franken, H. De Vrind, P. Sminia, J. Haveman, D. Troost, and D. Gonzalez Gonzalez, "Neurological complications after 434 mhz microwave hyperthermia of the rat lumbar region including the spinal cord," *International journal of radiation biology*, vol. 62, no. 2, pp. 229–238, 1992.

[79] T. Yamane, A. Tateishi, S. Cho, S. Manabe, M. Yamanashi, A. Dezawa, H. Yasukouchi, and K. Ishioka, "The effects of hyperthermia on the spinal cord.," *Spine*, vol. 17, no. 11, pp. 1386–1391, 1992.

[80] P. Sminia, J. Haveman, and D. Troost, "Thermotolerance of the spinal cord after fractionated hyperthermia applied to the rat in the cervical region," *International Journal of hyperthermia*, vol. 6, no. 2, pp. 269–278, 1990.

[81] J. Subjeck, J. Sciandra, and R. Johnson, "Heat shock proteins and thermotolerance; a comparison of induction kinetics," *The British journal of radiology*, vol. 55, no. 656, pp. 579–584, 1982.

[82] I. A. Brezovich, "Low frequency hyperthermia: capacitive and ferromagnetic thermoseed methods," *Medical physics monograph*, vol. 16, pp. 82–111, 1988.

[83] H. A. Wheeler, "Simple inductance formulas for radio coils," *Proceedings of the Institute of Radio Engineers*, vol. 16, no. 10, pp. 1398–1400, 1928.

[84] C. Elias, J. Lima, R. Valiev, and M. Meyers, "Biomedical applications of titanium and its alloys," *Jom*, vol. 60, no. 3, pp. 46–49, 2008.

[85] C. J. Gannon, P. Cherukuri, B. I. Yakobson, L. Cognet, J. S. Kanzius, C. Kittrell, R. B. Weisman, M. Pasquali, H. K. Schmidt, R. E. Smalley, *et al.*,

"Carbon nanotube-enhanced thermal destruction of cancer cells in a noninvasive radiofrequency field," *Cancer: Interdisciplinary International Journal of the American Cancer Society*, vol. 110, no. 12, pp. 2654–2665, 2007.

[86] A. Przekora, A. Benko, M. Nocun, J. Wyrwa, M. Blazewicz, and G. Ginalska, "Titanium coated with functionalized carbon nanotubes—a promising novel material for biomedical application as an implantable orthopaedic electronic device," *Materials Science and Engineering: C*, vol. 45, pp. 287–296, 2014.

[87] B. L. Perkins and N. Naderi, "Suppl-3, m7: carbon nanostructures in bone tissue engineering," *The open orthopaedics journal*, vol. 10, p. 877, 2016.

[88] G. Gałuszka, M. Madej, D. Ozimina, J. Kasińska, and R. Gałuszka, "The characterisation of pure titanium for biomedical applications," *Metalurgija*, vol. 56, no. 1-2, pp. 191–194, 2017.

[89] C. Bidinosti, E. Chapple, and M. Hayden, "The sphere in a uniform rf field—revisited," *Concepts in Magnetic Resonance Part B: Magnetic Resonance Engineering: An Educational Journal*, vol. 31, no. 3, pp. 191–202, 2007.

[90] D. Makki, K. Naikoti, and S. Murali, "Magnetic resonance imaging signal artefacts from invisible metal debris following surgery to the elbow," *Shoulder & elbow*, vol. 10, no. 2, pp. 133–135, 2018.

[91] K. M. Krishnan, "Biomedical nanomagnetics: a spin through possibilities in imaging, diagnostics, and therapy," 2010.

[92] M. Colombo, S. Carregal-Romero, M. F. Casula, L. Gutierrez, M. P. Morales, I. B. Boehm, J. T. Heverhagen, D. Prosperi, and W. J. Parak, "Biological applications of magnetic nanoparticles," *Chemical Society Reviews*, vol. 41, no. 11, pp. 4306–4334, 2012.

[93] S. Batra, W. Scholz, and T. Roscamp, "Effect of thermal fluctuation field on the noise performance of a perpendicular recording system," *Journal of applied physics*, vol. 99, no. 8, p. 08E706, 2006.

[94] C. L. Dennis and R. Ivkov, "Physics of heat generation using magnetic nanoparticles for hyperthermia," *International Journal of Hyperthermia*, vol. 29, no. 8, pp. 715–729, 2013.

[95] R. E. Rosensweig, "Heating magnetic fluid with alternating magnetic field," *Journal of magnetism and magnetic materials*, vol. 252, pp. 370–374, 2002.

[96] J. Carrey, B. Mehdaoui, and M. Respaud, "Simple models for dynamic hysteresis loop calculations of magnetic single-domain nanoparticles: Application to magnetic hyperthermia optimization," *Journal of Applied Physics*, vol. 109, no. 8, p. 083921, 2011.

[97] J. Leliaert, A. Vansteenkiste, A. Coene, L. Dupré, and B. Van Waeyenberge, "Vinamax: a macrospin simulation tool for magnetic nanoparticles," *Medical & biological engineering & computing*, vol. 53, no. 4, pp. 309–317, 2015.

[98] A. Coene, *Non-invasive methods for spatial and quantitative reconstructions of magnetic nanoparticles using electron paramagnetic resonance and magnetorelaxometry*. PhD thesis, Ghent University, 2017.

[99] T. L. Gilbert, "A phenomenological theory of damping in ferromagnetic materials," *IEEE Transactions on Magnetics*, vol. 40, no. 6, pp. 3443–3449, 2004.

[100] F. Soetaert, L. Dupré, R. Ivkov, and G. Crevecoeur, "Computational evaluation of amplitude modulation for enhanced magnetic nanoparticle hyperthermia," *Biomedical Engineering/Biomedizinische Technik*, vol. 60, no. 5, pp. 491–504, 2015.

[101] R. Wildeboer, P. Southern, and Q. Pankhurst, "On the reliable measurement of specific absorption rates and intrinsic loss parameters in magnetic hyperthermia materials," *Journal of Physics D: Applied Physics*, vol. 47, no. 49, p. 495003, 2014.

[102] E. Natividad, M. Castro, and A. Mediano, "Adiabatic vs. non-adiabatic determination of specific absorption rate of ferrofluids," *Journal of Magnetism and Magnetic Materials*, vol. 321, no. 10, pp. 1497–1500, 2009.

[103] M. Coïsson, G. Barrera, F. Celegato, L. Martino, F. Vinai, P. Martino, G. Ferraro, and P. Tiberto, "Specific absorption rate determination of magnetic nanoparticles through hyperthermia measurements in non-adiabatic conditions," *Journal of Magnetism and Magnetic Materials*, vol. 415, pp. 2–7, 2016.

[104] L. Aranda-Lara, E. Torres-García, and R. Oros-Pantoja, "Biological tissue modeling with agar gel phantom for radiation dosimetry of 99mtc," *Open Journal of Radiology*, vol. 4, no. 01, p. 44, 2014.

[105] F. Lecouvet, J. N. Talbot, C. Messiou, P. Bourguet, Y. Liu, and N. M. de Souza, "Monitoring the response of bone metastases to treatment with magnetic resonance imaging and nuclear medicine techniques: a review and

position statement by the european organisation for research and treatment of cancer imaging group," *European Journal of Cancer*, vol. 50, no. 15, pp. 2519–2531, 2014.

[106] H. T. Banks and H. T. Tran, *Mathematical and experimental modeling of physical and biological processes*. CRC Press, 2009.

[107] W. C. Dewey, "Arrhenius relationships from the molecule and cell to the clinic," *International journal of hyperthermia*, vol. 10, no. 4, pp. 457–483, 1994.

[108] J. A. Pearce, "Comparative analysis of mathematical models of cell death and thermal damage processes," *International Journal of Hyperthermia*, vol. 29, no. 4, pp. 262–280, 2013.

[109] I. Dos Santos, D. Haemmerich, D. Schutt, A. F. da Rocha, and L. R. Menezes, "Probabilistic finite element analysis of radiofrequency liver ablation using the unscented transform," *Physics in Medicine & Biology*, vol. 54, no. 3, p. 627, 2009.

[110] M. N. Rylander, Y. Feng, Y. Zhang, J. Bass, R. J. Stafford, A. Volgin, J. D. Hazle, and K. R. Diller, "Optimizing heat shock protein expression induced by prostate cancer laser therapy through predictive computational models," *Journal of biomedical optics*, vol. 11, no. 4, p. 041113, 2006.

[111] J. A. Pearce, "Relationship between arrhenius models of thermal damage and the cem 43 thermal dose," in *Energy-based Treatment of Tissue and Assessment V*, vol. 7181, p. 718104, International Society for Optics and Photonics, 2009.

[112] S. A. Sapareto and W. C. Dewey, "Thermal dose determination in cancer therapy," *International Journal of Radiation Oncology* Biology* Physics*, vol. 10, no. 6, pp. 787–800, 1984.

[113] M. W. Dewhirst, B. Viglianti, M. Lora-Michiels, M. Hanson, and P. Hoopes, "Basic principles of thermal dosimetry and thermal thresholds for tissue damage from hyperthermia," *International Journal of Hyperthermia*, vol. 19, no. 3, pp. 267–294, 2003.

[114] O. S. Nielsen and J. Overgaard, "Effect of extracellular ph on thermotolerance and recovery of hyperthermic damage in vitro," *Cancer research*, vol. 39, no. 7 Part 1, pp. 2772–2778, 1979.

[115] "Database for thermal and electromagnetic parameters of biological tissues." `https://itis.swiss/virtual-population/tissue-properties/overview/`. Accessed: 2018-05-15.

[116] B. L. Wright, J. T. Lai, and A. J. Sinclair, "Cerebrospinal fluid and lumbar puncture: a practical review," *Journal of neurology*, vol. 259, no. 8, pp. 1530–1545, 2012.